Vortex ring-tube reconnection in a viscous fluid

Van Luc Nguyen[1,2*] and Viet Dung Duong[3]

[1]Division of Thermal and Fluids Science, Institute for Computational Science, Ton Duc Thang University, Ho Chi Minh City, Vietnam

[2]Faculty of Civil Engineering, Ton Duc Thang University, Ho Chi Minh City, Vietnam

[3]School of Aerospace Engineering, University of Engineering and Technology, Vietnam National University, Ha Noi City, Vietnam

Abstract

The vortex ring-tube reconnection in a viscous fluid was investigated using a proposed vortex-in-cell method combined with a large eddy simulation model (LVIC). This method was verified using simulations of the Taylor–Green vortex flow at the Reynolds numbers (Re) of 200 and 2000. The results show that the present method can capture the small-scale vortex structures in turbulent flows well. Besides, a Lagrangian method for passive scalar transport was successfully developed to track the vortex dynamics. The LVIC was then applied to three simulations of the interaction of a vortex ring at $Re^r_\Gamma(\Gamma/\nu) = 10000$ and a vortex tube at $Re^t_\Gamma = 1000$, 5000 and 10000. At $Re^r_\Gamma = 10000$ and $Re^t_\Gamma = 1000$, the effects of the tube on the ring are trivial while the ring breaks it into two parts and entrains them. The flow's energy spectrum remains unchanged with time, the small-scale vortices are not generated, and the ring's motion plays a key role in the flow. Moreover, the helicity distribution on the vortices is negligible. At $Re^r_\Gamma = 10000$ and $Re^t_\Gamma = 5000$, the tube breaks into two parts, and the leaving part of the tube interacts forcefully with the ring to form the small-scale vortices at the high wavenumbers. The population of small-scale vortex structures increases with time, and the large-scale vortices are twisted after the impingement. At $Re^r_\Gamma = 10000$ and $Re^t_\Gamma = 10000$, the impingement of the ring on the tube leads to their breakdown and reconnection. A part of the ring interacts with the leaving part of the tube to form a secondary ring, while the rest replaces the leaving part to reconnect the tube. The population of small-scale vortex structures and helicity distribution increase in this flow stage because of the interaction of the secondary ring wake and connection vortices. However, after the reconnection, the population and helicity distribution on the vortex structures significantly decrease. The smallest-scale vortex structure and the most effective mixing occur with $Re^r_\Gamma = 10000$ and $Re^t_\Gamma = 5000$.

Keywords: Vortex-in-cell method, Large eddy simulation, Vortex interaction, Vortex ring, Vortex tube

1 Introduction

Vortex reconnection is the key to understanding the fluid flow phenomena observed in various environmental processes and engineering applications such as head collision of two vortex rings [1], dynamics

*Corresponding author: nguyenvanluc@tdtu.edu.vn

of vortex tubes [2], trailing vortices behind airplane [3], turbulent mixing layer in internal combustion engines [4, 5], quantum turbulence in super-fluidity [6]. Comprehensive understanding of the vortex interaction is essential to improving the design and controlling the related engineering devices. This has attracted the interest of many researchers in recent years. Scheeler et al. [2] measured the helicity and dynamics of intertwined thin-core vortex tubes in a viscous fluid flow. They showed that these helical vortices are stretched or compressed by another vortex; however, the total helicity remains unchanged. Winckelmans et al. [3] investigated reconnection of four counter-rotating vortex tubes in a viscous fluid at $Re_\Gamma = 5000$ using a vortex filament method. They showed the global vortex tube dynamics and found Crow instability before their reconnection. Walmsley et al. [6] pointed out that the collision and reconnection of two unidirectional quantized vortex rings of the equal radius in the limit of zero temperature generate vortex loops of both smaller and larger scales. These larger loops formed in the collision appear from random clusters of small quantized vortex rings. Jaque and Fuentes [7] investigated the reconnection of two orthogonal vortex tubes with small numerical viscosity corresponding to $Re_\Gamma = 15000$. They showed that the time to start reconnection significantly increases with the increase of the initial distance of two tubes. However, the reconnection lasts around 0.75 times of the vortex turnover for initial distances and two investigated vorticity profiles of the tube. Therefore, they declared the reconnection as a convective process. Rees et al. [8] performed the particle-based simulations of the dynamics of two antiparallel vortex tubes for a long time duration at $Re_\Gamma = 10000$. The elliptical-shaped rings along with axial flow are formed, corresponding to the primary vortex tube reconnection. The vortex tube reconnection with and without an initial axial flow manifests $-7/3$ and $-5/3$ slopes of energy cascade, respectively. Hussain and Duraisamy [9] discussed the scaling and self-similarity of coherent structure reconnection of two vortex tubes located in an antiparallel configuration in a viscous fluid and revealed a close relationship between the reconnection and the slope of the energy spectrum. The reconnection was captured in detail using direct numerical simulations (DNS) at low-to-moderate Re_Γ ranging from 250 to 9000. The colliding threads determined as multiple vortex cores were found corresponding to the planar jet because of the effects of high Re_Γ. Beardsell [10] numerically studied the viscous reconnection of two vortex tubes with orthogonal and antiparallel configurations in a range of Re_Γ from 500 to 1000 using spectral simulations. The reconnection time scales on Re_Γ with a continuous power law from -1 to $-1/2$. They emphasized that the initial orientations of two vortices do not influence their reconnection physics. The antiparallel vortex tube reconnection was numerically investigated by McGavin and Pontin [11] in the context of axial flow driving a vortex line twisting in same and opposite senses. The full reconnection manifesting three-dimensional complex thread structures was captured for the same sense of twist, while for the opposite twist, the two-dimensional reconnection was produced, causing the asymmetry of two vortex threads as a result of reconnection. Cheng et al. [12] studied the dynamics of two and three coaxial vortex rings via vortex leapfrogging and choreographies in a viscous fluid using a Lattice Boltzmann method. The vortex leapfrogging was attained in the case of two coaxial vortex rings, while in the case of three coaxial vortex rings, the leapfrogging alters from the inviscid model. They continued to investigate the time evolution of a single elliptical viscous vortex ring at Re_Γ in a range from 500 to 3000 [13]. They observed a cross linking of vorticity and splitting the vortex ring into two sub-rings after the axis switching. The number of sub-rings increases with the increase in the ratio of two axes of an elliptical vortex ring. Yao and Hussain [14] inspected the turbulence cascade model through vortex reconnection, including the successive reconnection avalanche. At moderate Re, the successive reconnection generates a population of small-scale vortex rings, hairpin vortex structures, and vortex tangles while at high Re, the reconnection splits into finner-scale turbulent structures, which produces the fine vortex tangle avalanche. Motivated by the works of Lim and Nickels [1] and Chu et al. [15] related to head-on vortex ring collision, Cheng et al. [16] numerically investigated the asymmetry development of vortex ringlets in the outcome of face-to-face colliding vortex rings due to the effects of the core size difference. The nonequivalent radial rates of each vortex ring's induced velocity were found due to the unequal core sizes in the unavailability of vortex rings' azimuthal perturbations. In contrast, in the existence of azimuthal perturbations, the occurring vortex ringlets change the outward direction of the collision into the inclined plane. The head-on collision of two elliptical-shaped vortex rings was further numerically investigated by Cheng et al. [17] to reveal the highly changeable flow topology through the collision, including the development of subelliptical-shaped rings in the nonexistence of azimuthal perturbation and availability of secondary vortex ringlets in the existence of azimuthal perturbation. The viscous reconnecting vortex rings arranged in various configurations at $Re_\Gamma = 250$ was numerically carried out by Chatelain et al. [18]. The dissipation of reconnection was obtained owing to the stretched secondary-vortex structures transferring the kinetic energy to dissipated small-scale structures. McKeown et al. [19] investigated the collisions of two counter-rotating vortex rings and tubes at $Re_\Gamma = 4500$ using DNS. They showed that the elliptic instability causes turbulent cascade development. This instability induces the formation of antiparallel secondary filaments, and these filaments interact together, resulting in the generation of smaller tertiary filaments.

In the engineering applications related to the turbulent mixing layer, a device's efficiency can be improved by mixing the turbulent vortex structures. Kato et al. [20] compared the liquid mixing due to the vortex rings generated from a circular pipe and a jet mixer. They pointed out that the ring enhances the mixing; however, the mixing time by the rings is shorter than that by a jet mixer with the same average flow rate. Zawadzki and Aref [21] studied the mixing of nondiffusion scalar particles through the noncoaxial collision of two identical rings. The mixing is improved as the distance between two ring axes increases from zero to about 0.25 ring radius. A further increase of the distance results in a reduction in the mixing because of the appearance of reconnection that impairs the stretching of vortex configuration. Hernándeza and Reyes [22] investigated the mixing due to the symmetrical collision of three and six vortex rings at $Re < 1000$ generated from jets arranged in 120° and 60° angle configurations, respectively. They reported that with three vortex rings, the collision induces the pairing of adjacent vortex tubes in opposite directions, and then these pairs radially expand to form secondary arm-like structures, whereas with six rings, these phenomena do not occur. However, two new secondary vortex rings formed move upward and downward, perpendicular to the horizontal collision plane for both cases. The mixing can be investigated using simulations of the collision of a vortex ring with a vortex tube. Ishikawa et al. [4] investigated the collision of a vortex ring at $Re^r_\Gamma = 500$ with a vortex tube at circulation ratios $\Gamma^r/\Gamma^t = 0.5 - 2$, where Γ^r and Γ^t are circulations of the ring and tube at the outset. They showed that the ring is stretched and twisted around the tube at a ratio smaller than unity. At a ratio equal to unity, the reconnection occurs between a part of the ring and a part of the tube. At a ratio larger than unity, the ring passes through the tube. The interaction of two vortices was clarified in the context of the laminar flow. The effects of the high Re on vortex structure, the reconnection, and the mixing in these interactions have not yet been explained. Therefore, this study will shed some light on this issue through simulations of the interaction of a vortex ring at $Re^r_\Gamma = 10000$ and a tube at $Re^t_\Gamma = 1000, 5000$ and 10000 using a proposed vortex-in-cell

(VIC) method combined with a large eddy simulation (LES) model.

The VIC method is a hybrid Eulerian–Lagrangian vortex method, known as a redistributed vortex particle method. It uses both the Eulerian and Lagrangian reference frames to describe the fluid flow and the vorticity–velocity formula to calculate the flow momentum. It is a combination of the meshfree and mesh-based methods for calculation of the fluid flow dynamics. In the meshfree methods, the fluid is discretized into the vortex particles in the Lagrangian description. These particles move at their velocities designated by the flow velocity at their positions and transport the flow momentum in term of vorticity. There are some advantages of these methods compared to the traditional mesh-based methods. First, the mesh-free methods require no mesh; therefore, they avoid the computational cost in mesh generation and mesh distortion issues. Second, these methods reduce numerical dissipation errors because of computing the convection term in linear form [23]. Solving the linear convection equation is not constrained by the Courant–Friedrichs–Lewy condition, so allowing to choose a more massive time step for simulations while ensuring the method's stability. Besides, these methods offer superior features in the analysis of vortex dynamics such as deformation, breakdown, coalescence, and decay of vortices of various scales [24].

However, the meshfree methods have a high computational cost when the particle velocity is obtained from the Biot–Savart integral. The velocity of a particle is calculated by a sum of $(n-1)$ multiplications from the rest of particles, resulting in $\mathcal{O}(n^2)$ operations for n particles [25]. Besides, these methods face the particle distribution distortion because of clustering particles caused by the natural Lagrangian motion of particles and fluid strains [26]. This clustering results in the lack of particles in some regions, in which the continuity of flow is not satisfied. The disadvantage of meshfree methods can be resolved using the Eulerian formulas for the velocity field and flow momentum calculated using the mesh-based methods. Interpolation technique is the key to the connection between the Lagrangian and Eulerian descriptions. The method redistributes particles onto the grid, at which the vorticity of particles is interpolated from that at the Lagrangian positions, ensuring the flow momentum conservation. This redistribution overcomes the problem of particle distribution distortion adequately. Moreover, the computational cost reduces when computing the particle velocity on the grid through solving the Poisson equation using a mesh-based method, such as the successive-over-relaxation or fast Fourier transform methods with $\mathcal{O}(n^{\frac{3}{2}})$ and $\mathcal{O}(n \log n)$ operations, respectively. It can be stated that the spirit of the VIC method is to evade the high cost in computing the Biot–Savart integral in the meshfree methods while enjoying their features [27].

Birdsall and Fuss introduced the VIC method to solve plasma problems [28], and then Christiansen adapted it to simulate the inviscid incompressible flows [29]. Subsequently, Cottet and Koumoutsakos [30] altered it to simulate the viscous incompressible flows. Coquerelle and Cottet [31] combined it with a penalization technique (a type of immersed boundary method) to investigate the flow around solid obstacles. This method was extended to simulate the particle–laden [32] and gas–liquid [25, 27, 33] two-phase flows. In this method, several models can be used to calculate the vortex diffusion such as random walk [34], core spreading [35, 36], Fishelov [37], diffusion velocity [38], redistribution [39], particle strength exchange [40, 41] and staggered-grid finite difference [24, 25, 27, 33]. These models have a low accuracy [34], overlap issues (distorted particles) [35, 36, 38], great expense with a nice order of particles [39, 40, 41], high dissipation errors [24, 25, 27, 33]. In this study, the 27-point and conservation schemes are introduced to calculate the vortex diffusion and stretching, respectively.

In many practical situations of industrial interest, the flows are often at high Re. These flows are turbulent, containing a wide range of length scales, from the largest coherent structures to the smallest dissipation scales (see Mansfield et al. [42], Chatelain et al. [43], and Winckelmans et al. [3]). The grid used in simulations often can not capture the smallest scales. Hence, the solver for the Navier–Stokes equations needs to be completed with a sub-grid scale (SGS) model that correctly dissipates the energy at the captured smallest scales to take into account the effects of the uncaptured scales. There are a few research works on this topic, in which the turbulent models built are based on the meshfree methods. Cocle et al. [44] employed the SGS effective stress tensor model directly coupled with the velocity–vorticity equation. Chatelain et al. [43] used a hyper- and low-viscosity SGS model, based on the finite difference schemes with the VIC method for validation. Mansfield et al. [42, 45] applied the subfilter-scale (SFS) vorticity stress to account for the effects of unresolved velocity and vorticity fluctuations. The SFS model is combined with a pure Lagrangian vortex method, in which the velocity computation is performed using the Biot–Savart law to resolve the smallest structures of trailing wake vortex. In this study, the authors combine the SFS model with the VIC method (LVIC) for the viscous incompressible flows. It takes advantage of the VIC method, compared to the pure Lagrangian vortex methods, as mentioned above. In addition, the LVIC is an efficient solver that can be implemented using parallel computers, supporting the high Re flow simulations found in engineering. This method is then applied to simulations of a vortex ring's impingement on a vortex tube to clarify the aspects of the reconnection of these two vortices. The rest of this paper is organized as follows: section 2 expresses the governing equations, section 3 describes the numerical method, section 4 gives the discussions on results, followed by the conclusions in section 5.

2 Governing equations

The flow of a viscous incompressible fluid in a domain $\boldsymbol{\Omega} \in \mathbb{R}^3$ is described by the mass and momentum Navier–Stokes equations as

$$\nabla \cdot \boldsymbol{u} = 0, \ \texttt{for}\ \boldsymbol{x} \in \boldsymbol{\Omega}\ ,\ t \in \mathbb{R}_0^+ \tag{1}$$

$$\frac{\partial \boldsymbol{u}}{\partial t} + (\boldsymbol{u} \cdot \nabla)\boldsymbol{u} = -\frac{1}{\rho}\nabla p + \nu \nabla^2 \boldsymbol{u} + \boldsymbol{g}, \ \texttt{for}\ \boldsymbol{x} \in \boldsymbol{\Omega}\ ,\ t \in \mathbb{R}_0^+ \tag{2}$$

where coordinate $\boldsymbol{x} = (x, y, z)$, velocity field $\boldsymbol{u} = (u, v, w)$, fluid density $\rho \in \mathbb{R}^+$, pressure $p \in \mathbb{R}^3$, kinematic viscosity $\nu \in \mathbb{R}^+$, time t, and gravitational acceleration $\boldsymbol{g}$. The momentum equation in the velocity–vorticity form is obtained applying the curl operation on sides of Eq. (2) as

$$\frac{\partial \boldsymbol{\omega}}{\partial t} + (\boldsymbol{u} \cdot \nabla)\boldsymbol{\omega} = \nu \nabla^2 \boldsymbol{\omega} + (\boldsymbol{\omega} \cdot \nabla)\boldsymbol{u} \tag{3}$$

where the vorticity $\boldsymbol{\omega}$ is expressed as

$$\boldsymbol{\omega} = \nabla \times \boldsymbol{u} \tag{4}$$

The second term on the left, and the first and second terms on the right of Eq. 3 are the vortex convection, diffusion and stretching, respectively. The vector velocity can be resolved into the sum of an irrotational (free-curl) and a solenoidal (divergence-free) vector fields based on the fundamental theorem of vector calculus as

$$\boldsymbol{u} = \nabla \phi + \nabla \times \boldsymbol{\psi} \tag{5}$$

where ϕ and $\boldsymbol{\psi}$ are scalar and vector potentials of the vector velocity, respectively. Applying the curl operation on sides of Eq. (5) and substituting properties $\nabla \times (\nabla \phi) = 0$ and $\nabla \cdot \boldsymbol{\psi} = 0$ into the results, the vector Poisson equation for the vector potential is obtained as

$$\nabla^2 \boldsymbol{\psi} = -\boldsymbol{\omega} \tag{6}$$

By substituting the velocity equation, Eq. (5), into the continuity equation, Eq. (1), the Laplace equation for the scalar potential is written as

$$\nabla^2 \phi = 0 \tag{7}$$

3 Numerical method

3.1 Vortex-in-cell method

The VIC method discretizes the fluid into vortex particles p at the position $\boldsymbol{x}_p$, moving at the velocity $\boldsymbol{u}(\boldsymbol{x}_p)$ and carrying the vorticity $\boldsymbol{\omega}(\boldsymbol{x}_p)$. The particle velocity $\boldsymbol{u}(\boldsymbol{x}_p)$ is the flow velocity at the particle location. From the momentum equation, Eq. (3), the motion of the vortex particles in the Lagrangian frame can be expressed as

$$\frac{d\boldsymbol{x}_p}{dt} = \boldsymbol{u}(\boldsymbol{x}_p) \tag{8}$$

$$\frac{d\boldsymbol{\omega}(\boldsymbol{x}_p)}{dt} = \nu \nabla^2 \boldsymbol{\omega}(\boldsymbol{x}_p) + \big(\boldsymbol{\omega}(\boldsymbol{x}_p)\cdot\nabla\big)\boldsymbol{u}(\boldsymbol{x}_p) \tag{9}$$

Eq. (9) is rewritten in the conservation form of the vortex stretching, due to $\nabla\cdot\boldsymbol{u} = 0$ and $\nabla\cdot\boldsymbol{\omega} = 0$, as

$$\frac{d\boldsymbol{\omega}(\boldsymbol{x}_p)}{dt} = \nu \nabla^2 \boldsymbol{\omega}(\boldsymbol{x}_p) + \nabla\cdot\big(\boldsymbol{\omega}(\boldsymbol{x}_p)\boldsymbol{u}(\boldsymbol{x}_p)\big) \tag{10}$$

The particles are initially distributed at the regular grid, at which their vorticities are updated using Eq. (10) to express the vortex diffusion and stretching. The particles move to the Lagrangian locations $\boldsymbol{x}_p$ by Eq. (8). The particle velocity $\boldsymbol{u}(\boldsymbol{x}_p)$ in Eqs. (8) and (10) is obtained using Eq. (5), where the vector and scalar potentials, $\boldsymbol{\psi}$ and ϕ, are gained solving the Poisson and Laplace equations, Eqs. (6) and (7), respectively. The particles are then redistributed onto the grid nodes $\boldsymbol{x}_q$, at which their vorticities are interpolated from those at the Lagrangian locations as

$$\boldsymbol{\omega}(\boldsymbol{x}_q) = \sum_p^{N_p} \boldsymbol{\omega}(\boldsymbol{x}_p) W\Big(\frac{x_q - x_p}{\Delta x}\Big) W\Big(\frac{y_q - y_p}{\Delta y}\Big) W\Big(\frac{z_q - z_p}{\Delta z}\Big) \tag{11}$$

where the grid nodes $\boldsymbol{x}_q = (x_q, y_q, z_q)$, the Lagrangian locations $\boldsymbol{x}_p = (x_p, y_p, z_p)$, Δx, Δy, Δz are sizes of a grid cell, N_p is the vortex particle number, and $W(x)$ is a kernel-interpolation function that was introduced by Monaghan for the smoothed-particle hydrodynamics methods [46] and used for the vortex methods [30] and expressed as

$$W(x) = \begin{cases} 1 - \frac{5}{2}|x|^2 + \frac{3}{2}|x|^3 & \text{if } |x| \leq 1 \\ \frac{1}{2}(2-|x|)^2(1-|x|) & \text{if } 1 < |x| \leq 2 \\ 0 & \text{if } |x| > 2 \end{cases} \tag{12}$$

By using this function, the first three flow momentum $\Big(M_0 = \int_\Omega \boldsymbol{\omega} dV,\ M_1 = \int_\Omega \boldsymbol{x}\times\boldsymbol{\omega} dV$, and $M_2 = \int_\Omega \boldsymbol{x}\times(\boldsymbol{x}\times\boldsymbol{\omega}) dV\Big)$ are conserved. The particle convection, Eq. (8), is solved using the second-order Runge–Kutta method as

$$\begin{cases} \boldsymbol{x}_p^* &= \boldsymbol{x}_q + \boldsymbol{u}(\boldsymbol{x}_q)\dfrac{\Delta t}{2} \\ \boldsymbol{x}_p &= \boldsymbol{x}_q + \boldsymbol{u}(\boldsymbol{x}_p^*)\Delta t \end{cases} \tag{13}$$

where $\boldsymbol{u}(\boldsymbol{x}_p^*)$ is interpolated from the velocity field at the grid using Eq. (11). In Eq. (10), the temporal variation is calculated using the second-order Adams–Bashforth method as

$$\boldsymbol{\omega}^{n+1}(\boldsymbol{x}) = \boldsymbol{\omega}^n(\boldsymbol{x}) + \Delta t\left(\frac{3}{2}Rhs^n - \frac{1}{2}Rhs^{n-1}\right) \tag{14}$$

where Rhs indicates the right-hand side of Eq. (10).

The vorticity is a solenoidal vector based on the fundamental fluid mechanics, i.e., $\nabla \cdot \boldsymbol{\omega} = 0$. However, calculating the flow momentum (Eq. (10)) and redistributing the vortex particles (Eq. (11)) on the grid generate numerical errors, the vorticity field does not satisfy to be a solenoidal vector. Therefore, the vorticity field needs to be recorrected in the calculation procedure. Two methods can amend the vorticity field, such as the projection method in which solving a Poisson equation is required, as detailed in ref. [25], and a method introduced in ref. [47], in which the vorticity is modified using Eq. (4). In this study, the vorticity field is recorrected using Eq. (4) after every 50 time steps.

3.2 Vortex diffusion

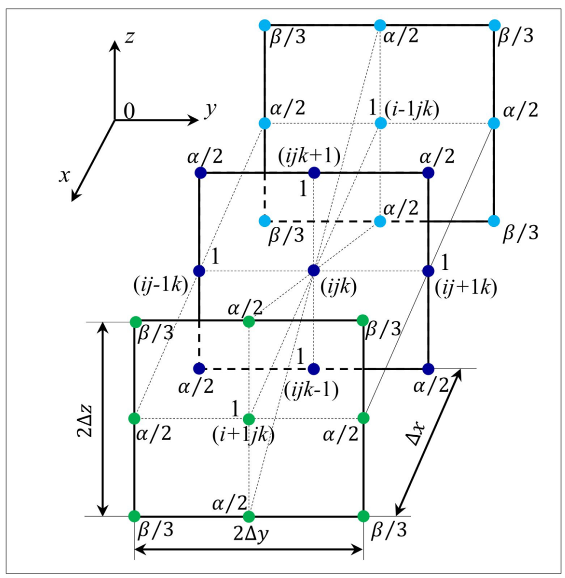

Figure 1: Schematics of 27 points and their impact factors on calculation of $\nabla^2\boldsymbol{\omega}$ at point (ijk)

The vortex diffusion is calculated using the 27-point schemes, in which 27 points surrounding the considered point are used to calculate the Laplace operation, as shown in Fig. 1. This scheme is based on the integral form of the Laplace operation [30, 40, 41, 47], written as

$$\nabla^2\boldsymbol{\omega}(\boldsymbol{x}) = \frac{2}{\epsilon^2}\int_{\mathbb{R}^3}\big(\boldsymbol{\omega}(\boldsymbol{y}) - \boldsymbol{\omega}(\boldsymbol{x})\big)\xi_\epsilon(\boldsymbol{x}-\boldsymbol{y})d\boldsymbol{y} \tag{15}$$

where $\xi(s) = -\dfrac{1}{s}d\gamma(s)ds$, $\gamma_\sigma(\boldsymbol{x}) = \dfrac{1}{\pi^{\frac{3}{2}}\sigma^3}exp^{-\frac{x^2}{\sigma^2}}$ and σ is cutoff value. $\nabla^2\boldsymbol{\omega}(\boldsymbol{x})$ is calculated based on the influence of $\boldsymbol{\omega}$ of the surrounding particles with the impact of their distance $|\boldsymbol{x}-\boldsymbol{y}|$. In the

VIC method, the flow momentum is calculated on the grid; therefore, the integral form of the Laplace operation is also approximated on the grid. $\nabla^2\boldsymbol{\omega}$ at the point (ijk) is computed as follows:

$$\nabla^2\boldsymbol{\omega} = W_1 + \alpha_1 W_2 + \alpha_2 W_3 \tag{16}$$

where

$$\begin{aligned}
W_1 =& \frac{(\boldsymbol{\omega}_{i+1jk} + \boldsymbol{\omega}_{i-1jk}) + (\boldsymbol{\omega}_{ij+1k} + \boldsymbol{\omega}_{ij-1k}) + (\boldsymbol{\omega}_{ijk+1} + \boldsymbol{\omega}_{ijk-1}) - 6\boldsymbol{\omega}_{ijk}}{\Delta^2} \\
W_2 =& \Bigg(\frac{(\boldsymbol{\omega}_{ij-1k+1} + \boldsymbol{\omega}_{ij+1k-1}) + (\boldsymbol{\omega}_{ij+1k+1} + \boldsymbol{\omega}_{ij-1k-1}) + (\boldsymbol{\omega}_{i+1jk+1} + \boldsymbol{\omega}_{i-1jk-1})}{2\Delta^2} \\
&+ \frac{(\boldsymbol{\omega}_{i-1jk+1} + \boldsymbol{\omega}_{i+1jk-1}) + (\boldsymbol{\omega}_{i+1j-1k} + \boldsymbol{\omega}_{i-1j+1k}) + (\boldsymbol{\omega}_{i+1j+1k} + \boldsymbol{\omega}_{i-1j-1k}) - 12\boldsymbol{\omega}_{ijk}}{2\Delta^2} \Bigg) \\
W_3 =& \Bigg(\frac{(\boldsymbol{\omega}_{i-1j-1k+1} + \boldsymbol{\omega}_{i+1j+1k-1}) + (\boldsymbol{\omega}_{i-1j+1k+1} + \boldsymbol{\omega}_{i+1j-1k-1})}{3\Delta^2} \\
&+ \frac{(\boldsymbol{\omega}_{i-1j-1k-1} + \boldsymbol{\omega}_{i+1j+1k+1}) + (\boldsymbol{\omega}_{i-1j+1k-1} + \boldsymbol{\omega}_{i+1j-1k+1}) - 8\boldsymbol{\omega}_{ijk}}{3\Delta^2} \Bigg)
\end{aligned}$$

and $\alpha_1 = 0.00077011858593$, $\alpha_2 = -\alpha_1$ and $\Delta x = \Delta y = \Delta z = \Delta$. Coefficients α_1 and α_2 are achieved by employing an iteration algorithm to impose the calculated results close to the analytical solution of the Laplace operation of a harmonic function.

3.3 Vortex stretching

The vortex stretching is computed using the conservation schemes. In this scheme, the vortex stretching component in the x-direction $\big(\nabla\cdot(\boldsymbol{\omega u})\big)_x$ is given as

$$\big(\nabla\cdot(\boldsymbol{\omega u})\big)_x = \delta_x(\omega_x u) + \delta_y(\omega_y u) + \delta_z(\omega_z u) \tag{17}$$

where the first term on the right of Eq. (17) is computed using approximations as

$$\delta_x f_{i+\frac{1}{2}} = \frac{-f_{i+2} + 27f_{i+1} - 27f_i + f_{i-1}}{24\Delta x} + \mathcal{O}(\Delta x)^4 \tag{18}$$

$$\delta_x f_i = \frac{-\delta_x f_{i-\frac{3}{2}} + 9\delta_x f_{i-\frac{1}{2}} + 9\delta_x f_{i+\frac{1}{2}} - \delta_x f_{i+\frac{3}{2}}}{16\Delta x} + \mathcal{O}(\Delta x)^4 \tag{19}$$

where $f = \omega_x u$. The first-order derivative of f with respect to x at point $x_{i+\frac{1}{2}}$ $(\delta_x f_{i+\frac{1}{2}})$ is calculated using Eq. (18), and $\delta_x f_i$ is then interpolated from $\delta_x f_{i+\frac{1}{2}}$ using Eq. (19).

3.4 Large eddy simulation combined with vortex-in-cell method

Consider a filtering function $H(\boldsymbol{x})$ with a length scale δ, the filtered flow quantity $\overline{\boldsymbol{\theta}(\boldsymbol{x})}$ is expressed as

$$\overline{\boldsymbol{\theta}(\boldsymbol{x})} = \int \boldsymbol{\theta}(\boldsymbol{y}) H\Big(\frac{\boldsymbol{x}-\boldsymbol{y}}{\delta}\Big)\frac{d\boldsymbol{y}}{\delta^3} \tag{20}$$

and the fluctuation is given as $\boldsymbol{\theta}'(\boldsymbol{x}) = \boldsymbol{\theta}(\boldsymbol{x}) - \overline{\boldsymbol{\theta}(\boldsymbol{x})}$. Applying the filtering operation on both sides of the vorticity equation, Eq. (3), the result is expressed as follows:

$$\frac{\partial\overline{\boldsymbol{\omega}}}{\partial t} + (\overline{\boldsymbol{u}}\cdot\nabla)\overline{\boldsymbol{\omega}} = \nu\nabla^2\overline{\boldsymbol{\omega}} + (\overline{\boldsymbol{\omega}}\cdot\nabla)\overline{\boldsymbol{u}} + \nabla\cdot(\Phi_{ij} - \Phi_{ji}) \tag{21}$$

The third term on the right of Eq. 21 expresses the sub-grid scale of the flow, where $\Phi_{ij} = \overline{\omega_i u_j} - \overline{\omega}_i \overline{u}_j$. Using properties of the Helmholtz stress related to gradient of the resolved vorticity, Φ_{ij} is modeled as

$$\Phi_{ij} = \nu_t \frac{\partial \overline{\omega}_i}{\partial x_j} \tag{22}$$

where ν_t is eddy diffusivity formulated by $\nu_t = (C_s\Delta)^2\sqrt{2S_{ij}S_{ij}}$, in which $\Delta = \sqrt[3]{\Delta x \Delta y \Delta z}$, $S_{ij} = \frac{1}{2}(\delta_j u_i + \delta_i u_j)$ and $C_s = 0.15$ given by Mansfield et al. [42]. $\dfrac{\partial \overline{\omega}_i}{\partial x_j}$ and $\delta_j u_i$ are approximated using Eqs. 18 and 19. Eq. (21) can be written in the Lagrangian reference frame of the vortex particles as

$$\frac{d\boldsymbol{x}_p}{dt} = \overline{\boldsymbol{u}(\boldsymbol{x}_p)} \tag{23}$$

$$\frac{d\overline{\boldsymbol{\omega}(\boldsymbol{x}_p)}}{dt} = \nu\nabla^2\overline{\boldsymbol{\omega}(\boldsymbol{x}_p)} + \nabla\cdot\Big(\overline{\boldsymbol{\omega}(\boldsymbol{x}_p)}\;\overline{\boldsymbol{u}(\boldsymbol{x}_p)}\Big) + \nabla\cdot\Big(\Phi_{ij}(\boldsymbol{x}_p) - \Phi_{ji}(\boldsymbol{x}_p)\Big) \tag{24}$$

3.5 Lagrangian method for scalar transport

In the VIC method, the vorticity is used to analyze the phenomena of vortex dynamics. However, in the impingement's case of two vortices, they deform. Clarifying the characteristics of the dynamics of their interaction is complex. Therefore, their dynamics are further tracked using two distinctive ink colors. The transport of ink color is governed by the convection equation for a passive scalar field α as

$$\frac{\partial\alpha}{\partial t} + (\boldsymbol{u}\cdot\nabla)\alpha = 0 \tag{25}$$

The passive scalar transport is solved using the mesh-free method, in which the scalar field is discretized into scalar particles carrying their scalar field. The above equation is written in the Lagrangian reference frame of scalar particles α as

$$\frac{d\alpha}{dt} = 0 \tag{26}$$

$$\frac{d\boldsymbol{x}_\alpha}{dt} = \boldsymbol{u}(\boldsymbol{x}_\alpha) \tag{27}$$

Eq. 27 is solved using the fourth-order Runge–Kutta method as

$$\boldsymbol{x}_\alpha^{n+1} = \boldsymbol{x}_\alpha^n + \frac{\Delta t}{6}\big[\boldsymbol{u}(\boldsymbol{x}_\alpha^n) + 2\boldsymbol{u}(\boldsymbol{x}_1) + 2\boldsymbol{u}(\boldsymbol{x}_2) + \boldsymbol{u}(\boldsymbol{x}_3)\big] \tag{28}$$

where $\boldsymbol{x}_\alpha^n$ and $\boldsymbol{x}_\alpha^{n+1}$ are the scalar particle position at nth and $(n+1)$th time steps, respectively, $\boldsymbol{x}_\alpha^n$ is known, Δt is time step, and $\boldsymbol{u}(\boldsymbol{x}_\alpha^n)$, $\boldsymbol{u}(\boldsymbol{x}_1)$, $\boldsymbol{u}(\boldsymbol{x}_2)$ and $\boldsymbol{u}(\boldsymbol{x}_3)$ are the particle velocity at locations $\boldsymbol{x}_\alpha^n$, $\boldsymbol{x}_1$, $\boldsymbol{x}_2$ and $\boldsymbol{x}_3$, respectively. These velocities are obtained from the flow velocity using the interpolation scheme, Eq. 11. The locations $\boldsymbol{x}_1$, $\boldsymbol{x}_2$ and $\boldsymbol{x}_3$ are calculated as follows:

$$\begin{aligned}
\boldsymbol{x}_1 &= \boldsymbol{x}_\alpha^n + \boldsymbol{u}(\boldsymbol{x}_\alpha^n)\frac{\Delta t}{2} \\
\boldsymbol{x}_2 &= \boldsymbol{x}_\alpha^n + \boldsymbol{u}(\boldsymbol{x}_1)\frac{\Delta t}{2} \\
\boldsymbol{x}_3 &= \boldsymbol{x}_\alpha^n + \boldsymbol{u}(\boldsymbol{x}_2)\Delta t
\end{aligned} \tag{29}$$

3.6 Numerical procedures

Supposing that the flow at $n\Delta t$ is known, the flow at $(n+1)\Delta t$ is computed using the following procedure:

• compute the sub-grid scale term in Eq. 24 using a model expressed by Eq. 22 to express the unresolved scales of the flow;

• compute the flow momentum in vorticity $\boldsymbol{\omega}(\boldsymbol{x}_p)$ using (24) to express the vortex diffusion, stretching and sub-grid scale of the flow;

• compute the vortex convection $\boldsymbol{x}_p$ using Eq. (23);

• redistribute the particles onto the grid nodes using Eq. (11);

• compute the vector potential $\boldsymbol{\psi}$ using the Poisson equation, Eq. (6);

• compute the velocity field $\boldsymbol{u}$ using Eq. (5);

• recorrect the vorticity field to satisfy the condition of a solenoidal vector using Eq. (4);

In this study, the spatial and temporal derivatives calculation has the fourth- and second-order accuracy, respectively. The irrotational vector field $\nabla\phi$ is set to be zero. The Poisson equation, Eq. (6), is solved employing the Fourier method, in which the Fourier transform is computed using the $FFTW3$ library [48]. The periodic condition is applied at six surfaces of the domain, at one of which five ghost points are set to treat this condition. For example, at the planes $x = x_{min}$ and $x = x_{max}$, the flow quantity $\boldsymbol{f}$ at the ghost points is respectively expressed as

$$\boldsymbol{f}(-i,j,k) = \boldsymbol{f}(nx-i,j,k) \qquad for\ 0 \le i \le 5\ \&\ i \in \mathbb{Z} \tag{30}$$

$$\boldsymbol{f}(nx+i,j,k) = \boldsymbol{f}(i,j,k) \qquad for\ 0 \le i \le 5\ \&\ i \in \mathbb{Z} \tag{31}$$

where $\boldsymbol{f} = (\boldsymbol{\omega}, \boldsymbol{\psi}, \boldsymbol{u})$ and nx is number of the grid nodes in the x direction. The passive scalar transport is calculated simultaneously with the flow solver.

4 Results and discussions

The current method is validated using simulations of Taylor–Green vortex flow (TGVF) at two Reynolds numbers (defined as $Re = 1/\nu$ [49, 50]) 200 and 2000. The scalar transport calculation is evaluated using simulations of the deformation of a scalar sphere immersed in an ideal vortex flow. Subsequently, characteristics of the interaction between two vortices are investigated using simulations of the collision of a vortex ring with a vortex tube.

4.1 Validation for calculation of vortex diffusion and stretching

First, the vortex diffusion and stretching calculations are evaluated using simulations of TGVF at $Re = 200$. The TGVF at the outset is expressed as [49, 50]

$$\left\{\begin{array}{lcl} u &=& \cos(x)\sin(y)\cos(z) \\ v &=& -\sin(x)\cos(y)\cos(z) \\ w &=& 0 \end{array}\right. \ \& \ \left\{\begin{array}{lcl} \omega_x &=& -\sin(x)\cos(y)\sin(z) \\ \omega_y &=& -\cos(x)\sin(y)\sin(z) \\ \omega_z &=& -2\cos(x)\cos(y)\cos(z) \end{array}\right. \tag{32}$$

where $x, y, z \in [0, 2\pi]$. Four grid resolutions of 32^3, 64^3, 96^3 and 128^3 are used for the convergence study, and the time step $\Delta t = 0.001$ is set in simulations.

Figs. 2 shows the time evolution of total enstrophy $En(t)$ and kinetic energy $Ek(t)$ of TGVF at $Re = 200$, in which $En(t)$ and $Ek(t)$ are expressed as

$$En(t) = \frac{1}{2L_xL_yL_z}\iiint_{\boldsymbol{\Omega}} \boldsymbol{\omega}^2 dV \tag{33}$$

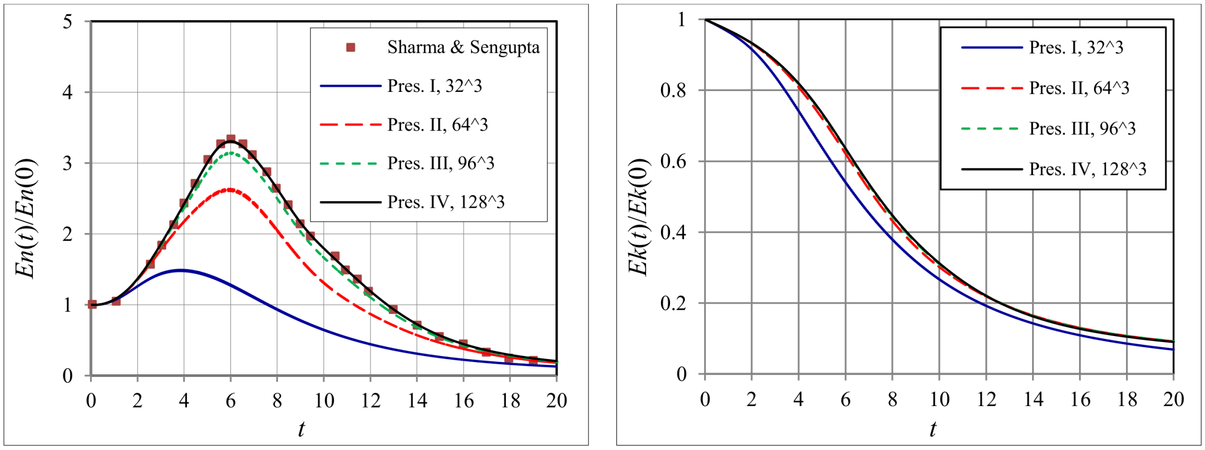

(a) (b)

Figure 2: Time evolution of the total enstrophy and kinetic energy of TGVF at $Re = 200$: (a) Total enstrophy; (b) Total kinetic energy. Grid nodes are 32^3, 64^3, 96^3 and 128^3. Present (Pres.) results of the enstrophy are compared to the existing simulation results [49] represented by a red-square-dotted curve [Reproduced from Sharm and Sengupta, with the permission of AIP Publishing]

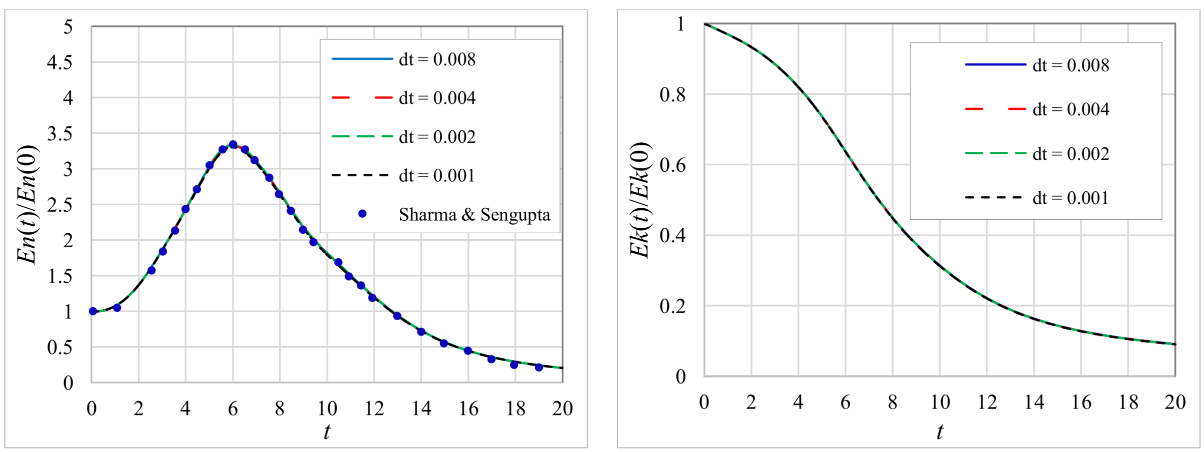

(a) (b)

Figure 3: Time evolution of the total enstrophy and kinetic energy of TGVF at $Re = 200$: (a) Total enstrophy; (b) Total kinetic energy. Grid nodes are 128^3, and four time steps used in simulations are $\mathrm{dt}(\Delta t) = 0.008$, 0.004, 0.002 and 0.001. Present (Pres.) results of the enstrophy are compared to the existing simulation results [49] represented by a red-square-dotted curve [Reproduced from Sharm and Sengupta, with the permission of AIP Publishing]

$$Ek(t) = \frac{1}{2L_xL_yL_z}\iiint_{\mathbf{\Omega}} \boldsymbol{u}^2 dV \tag{34}$$

where L_x, L_y and L_z are the computational domain sizes. In Fig. 2, the present results are obtained utilizing the 27-point and conservation schemes to calculate the vortex diffusion and stretching, respectively. The present results are convergent with the increase in grid resolution. The estimated enstrophy values at the grid node number of 128^3 have good agreement with those provided by Sharm and Sengupta [49]. Therefore, the calculation of vortex diffusion and stretching can be estimated using the 27-point and conservation schemes well. The effects of the time step on the time evolution of the total enstrophy and kinetic energy are also investigated, as shown in Fig. 3. It is observed that the curves of the total enstrophy and kinetic energy with the time steps of $\Delta t = 0.008$, 0.004, 0.002 and 0.001 seem to overlap and agree well with those given by Sharm and Sengupta [49]. Therefore, at this Re, the time step slightly affects the simulation results. The enstrophy increases remarkably from the beginning to $t = 6$, due to vortex stretching's effects greater than those of vortex diffusion. In this period, the vortices are stretched strongly because of their interaction, as further explained later. From $t = 6$, the enstrophy decreases, owing to a more significant effect of vortex diffusion. The total kinetic energy significantly reduces in whole time evolution because it is transferred to thermal energy.

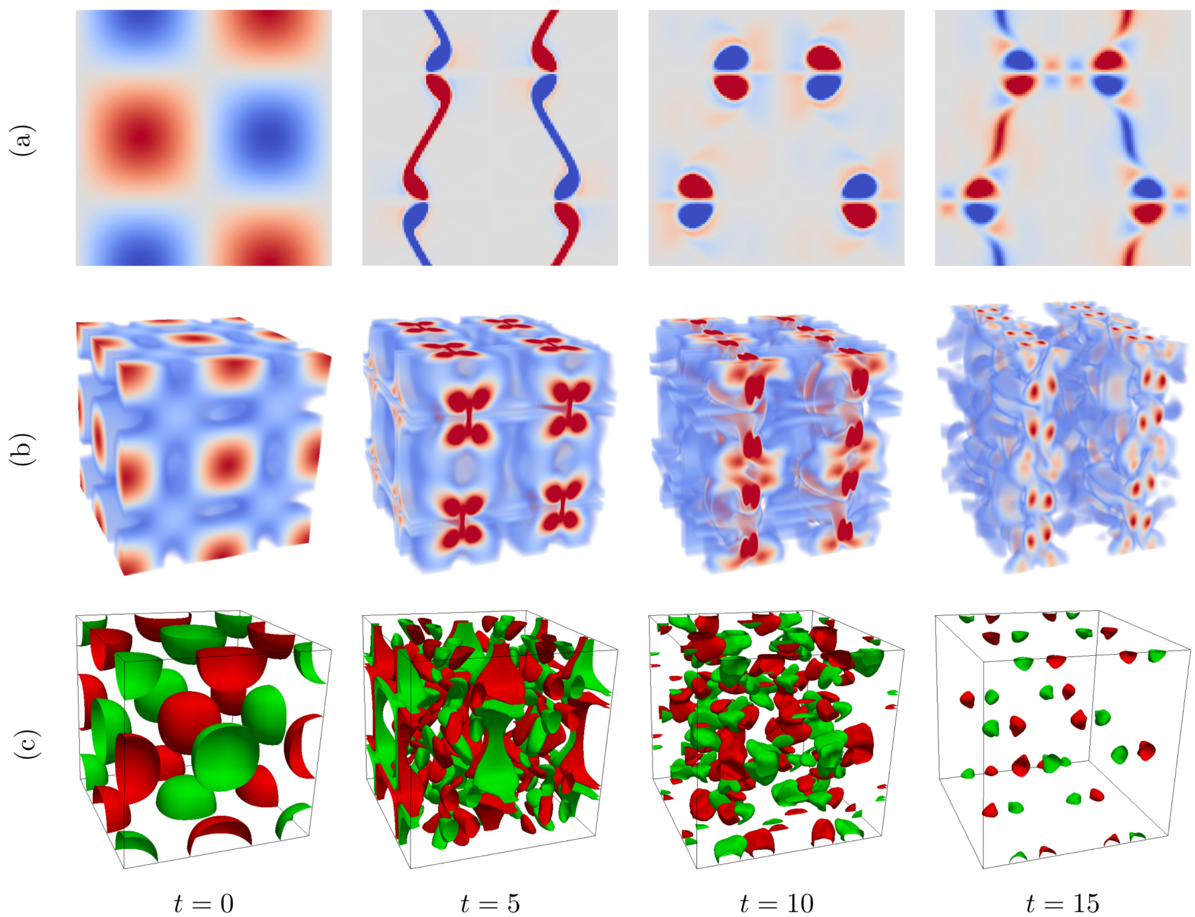

Figure 4: Time evolution of the vortex structure of TGVF at $Re = 200$: (a) Contours of ω_y are plotted in a range from -1 to 1 at plane $y = \pi/2$; positive and negative values are represented by blue and red colors, respectively; (b) Contour surfaces of $|\boldsymbol{\omega}|$ are plotted in a range from 0.5 to 2; (c) Isovalues of $\omega_z = \pm 1$ are represented using red and green surfaces, respectively

Fig. 4 shows the time evolution of the vortex structure of TGVF at $Re = 200$, in which plots of contours of the vorticity component ω_y, the vorticity magnitude $|\boldsymbol{\omega}|$, and isosurfaces of the vorticity component ω_z are shown in the first, second and third rows, respectively. At $t = 0$, the vortex structure is composed of large eddies arranged alternately. These eddies diffuse and are stretched strongly due to the fluid viscosity and three-dimensional flow effects, respectively, as seen at $t = 5$. The vortices break down into smaller vortices at $t = 10$. At $t = 15$, some low-energy vortices are formed, and the strength of these eddies reduces with time.

4.2 Validation for LES model

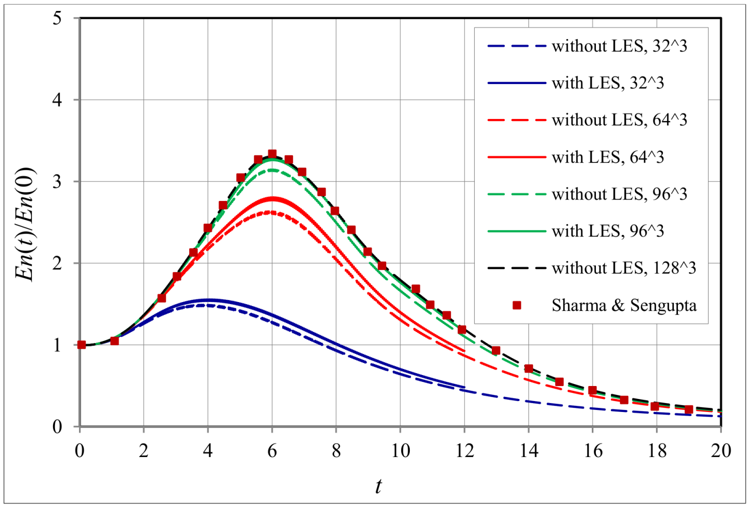

Figure 5: Time evolution of the enstrophy of TGVF at $Re = 200$: Grid nodes are 32^3, 64^3, 96^3 and 128^3. Present (Pres.) results are compared to the existing simulation results [49] represented by red-square-dotted curve [Reproduced from Sharm and Sengupta, with the permission of AIP Publishing]

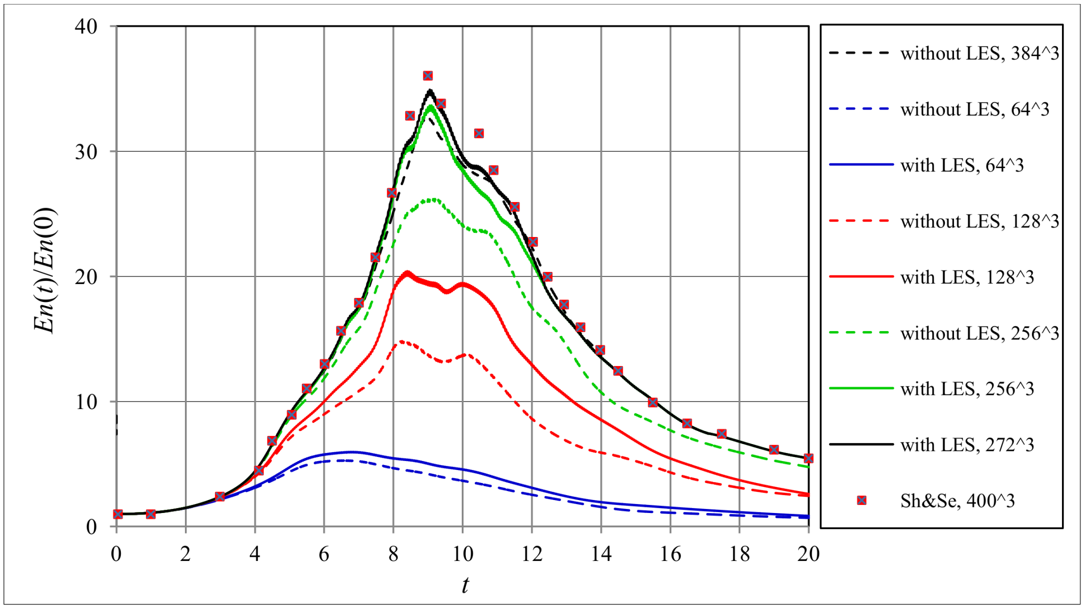

Figure 6: Time evolution of the enstrophy of TGVF at $Re = 2000$ obtained with and without LES model: Grid resolutions 64^3, 128^3, 256^3, 272^3 and 384^3; time step $\Delta t = 0.001$. Present results are compared to those by the existing simulation results [49] (denoted by Sh&Se in legend) with 400^3 grid nodes represented by a red-square-dotted curve [Reproduced from Sharm and Sengupta, with the permission of AIP Publishing]

The combination of the LES model with the VIC method is evaluated using simulations of TGVF at $Re = 200$ and 2000. Fig. 5 shows the time evolution of the enstrophy of TGVF at $Re = 200$. The present results are obtained with and without the LES model. At the grid resolution of 32^3, the LES model's effects on the results are trivial. That is because the small-scale fluid motions do not exist at this number of grid nodes. However, these effects increase significantly when the grid nodes are 64^3 and 96^3. Particularly, the results obtained using the LES model at grid nodes 96^3 are the same as those without the LES model at the grid nodes 128^3 and agree well with the simulation results by Sharm and Sengupta [49]. Therefore, using the LES model with a lower grid resolution can still capture the flow characteristics well.

The time evolution of the enstrophy of TGVF at $Re = 2000$ is shown in Fig. 6. At this Re, five grid resolutions are 64^3, 96^3, 128^3, 256^3, 272^3 and 384^3 used for simulations, as depicted in the figure legend. At the grid nodes of 64^3, the results obtained using the LES model are not so different from those without the LES model. However, this difference increases considerably at the grid nodes of 128^3 and 256^3. The rate of convergence of the method with the LES model is higher than those without the LES model. The results gained using the LES model with grid nodes of 256^3 and 272^3 approach those without the LES model with 384^3 and 400^3 ([49]) grid nodes, respectively. These results prove that the VIC method, combined with the LES model, can catch the global characteristics of this turbulent flow well. The total enstrophy of the flow increases strongly from the beginning to about $t = 9$, due to the effects of stretching of vortices caused by their interaction. From $t = 9$, the total enstrophy reduces significantly because the vortices break down into smaller vortices, as further explained later. The breakdown leads to a decrease in the vortex strength; in other words, the vorticity values reduce.

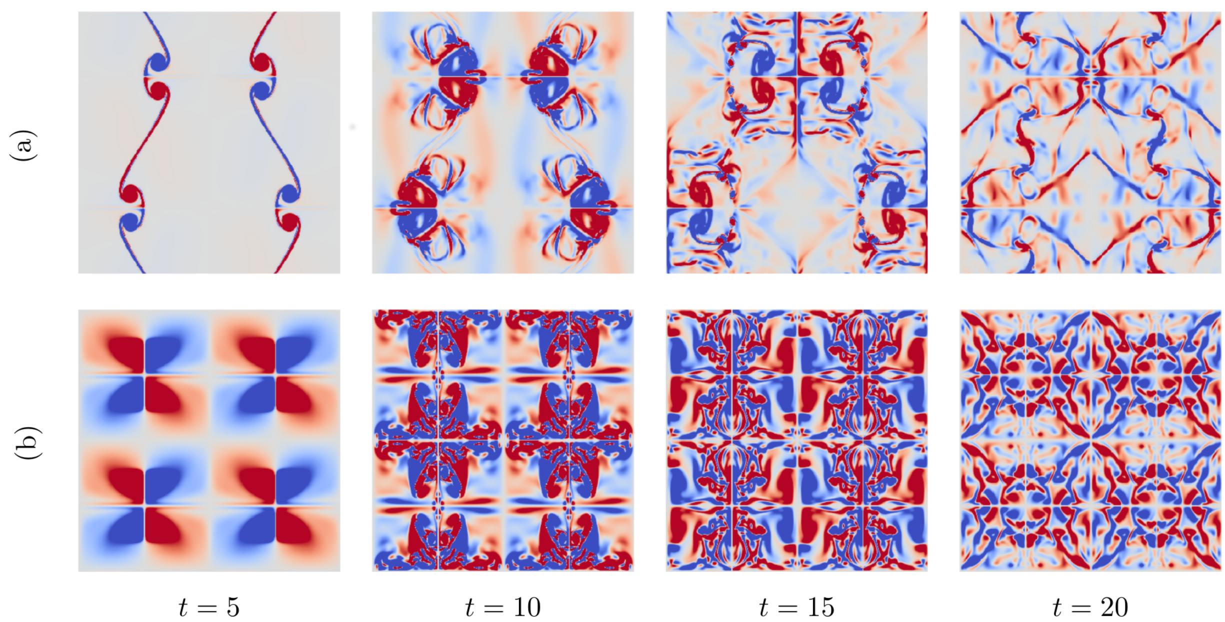

Figure 7: Time evolution of the vortex structure of TGVF at $Re = 2000$: (a) Contours of ω_y are plotted in a range from -1 to 1 at plane $y = \pi/2$; (b) Contours of ω_y are plotted in a range from -1 to 1 at plane $y = \pi$; the positive and negative values are represented by red and blue contours, respectively

Figs. 7 and 8 present the time evolution of the vortex structure of the TGVF at $Re = 2000$, in which plots of the vorticity component ω_y at planes $y = \pi/2$ and $y = \pi$ are shown in Fig. 7 while plots of the vorticity magnitude $|\boldsymbol{\omega}|$ and component ω_z are indicated in Fig. 8. At $t = 0$, the vortex structure is composed of large eddies arranging alternately. These eddies deform strongly because of their interaction at $t = 5$. At $t = 10$, the vortices continue deforming and break down into small vortices. At $t = 15$ and 20, these vortices continue to break down into smaller vortices and decay with

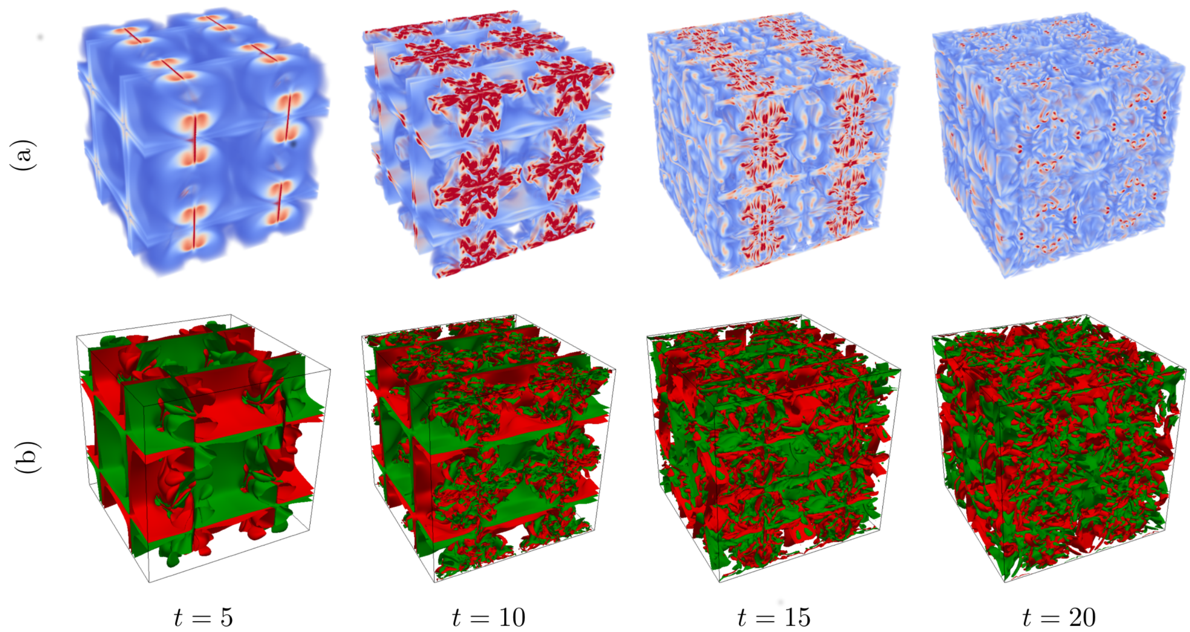

Figure 8: Time evolution of the vortex structure of TGVF at $Re = 2000$: (a) Contour surfaces of $|\boldsymbol{\omega}| = 0.5$–$5$; (b) Isosurvalues of $\omega_z = \pm 1$ are represented by the red and green surfaces, respectively

time.

Fig. 9 shows the energy spectrum $E(k)$ of the TGVF at $t = 10, 15$ and 20 at $Re = 2000$ using DNS and LES model, in which the $E(k)$ is calculated as follows [51]:

$$E(k) = 2exp\left(- \frac{\left(k\sqrt[3]{\Delta x \Delta y \Delta z}\right)^2}{2} \right) \left(\frac{1}{2\pi}\right)^2 \sum_{i=1}^{n_p} \sum_{j=i+1}^{n_p} \frac{(\Delta x \Delta y \Delta z)^2 \sin(k|\boldsymbol{x}_i - \boldsymbol{x}_j|)}{k|\boldsymbol{x}_i - \boldsymbol{x}_j|} \boldsymbol{\omega}_i \cdot \boldsymbol{\omega}_j \quad (35)$$

where $k = \overline{1, 2, ..., n}$ is wavenumbers, and n_p is number of vortex particles. The calculation of $E(k)$ with $\mathcal{O}(n_p^2)$ operations is expensive; therefore, the $E(k)$ is computed at several time steps. At the large scales (low wavenumbers) of vortex structures, the vortices are stretched because of their interaction. At intermediate scales (inertial subrange), there is a transfer of energy from large scales of vortex structures to small scales, known as energy cascade. From the figure, it is observed that in this subrange, the calculated energy spectrum obeys the $k^{-3/5}$ law of the Kolmogorov's hypothesis. At small scales (dissipation range), the energy of vortices is transferred into thermal energy. The energy spectrum decreases with time due to the effects of the fluid viscosity. The smallest scales corresponding to the highest wavenumber of the flow are observed at $t = 10$; in other words, the highest population of the small-scale vortex structures occurs. This population decreases with time, corresponding to a reduction in the intensity of vortices' interaction in the domain. The results in the inertial subrange obtained using LES model agree well with those using DNS. In the dissipation range, the LES model does not produce the highest wavenumber, as given using DNS; however, it can capture a large part of the flow scales in this range. Generally, the present method combined with the LES model can produce well the local characteristics of the turbulent flow at this Re.

4.3 Validation for calculation of scalar transport

Scalar transport governed by Eq. 25 is calculated using the Lagrangian method. This method is verified using a benchmark simulation of a scalar sphere's deformation in an ideal vortex flow [52]. The

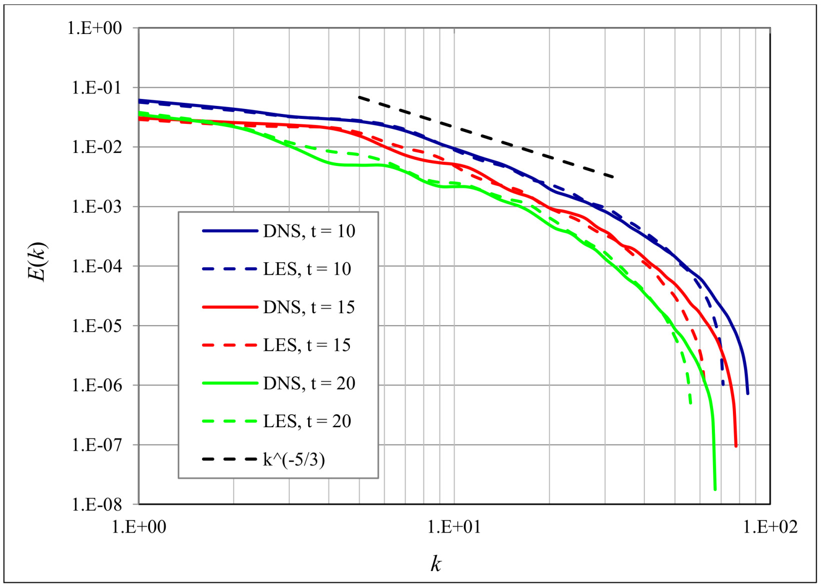

Figure 9: Energy spectrum $E(k)$ of TGVF at times $t = 10$, 15 and 20 at $Re = 2000$. Solid and dash curves are obtained using DNS with 384^3 and LES model with 272^3 grid nodes, respectively

sphere at the beginning has a radius of $r_0 = 0.15$ and is positioned at $(x_0, y_0, z_0) = (0.35, 0.35, 0.35)$. The vortex flow is described as

$$\begin{cases} u &= 2\sin^2(\pi x)\sin(2\pi y)\cos(2\pi z)\cos(\pi t/T) \\ v &= -\sin(2\pi x)\sin^2(\pi y)\sin(2\pi z)\cos(\pi t/T) \\ w &= -\sin(2\pi x)\sin(2\pi y)\sin^2(\pi z)\cos(\pi t/T) \end{cases} \tag{36}$$

where T is period of the flow, and $x, y, z \in [0, 1]$. The deformation of the scalar field is tracked by its boundary surface, in which 8984 scalar particles are distributed regularly on the spherical surface at $t = 0$. Time step is tested as $\Delta t = 0.001$, 0.005 and 0.01, and the domain is divided into 64^3 cube cells.

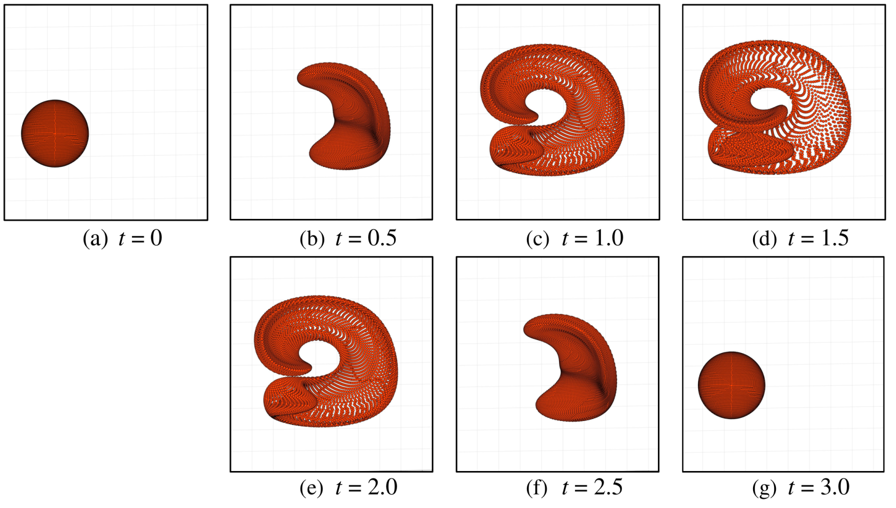

Figure 10: Time evolution of deformation of a scalar sphere in an ideal vortex flow with period $T = 3$. (a) $t = 0$, (b) $t = 0.5$, (c) $t = 1.0$, (d) $t = 1.5$, (e) $t = 2.0$, (f) $t = 2.5$ and (g) $t = 3.0$

Figs. 10 and 11 show the time evolution of deformation of a scalar field in an ideal vortex flow with

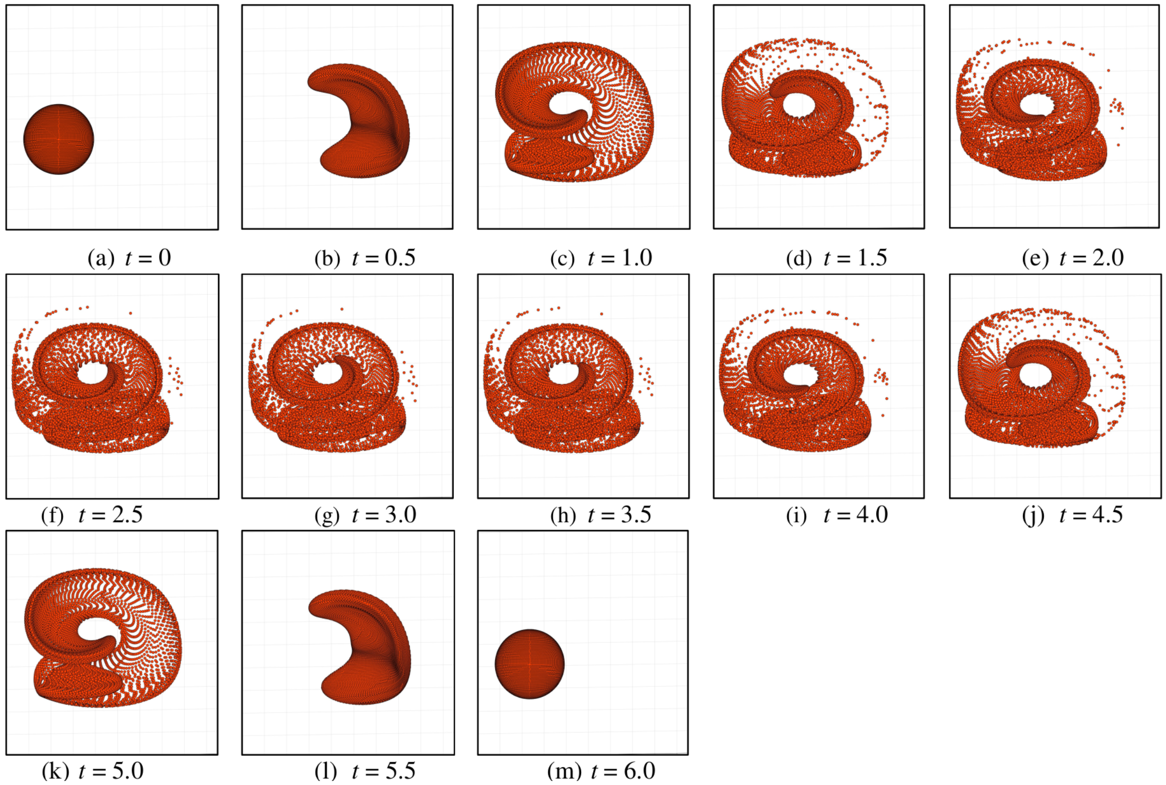

Figure 11: Time evolution of deformation of a scalar sphere in an ideal vortex flow with period $T = 6$. (a) $t = 0$, (b) $t = 0.5$, (c) $t = 1.0$, (d) $t = 1.5$, (e) $t = 2.0$, (f) $t = 2.5$, (g) $t = 3.0$, (h) $t = 3.5$, (i) $t = 4.0$, (j) $t = 4.5$, (k) $t = 5.0$, (l) $t = 5.5$ and (m) $t = 6.0$

period $T = 3$ and 6, respectively. At $t = 0$, the boundary of the scalar field is a spherical surface. This field deforms with the time evolution because of stretching by two vortices. The maximal deformation is at $t = T/2$, $t = 1.5$ and $t = 3$ in cases I and II, as shown in Figs. 10 and 11, respectively. Then, the scalar field boundary recovers gradually, and it is expected to reach its original state at $t = T$. The relative error between the calculated and analytical results at $t = T$ is defined as

$$\epsilon = \sum_{i=1}^{N_\alpha=8984} \frac{|\sqrt{(x_\alpha - x_0)^2 + (y_\alpha - y_0)^2 + (z_\alpha - z_0)^2} - r_0|}{r_0 N_\alpha} \tag{37}$$

The relative error is $\epsilon = 0.24\%$ for both study cases. The effects of the time step on the results are trivial. Thus, the solver for the convection equation, Eq. 25, can capture the passive scalar transport adequately.

4.4 Reconnection of a vortex ring and a vortex tube

The impingement of a vortex ring on a vortex tube is investigated to clarify two vortices' reconnection. A vortex ring at a Reynolds number ($Re_\Gamma^r = \Gamma_0^r/\nu$) is first simulated to verify the capability of the current method to capture this flow. A following Gaussian distribution function describes the vortex ring at the outset:

$$(\omega_r, \omega_\theta, \omega_z) = \left(0, \frac{\Gamma_0^r}{\pi\sigma^2} e^{-\frac{\rho^2(x,y,z)}{\sigma^2}}, 0\right) \tag{38}$$

where $\rho^2(x, y, z) = \left(r_0 - \sqrt{(x - x_0^r)^2 + (y - y_0^r)^2}\right)^2 + (z - z_0^r)^2$, ring radius $r_0 = 1$, core radius $\sigma = 0.24r_0$, initial circulation $\Gamma_0^r = 1$, initial position $(x_0^r, y_0^r, z_0^r) = (0, 0, 3r_0)$. The dimensionless variables are defined as $\boldsymbol{x}^* = \boldsymbol{x}/r_0$, $\boldsymbol{u}^* = \boldsymbol{u}r_0/\Gamma_0$, $t^* = t\Gamma_0/r_0^2$, $\boldsymbol{\omega}^* = \boldsymbol{\omega}r_0^2/\Gamma_0$, $\nabla^* = r_0\nabla$ and $Re_\Gamma = \Gamma_0/\nu$. The flow momentum, Eq. 21, is rewritten in the dimensionless form as

$$\frac{\partial\overline{\boldsymbol{\omega}^*}}{\partial t^*} + (\overline{\boldsymbol{u}^*}\cdot\nabla^*)\overline{\boldsymbol{\omega}^*} = \frac{1}{Re_\Gamma}\nabla^{*2}\overline{\boldsymbol{\omega}^*} + (\overline{\boldsymbol{\omega}^*}\cdot\nabla^*)\overline{\boldsymbol{u}^*} + \nabla^*\cdot(\Phi^*_{ij} - \Phi^*_{ji}) \tag{39}$$

The ring moves vertically downward at $Re^r_\Gamma = 10000$. The non-dimensional time step (Δt^*) is set to be 0.002, and a computational domain $(-2.5r_0, 2.5r_0)\times(-5r_0, 5r_0)\times(-5r_0, 5r_0)$ is discretized into cube cells. Four grid resolutions are used for the convergence study, as explained later.

Figs. 12, 13 and 14 (a) show the time evolution of the total enstrophy, kinetic energy, effects of the vortex diffusion, stretching, sub-grid scale terms on the rate of change of enstrophy. The effects of the vortex diffusion, stretching, and sub-grid scale terms on the rate of change of enstrophy are formulated by Eq. 46, as shown in the appendix A. From these figures, it is observed that the simulation results are convergent with the increase in the grid resolution. The results using $150\times300\times300$ grid nodes is close to those using $160\times320\times320$ grid nodes. Therefore, the grid resolution $160\times320\times320$ is used for other simulations. The total enstrophy slightly increases in the early stage, owing to the effects of the vortex stretching and sub-grid scale term greater than those of the vortex diffusion, and then it decreases. It is noted that the vortex diffusion causes a decrease in the total enstrophy while the vortex stretching and sub-grid scale term enhance the values of the vorticity, as shown in Figs. 13 and 14 (a). The kinetic energy gradually reduces in the whole time evolution because it is transferred into thermal energy.

Fig. 14 (b) shows the time evolution of vertical displacement of the vortex ring, where the displacement is expressed as

$$Z_c(t^*) = \int z^*\omega^*_y dx^* dz^* \Big/ \int \omega^*_y dx^* dz^* \tag{40}$$

The ring moves vertically downward at an estimated speed of $u^*_T = 0.2202$. Moreover, the translation velocity of a Gaussian vortex ring can be calculated using the formula as [53]

$$u^*_T = \frac{\Gamma_0}{4\pi r_0}\left(\ln\frac{8r_0}{\sigma} - 0.558\right) \tag{41}$$

The relative error of the translation velocity values obtained from the simulation and Eq. 41 is 4 %. Therefore, at this grid resolution and time step, the method can produce the characteristics of the vortex ring at this Re^r_Γ well. Fig. 15 shows contours of Q values representing the local balance between the shear strain and vorticity magnitude [54] and distribution of the flow velocity on the x-z plane at $t^* = 30$. Q is expressed as $Q = 0.5(||\bar{\Omega}||^2 - ||\bar{S}||^2)$, where $S_{ij} = 0.5(\delta^*_j u^*_i + \delta^*_i u^*_j)$ and $\Omega_{ij} = 0.5(\delta^*_j u^*_i - \delta^*_i u^*_j)$. The vortex ring shape is almost conserved in the whole time evolution.

The characteristics of the interaction of a vortex ring and a vortex tube are investigated. The Gaussian distribution expresses the vortex tube at the beginning as

$$(\omega_x, \omega_y, \omega_z) = \left(0, \frac{\Gamma^t_0}{\pi\sigma^2}e^{-\frac{R^2(x,y,z)}{\sigma^2}}, 0\right) \tag{42}$$

where $R^2(x,y,z) = (x - x^t_0)^2 + (z - z^t_0)^2$, core radius $\sigma = 0.24r_0$, and initial position $(x^t_0, y^t_0, z^t_0) = (0, 0, r_0)$. The circulation ratios of the ring to tube are investigated in three cases as $\Gamma^t_0/\Gamma^r = 0.1$, 0.5 and 1. Re^r_Γ is fixed to be 10000, and Re^t_Γ are 1000, 5000, 10000. The computational domain and time step are set as the same as in the case of simulation of a single vortex ring.

Figs. 16 and 17 show the time evolution of the interaction of a vortex ring and a vortex tube, in which the structure of vortices are described using the contours of Q values and the helicity $|\boldsymbol{u}^*\times\boldsymbol{\omega}^*|$

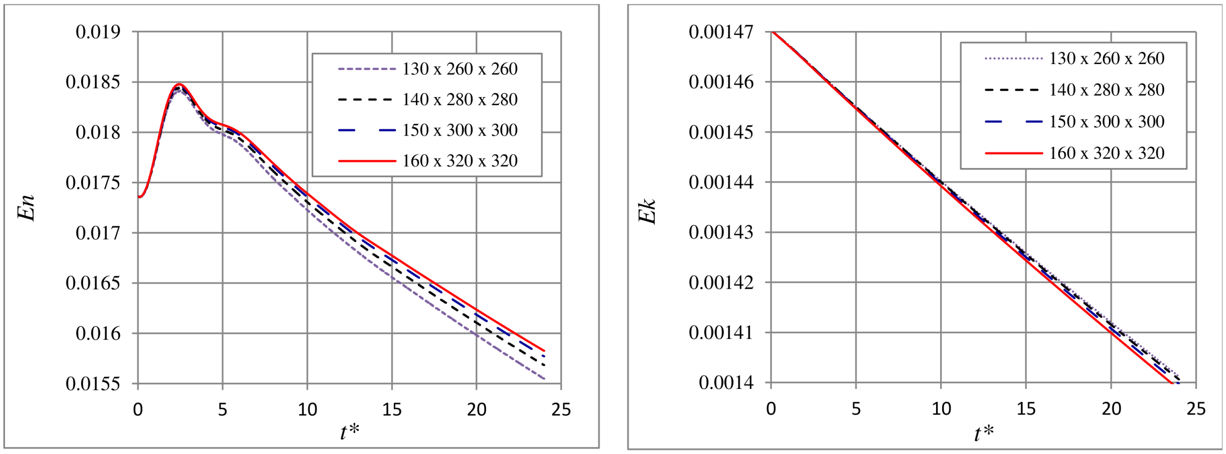

(a) (b)

Figure 12: Time evolution of total enstrophy and kinetic energy of the flow induced by a single vortex ring motion at $Re_{\Gamma}^{r} = 10000$: (a) total enstrophy, En; (b) total kinetic energy, Ek. Grid nodes are $130 \times 260 \times 260$, $140 \times 280 \times 280$, $150 \times 300 \times 300$ and $160 \times 320 \times 320$

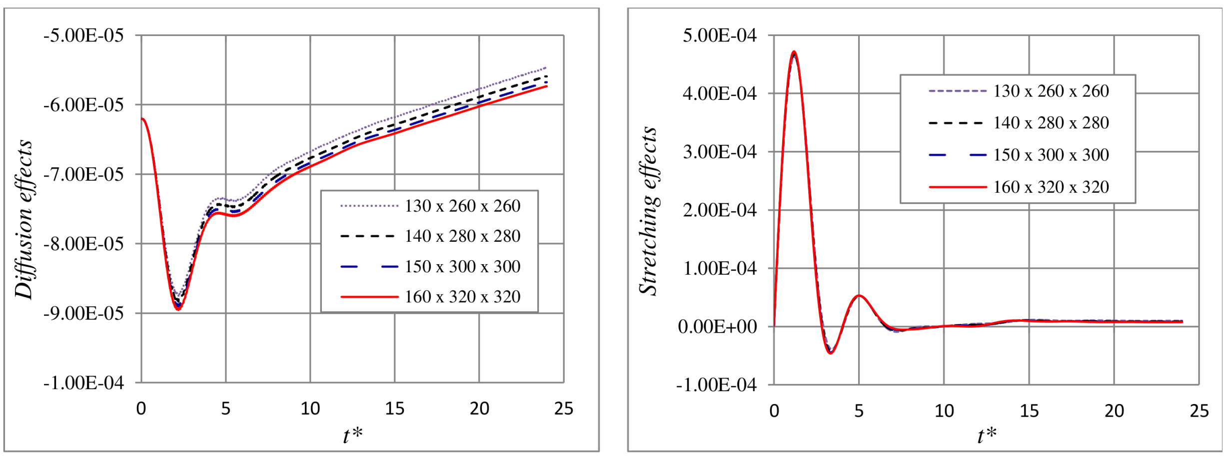

(a) (b)

Figure 13: Time evolution of the effects of vortex diffusion and stretching on rate of change of enstrophy of the flow induced by a single vortex ring motion at $Re_{\Gamma}^{r} = 10000$: (a) diffusion effects; (b) stretching effects

while their cores are expressed by local enstrophy values. In the case of $Re_{\Gamma}^{r} = 10000$ and $Re_{\Gamma}^{t} = 1000$, the ring rapidly moves toward the tube and impinges on it at $t^* = 8$. The ring shape is almost conserved in the whole time evolution. This is explained by the fact that the effects of the tube on the ring are trivial. The ring core slightly fluctuates at $t^* = 16$, and this fluctuation increases with time, as shown at $t^* = 20$, 24, and 28. In the impingement region, the tube's strength reduces, and the contours of Q representing the tube disappear, as seen at $t^* = 8$, 12 and 16. The tube breaks into two parts, and they are entrained by the ring wake, as observed at $t^* = 20$, 24, and 28. In the case of $Re_{\Gamma}^{r} = 10000$ and $Re_{\Gamma}^{t} = 5000$, the tube is deformed at $t^* = 8$ and 12, and a part of the tube is detached at $t^* = 16$. This detached part rolls around the ring, leading to the generation of vortices of small scales, as seen at $t^* = 20$. The tube reconnects at this time. The detached part of the tube continues to interact forcefully with the ring to induce the formation of vortices of various scales, as seen at $t^* = 24$ and 28. In the case of $Re_{\Gamma}^{r} = 10000$ and $Re_{\Gamma}^{t} = 10000$, the ring impinges on the tube at $t^* = 8$. At $t^* = 12$, the ring breaks into two parts, one of which interacts with the leaving part

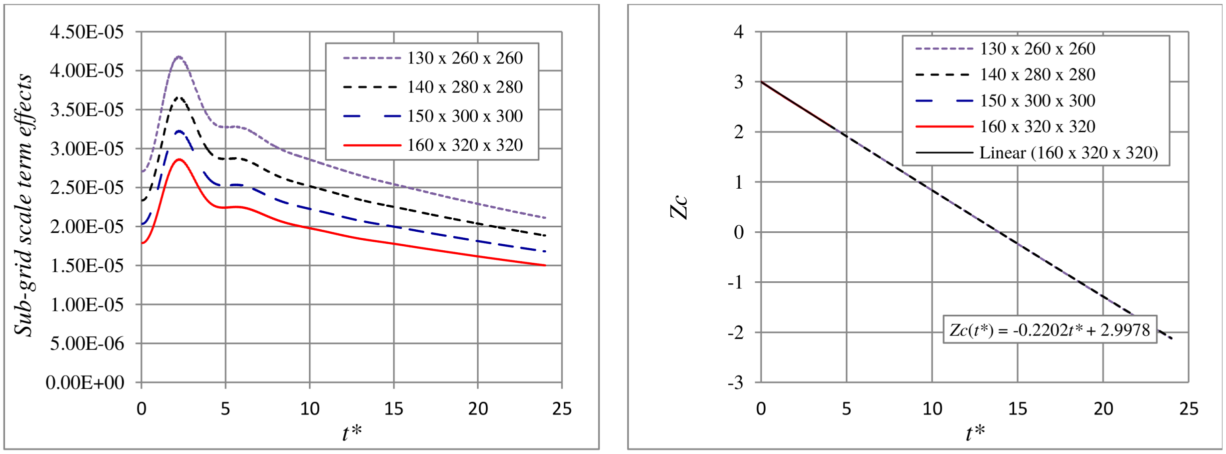

(a) (b)

Figure 14: (a) Time evolution of effects of sub-grid scale term on rate of change of enstrophy of the flow induced by a single vortex ring motion at $Re^r_\Gamma = 10000$. (b) Time evolution of vertical displacement of vortex ring; the displacement is determined as $Z_c(t^*) = -0.2202t^* + 2.9978$, as shown in the legend

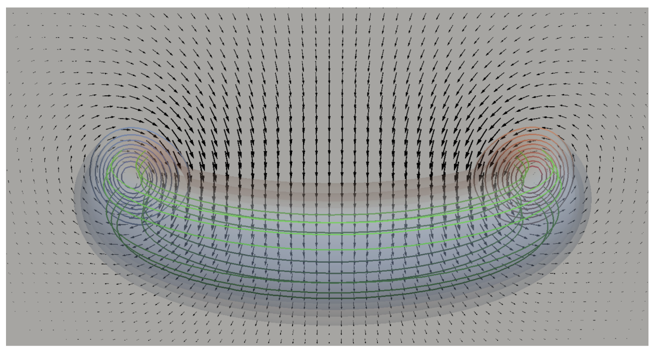

Figure 15: Contours of Q value and distribution of flow velocity on x-z plane passing through the vortex ring centerline at $t^* = 30$. $Q = 0.5(||\bar{\Omega}||^2 - ||\bar{S}||^2)$, where $S_{ij} = 0.5(\delta^*_j u^*_i + \delta^*_i u^*_j)$ and $\Omega_{ij} = 0.5(\delta^*_j u^*_i - \delta^*_i u^*_j)$

of the tube to form the secondary ring moving downward. This ring is unstable, deforms strongly at $t^* = 16$, and it is distorted at $t^* = 20, 24$ and 28. Another one replaces the leaving part of the tube to reconnect the tube at $t^* = 12$ and 16. This reconnected tube is twisted counterclockwise to the y-axis at $t^* = 20, 24$ and 28, leading to the generation of small-scale vortices around the tube. There are two strong interaction regions in which the ring impinges on the tube. The secondary ring stretches these interaction regions toward its motion to form large-scale vortices, as seen at $t^* = 16$ and 20. These vortices interact together and with the vortex wake formed behind the secondary ring to form the small-scale vortices, as seen at $t^* = 24$ and 28.

Fig. 18 depicts the time evolution of the Q and local helicity distribution ($H = \boldsymbol{u}^* \cdot \boldsymbol{\omega}^*$) representing twisting of the vortex structure. In the case of $Re^r_\Gamma = 10000$ and $Re^t_\Gamma = 1000$, the helicity is negligible in the period from $t^* = 0$ to $t^* = 20$. The entrained part of the tube is slightly twisted, as seen at $t^* = 24$ and 28. In the case of $Re^r_\Gamma = 10000$ and $Re^t_\Gamma = 5000$, the helicity appears in the connection regions at $t^* = 12$ and then spreads to both sides of the tube at $t^* = 16$, due to the effects of the ring wake. The detached part of the tube is twisted strongly because of the secondary ring's effects, as seen at $t^* = 16$. This detached part affects the secondary ring and generates the twisted small-scale vortices at $t^* = 20$. The helicity distribution is disturbed downstream, as seen at $t^* = 24, 28$. In the

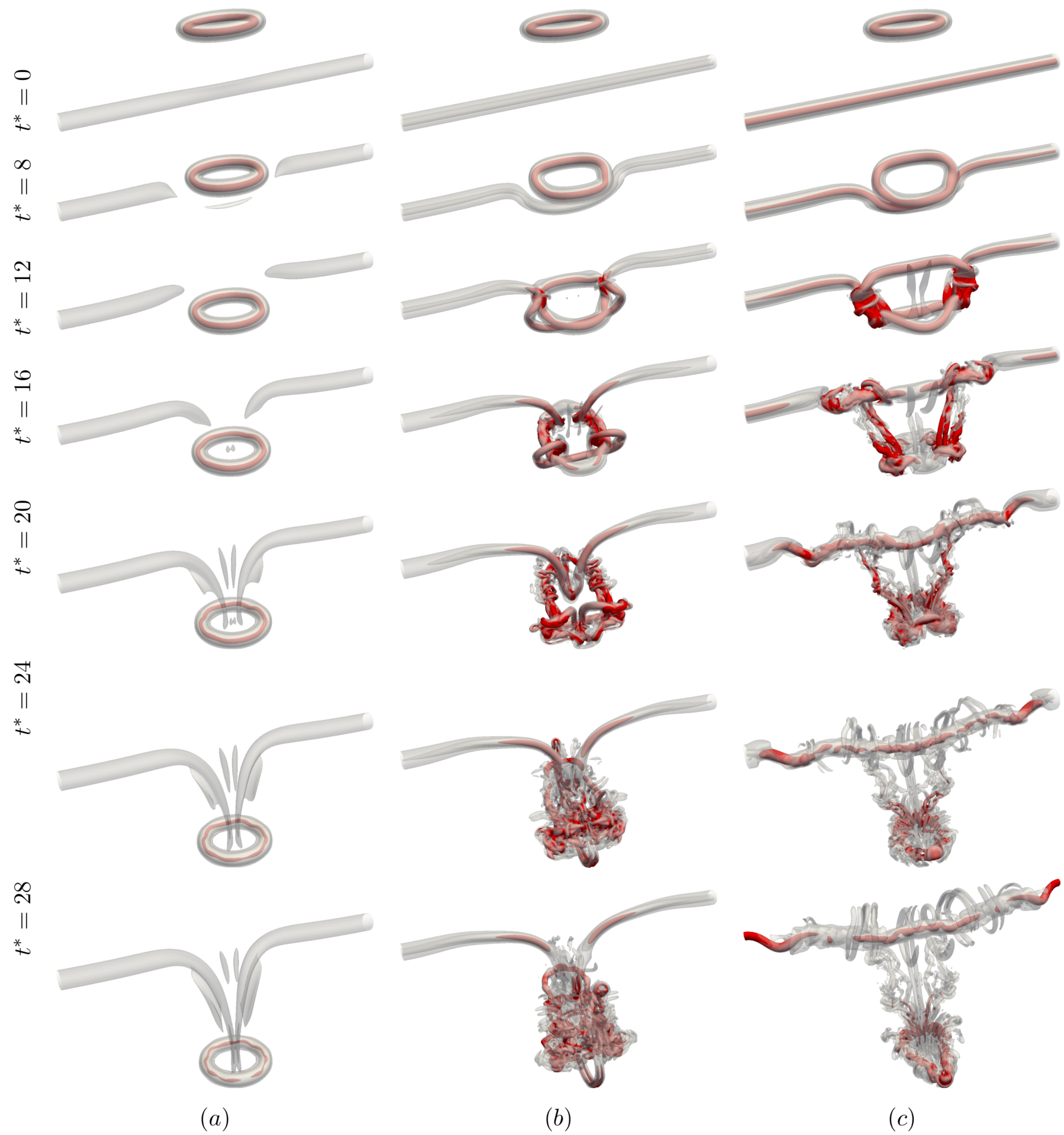

Figure 16: Time evolution of the interaction of a vortex ring and a vortex tube: gray surfaces represent isovalues of Q while red surfaces represent contours of local enstrophy $|\boldsymbol{\omega}^*|^2$. (a) $Re_\Gamma^r = 10000$ & $Re_\Gamma^t = 1000$; (b) $Re_\Gamma^r = 10000$ & $Re_\Gamma^t = 5000$; (c) $Re_\Gamma^r = 10000$ & $Re_\Gamma^t = 10000$

case of $Re_\Gamma^r = 10000$ and $Re_\Gamma^t = 10000$, the helicity appears at $t^* = 8$ in the connection regions, then increases significantly at $t^* = 12$. The secondary ring is twisted in the whole time evolution. The helicity on the tube moves far away from the connection points, as seen at $t^* = 20$, 24, and 28. At $t^* = 28$, the helicity on the tube is less; in other words, the tube is more stable.

Fig. 19 shows the vortex structure expressed in the vorticity component ω_z^* representing the stretching of vortices caused by three-dimensional effects of the flow at $t^* = 12$ and 14. In the case of $Re_\Gamma^r = 10000$ and $Re_\Gamma^t = 1000$, the vorticity component ω_z^* appears on the entrained part of the tube and is not formed on the ring; in other words, the three-dimensional effects of the flow are trivial. In the cases of $Re_\Gamma^r = 10000$ and $Re_\Gamma^t = 5000$ or $Re_\Gamma^t = 10000$, ω_z^* is formed on both the ring and tube. Especially, there are pairs of small-scale vortices with opposite signs of ω_z^* around the tube and behind

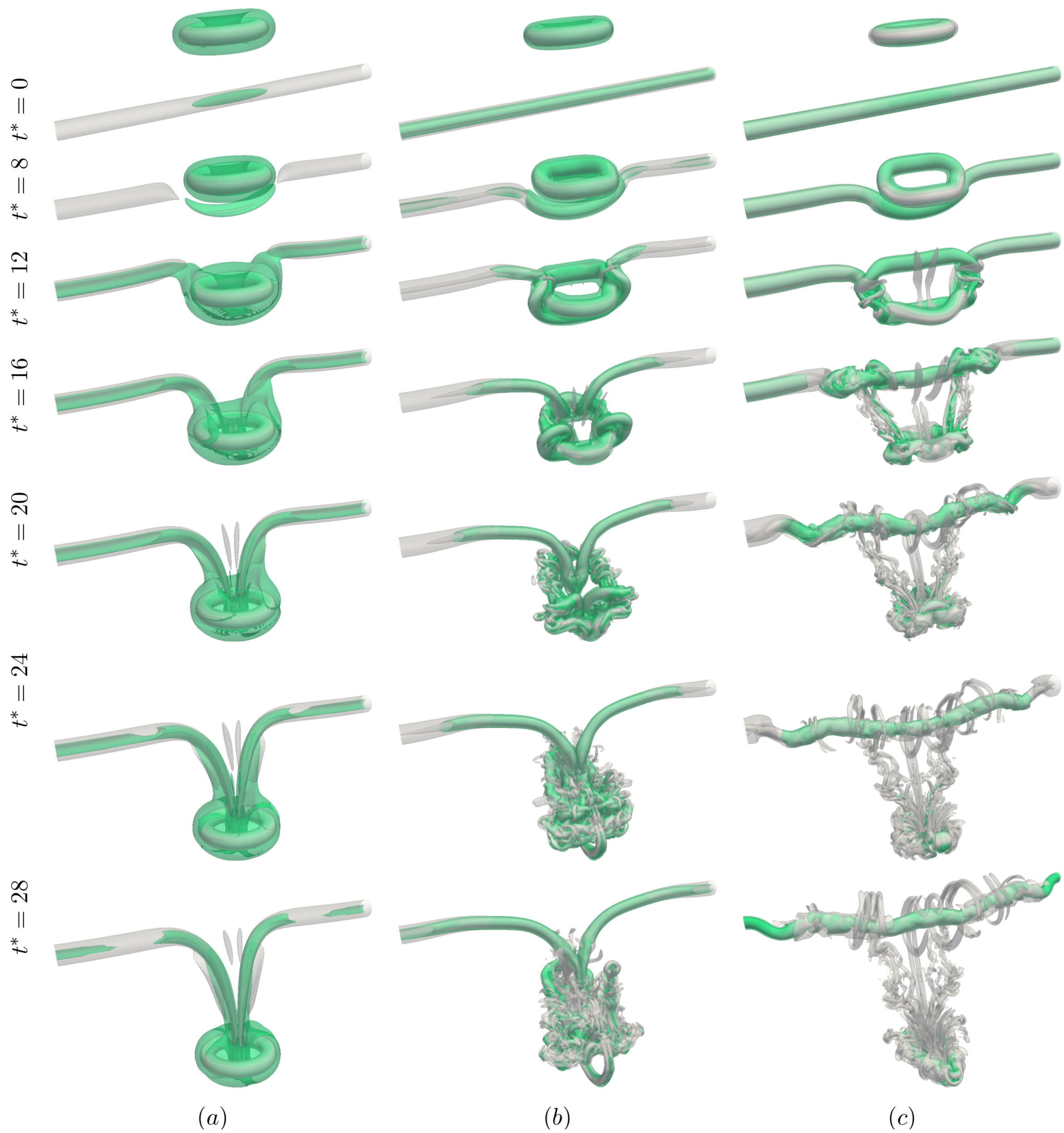

Figure 17: Time evolution of the interaction of a vortex ring and a vortex tube: gray surfaces represent isovalues of Q while red surfaces represent contours of local helicity $|\boldsymbol{u}^* \times \boldsymbol{\omega}^*|$. (a) $Re^r_\Gamma = 10000$ & $Re^t_\Gamma = 1000$; (b) $Re^r_\Gamma = 10000$ & $Re^t_\Gamma = 5000$; (c) $Re^r_\Gamma = 10000$ & $Re^t_\Gamma = 10000$

the secondary ring.

Fig. 20 shows the time evolution of the passive scalar particles utilized to track the dynamics of two vortices. The red and blue scalar particles represent the vortex ring and tube, respectively. In the case of $Re^r_\Gamma = 10000$ and $Re^t_\Gamma = 1000$, the particles move in an ordered pattern, as seen at $t^* = 0, 8,$ and 12. The tube-scalar particles are entrained by the ring, as observed at $t^* = 8, 20,$ and 28. The ring-scalar particles' order is slightly disturbed by the tube effects at $t^* = 20$ and 28. In the case of $Re^r_\Gamma = 10000$ and $Re^t_\Gamma = 5000$, the tube- and ring-scalar particles mix because of the appearance of the turbulent vortex structures, as seen at $t^* = 20$ and 28. In the case of $Re^r_\Gamma = 10000$ and $Re^t_\Gamma = 10000$, the breakdown and reconnection of the vortex ring and tube are clearly observed at $t^* = 16$, 20, and 28. A cluster of the red-ring particles replaces the blue-leaving-tube particles to reconstruct the tube.

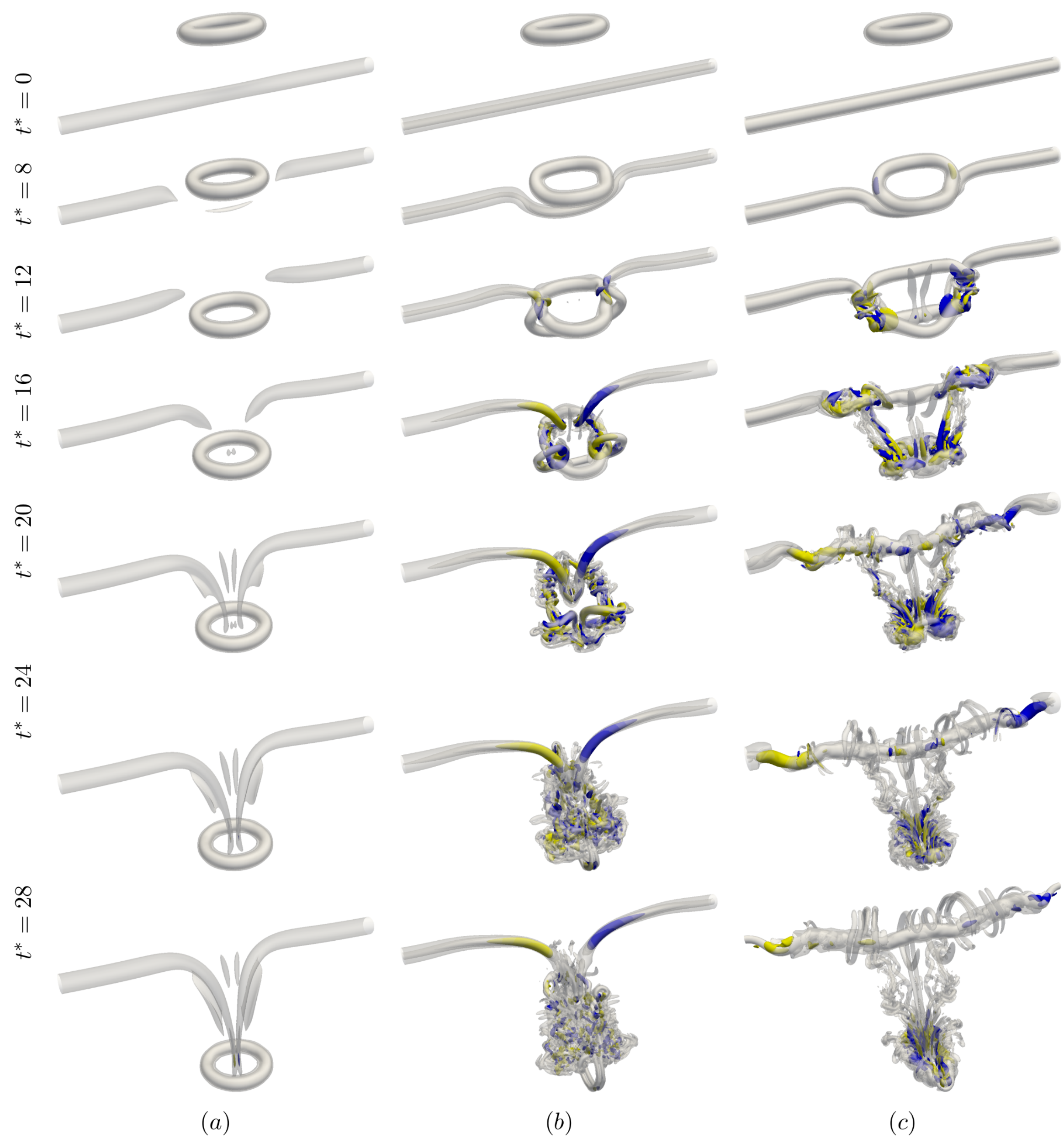

Figure 18: Time evolution of the interaction of a vortex ring and a vortex tube: gray surfaces represent isovalues of Q while yellow and blue surfaces represent those of positive and negative values of the local helicity ($H = \boldsymbol{u}^* \cdot \boldsymbol{\omega}^*$), respectively. (a) $Re_\Gamma^r = 10000$ & $Re_\Gamma^t = 1000$; (b) $Re_\Gamma^r = 10000$ & $Re_\Gamma^t = 5000$; (c) $Re_\Gamma^r = 10000$ & $Re_\Gamma^t = 10000$

Another cluster of the red-ring particles connects with the blue-leaving-tube particles to construct a new secondary ring. The red-ring and blue-tube particles behind the secondary ring are disturbed because of the effects of the turbulent structures induced by the interaction of the secondary ring wake with connection vortices.

Fig. 21 shows the energy spectrum of the flow induced by the interaction between a vortex ring and a vortex tube at $t^* = 0, 12, 20,$ and 28 in three simulation cases. In the case of $Re_\Gamma^r = 10000$ and $Re_\Gamma^t = 1000$, the energy does not change with time because the effects of the vortex tube on the vortex ring are trivial, and the small-scale vortex structures are not generated. This energy is dominated by the flow induced by the vortex ring motion. In the case of $Re_\Gamma^r = 10000$ and $Re_\Gamma^t = 5000$, the

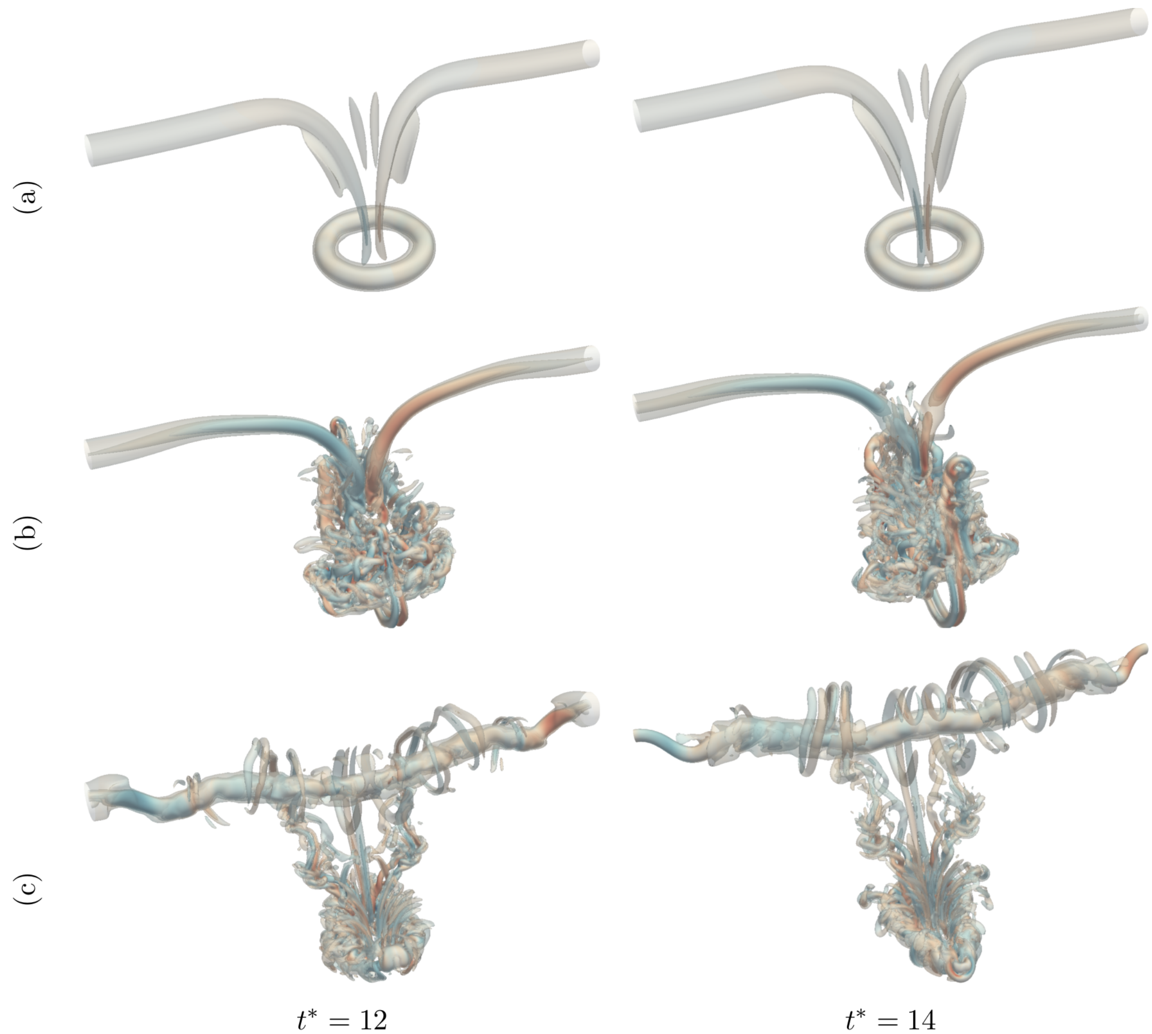

Figure 19: Time evolution of the interaction of a vortex ring and a vortex tube: Isovalues of Q are represented by gray surfaces while yellow and blue surfaces represent positive and negative values of ω_z^*. (a) $Re_\Gamma^r = 10000$ & $Re_\Gamma^t = 1000$; (b) $Re_\Gamma^r = 10000$ & $Re_\Gamma^t = 5000$; (c) $Re_\Gamma^r = 10000$ & $Re_\Gamma^t = 10000$

population of the small-scale vortex structures at the high wavenumbers increases, and the smallest-scale vortex is observed at $t^* = 28$. This is explained by the fact that the leaving part of the tube forcefully interacts with the ring in the whole time evolution. In the case of $Re_\Gamma^r = 10000$ and $Re_\Gamma^t = 10000$, the population of the small-scale vortex structure increases from the beginning to $t^* = 20$ before a reduction at $t^* = 28$. This is because after the reconnection, the secondary ring and tube become more stable. In the inertial subrange, the energy spectrum correlates with the wavenumbers by $E(k) \sim k^{-3/2}$. The present results do not fit the curve of $k^{-5/3}$ in the Kolmogorov's hypotheses because the current turbulent flow is not isotropic.

Fig. 22 shows a comparison of the energy spectrum of the flow induced by the interaction of a vortex ring at $Re_\Gamma^r = 10000$ and a vortex tube at $Re_\Gamma^t = 5000$ and 10000. It is observed that the energy of the large-scale vortices at the low wavenumbers ranging from 1 to 7 in the case of $Re_\Gamma^r = 10000$ and $Re_\Gamma^t = 10000$ is higher than that with $Re_\Gamma^r = 10000$ and $Re_\Gamma^t = 5000$. This is explained by the fact that the large-scale vortices at higher Re_Γ produce higher energy. However, with wavenumbers higher than 10, the energy of the small-scale vortices in the case of $Re_\Gamma^r = 10000$ and $Re_\Gamma^t = 10000$ is lower than with $Re_\Gamma^r = 10000$ and $Re_\Gamma^t = 5000$. This is because a strong interaction of a vortex ring and a

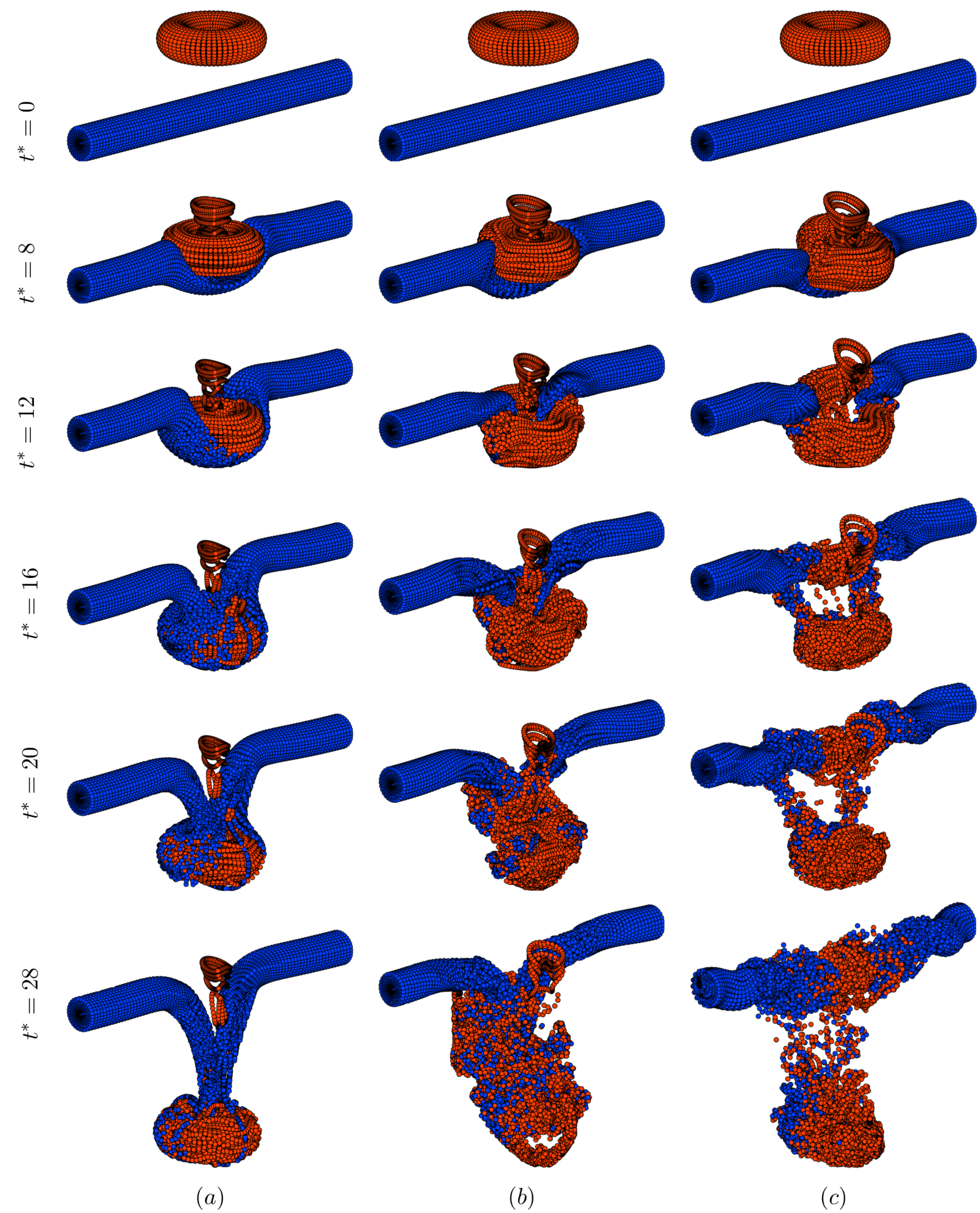

Figure 20: Time evolution of the interaction of a vortex ring and a vortex tube: Red and blue passive scalar particles represent the vortex ring and tube, respectively. (a) $Re^r_\Gamma = 10000$ & $Re^t_\Gamma = 1000$; (b) $Re^r_\Gamma = 10000$ & $Re^t_\Gamma = 5000$; (c) $Re^r_\Gamma = 10000$ & $Re^t_\Gamma = 10000$

vortex tube with $Re^r_\Gamma = 10000$ and $Re^t_\Gamma = 5000$ occurs after their collision while with $Re^r_\Gamma = 10000$ and $Re^t_\Gamma = 10000$, after the reconnection, the flow becomes more stable. The population of the small-scale vortex structures in the case of $Re^r_\Gamma = 10000$ and $Re^t_\Gamma = 5000$ is higher than those with $Re^r_\Gamma = 10000$ and $Re^t_\Gamma = 10000$. The smallest-scale vortex structure is observed with $Re^r_\Gamma = 10000$ and $Re^t_\Gamma = 5000$. It can state that that the most effective mixing is observed with $Re^r_\Gamma = 10000$ and

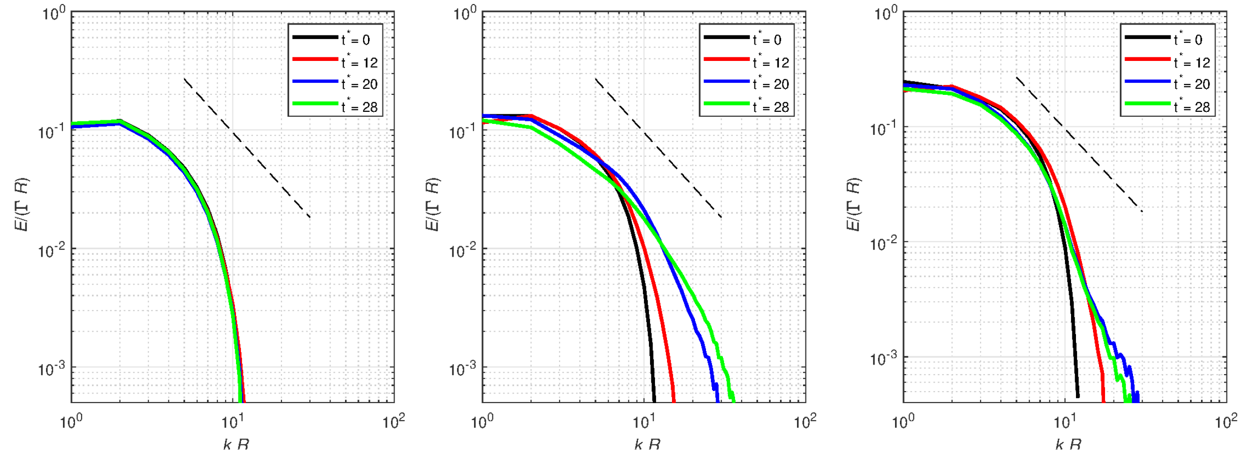

(a) (b) (c)

Figure 21: Energy spectrum of the flow induced by the interaction of a vortex ring and a vortex tube: Dashed lines represent $(-3/2)$ slope lines. (a) $Re^r_\Gamma = 10000$ & $Re^t_\Gamma = 1000$; (b) $Re^r_\Gamma = 10000$ & $Re^t_\Gamma = 5000$; (c) $Re^r_\Gamma = 10000$ & $Re^t_\Gamma = 10000$

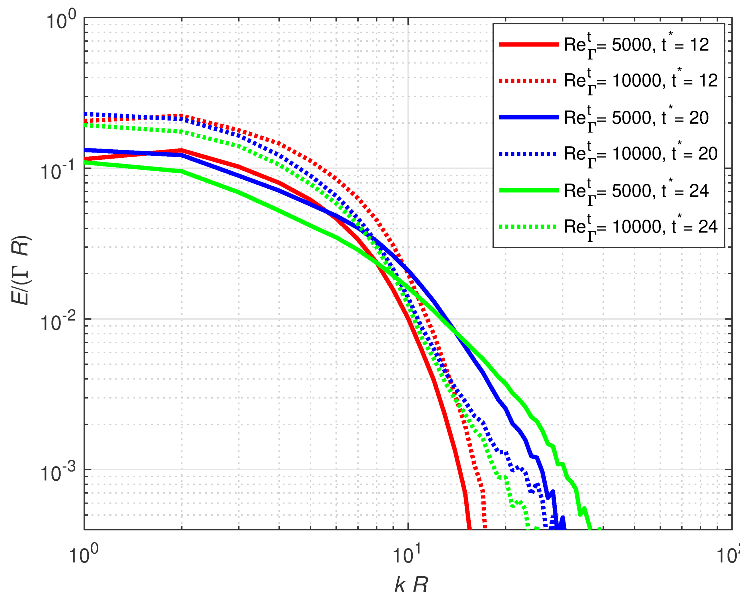

Figure 22: Comparison of the energy spectrum of the flow induced by the interaction of a vortex ring at $Re^r_\Gamma = 10000$ and a vortex tube at $Re^t_\Gamma = 5000$ and 10000

$Re^t_\Gamma = 5000$.

Figs. 23, 24 and 25 show the time evolution of the total enstrophy, kinetic energy, and the effects of the vortex diffusion, stretching, and sub-grid scale term on the rate of change of enstrophy of the flow induced by the interaction of a vortex ring and a vortex tube. In the case of $Re^r = 10000$ and $Re^t = 1000$, the total enstrophy is trivial and almost remains unchanged in the whole time evolution. This is because the tube's effects on the ring are negligible, and the flow induced by the ring dominates in the whole domain. This aspect is further explained by the fact that the effects of the vortex diffusion, stretching, and sub-grid scale term on the rate of change of enstrophy are trivial, as shown in Fig. 25. In the case of $Re^r = 10000$ and $Re^t = 5000$, the total enstrophy strongly increases from $t^* = 7.5$ to 25 due to the sum of effects of the vortex stretching and sub-grid scale term greater than those

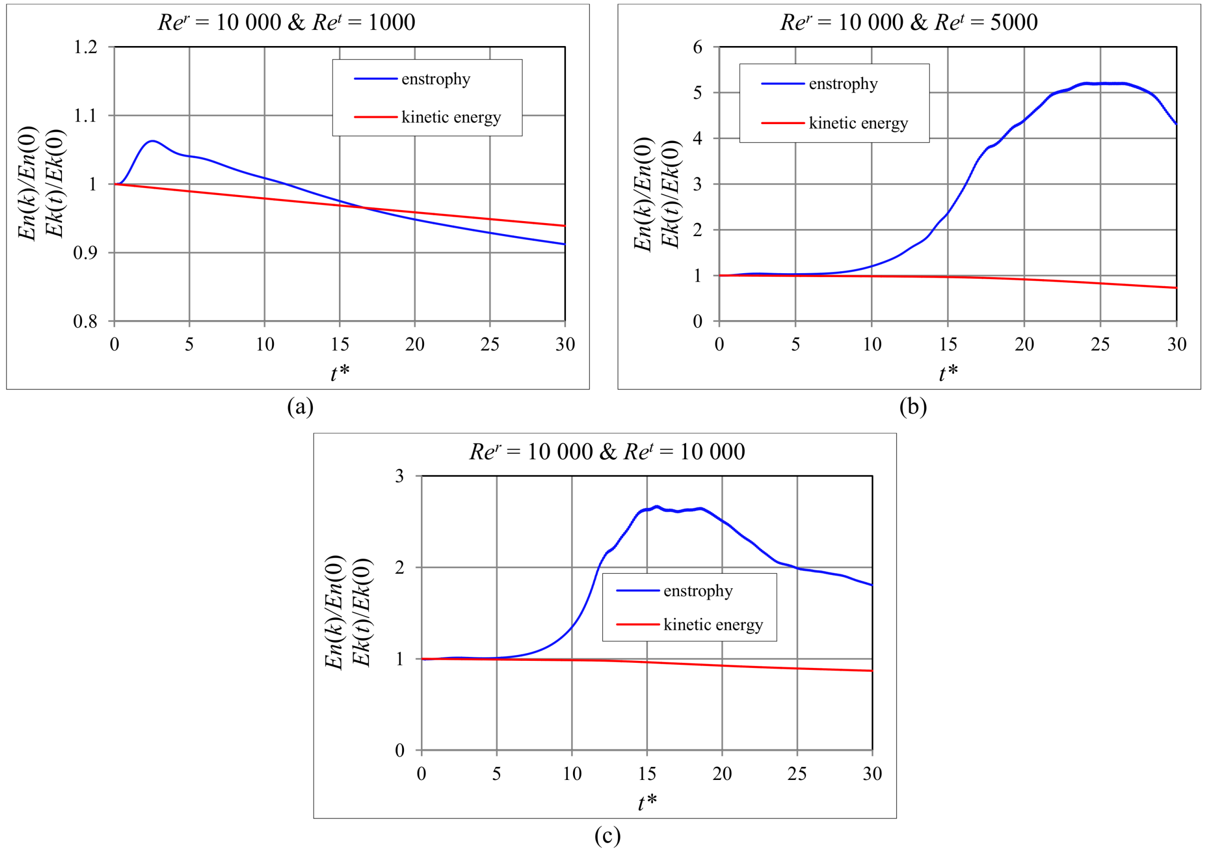

Figure 23: Time evolution of total enstrophy and kinetic energy of the flow induced by the interaction of a vortex ring and a vortex tube: (a) Re^r =10 000 & Re^t = 1000; (b) Re^r =10 000 & Re^t = 5000; (c) Re^r =10 000 & Re^t =10 000

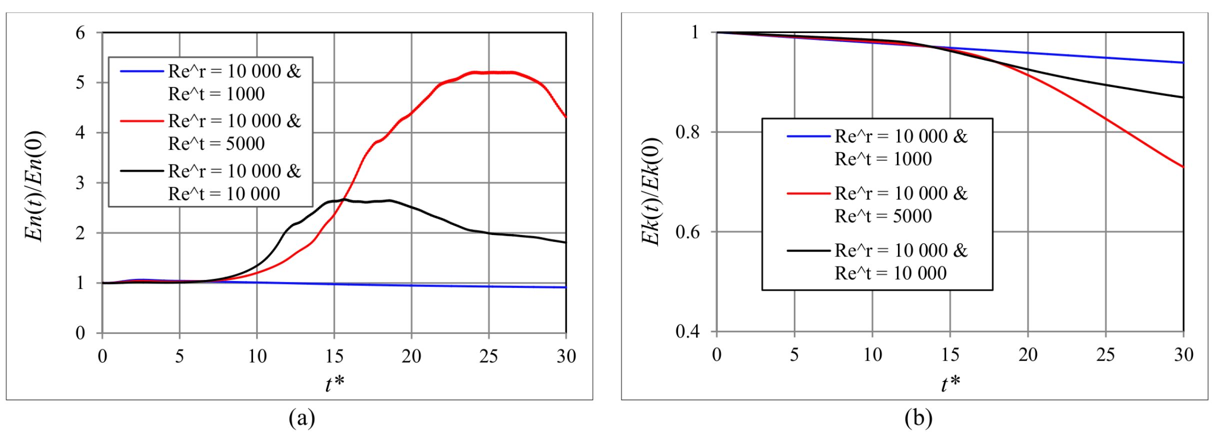

Figure 24: Time evolution of total enstrophy and kinetic energy of the flow induced by the interaction of a vortex ring and a vortex tube: (a) total enstrophy, En; (b) total kinetic energy, Ek

of vortex diffusion. In this stage, the leaving part of the tube interacts strongly with the ring to generate small-scale vortices. The enstrophy then reduces in the final stage, owing to the effects of the vortex diffusion greater than those of the vortex stretching and sub-grid scale term. The vortices forcefully decay in this stage. In the case of Re^r = 10000 and Re^t = 10000, the total enstrophy drastically increases from $t^* = 7$ to 15, due to a strong interaction between the ring and tube. During this stage, the reconnection of the vortex ring and tube occurs. The effects of vortex stretching and

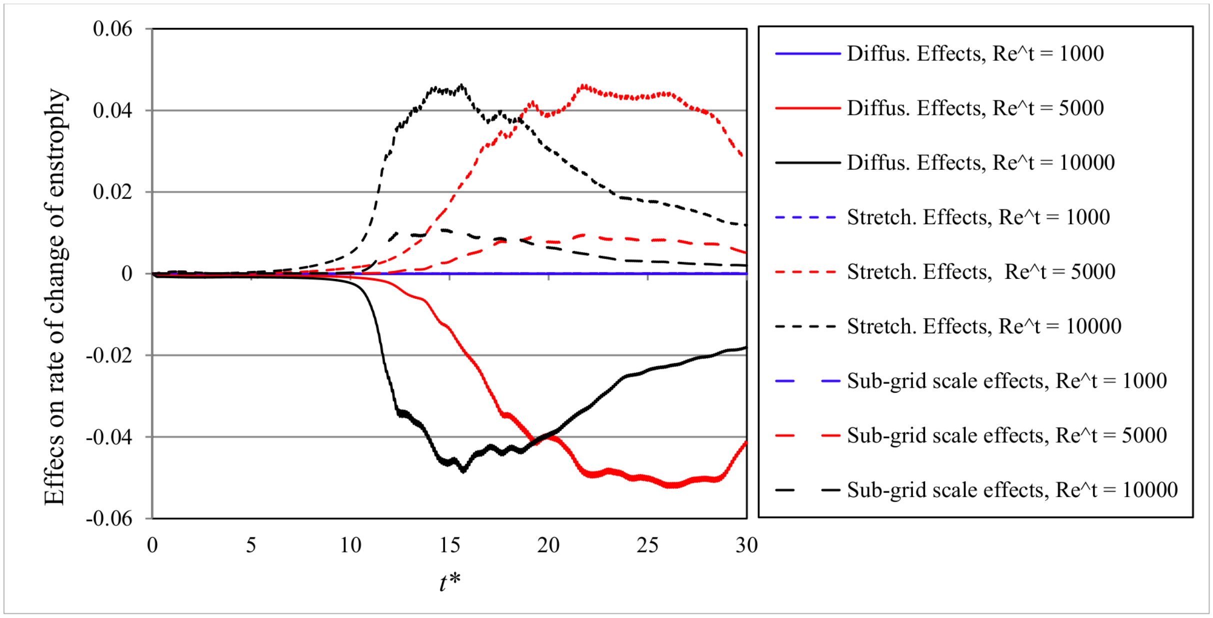

Figure 25: Time evolution of the effects of vortex diffusion, stretching and sub-grid scale term on rate of change of enstrophy of the flow induced by the interaction of a vortex ring and a vortex tube

sub-grid scale term are greater than those of the vortex diffusion, leading to a great generation of the small-scale vortex structures. The total enstrophy almost remains unchanged from $t^* = 15$ to 20, due to a balance of the generation of new small-scale vortices and decay of the existing vortices. The total enstrophy decreases in the ultimate stage due to the strong effect of vortex diffusion. From $t^* = 15$, the total enstrophy in this case are lower than those with $Re^r = 10000$ and $Re^t = 5000$. This is explained as the flow becomes more stable after the reconnection, while the flow is unstable in the case of $Re^r = 10000$ and $Re^t = 5000$ because the reconnection on the vortex ring does not happen. The total kinetic energy gradually reduces with time in three simulation cases. The most decrease is observed with $Re^r = 10000$ and $Re^t = 5000$, followed by the cases of $Re^r = 10000$ and $Re^t = 10000$ and $Re^r = 10000$ and $Re^t = 1000$. It is observed that the more the flow is unstable, the more the kinetic energy is lost due to its transfer to thermal energy.

5 Conclusions

A vortex-in-cell (VIC) method combined with a large eddy simulation (LES) model was developed for viscous incompressible flows. The vortex diffusion and stretching are calculated using the proposed 27-point and conservation schemes, respectively, which were verified using the benchmark simulations of the Taylor–Green vortex flow (TGVF) at the Reynolds number $Re = 200$. The results indicate that these schemes satisfy the convergence of a numerical method and produce the flow characteristics well. The combination of the VIC method with the LES model (LVIC) was evaluated using simulations of the TGVF at $Re = 200$ and 2000. It was proved that the LVIC could capture the characteristics of the turbulent flows well. Moreover, a Lagrangian method for passive scalar transport intensified with the LVIC was developed to track the vortex dynamics. The LVIC was then applied to simulations of the interaction of a vortex ring and a vortex tube to clarify their reconnection characteristics. The characteristics of the flow phenomena are highlighted as follows:

In the case of $Re_\Gamma^r = 10000$ and $Re_\Gamma^t = 1000$, the tube effects on the ring are trivial while the ring breaks it into two parts and entrains them. The energy spectrum remains unchanged with time evolution, the small-scale vortex structure is not generated, and the helicity does not appear on the vortex structure.

In the case of $Re_\Gamma^r = 10000$ and $Re_\Gamma^t = 5000$, a part of the tube is detached, and this part rolls around the ring to generate the vortex structures of small scales. The tube is reconnected after the impingement. The population of small-scale vortex structures increases in the whole time evolution; the smaller-scale vortices continue to be formed after the impingement. The detached part of the tube and the ring are strongly twisted.

In the case of $Re_\Gamma^r = 10000$ and $Re_\Gamma^t = 10000$, the reconnection occurs on both the ring and tube. When the ring collides with the tube, they break into two parts. A part of the ring connects with a leaving part of the tube to form the secondary ring while the rest replaces the leaving part to reconstruct the tube. Then, the flow becomes more stable. The population of the small-scale vortex structures increases from the beginning until the collision. However, it significantly decreases after the reconnection.

The total enstrophy in the case of $Re_\Gamma^r = 10000$ and $Re_\Gamma^t = 1000$ is trivial and remains unchanged with time evolution because of a weak vortex interaction. The duration of the increase of the enstrophy in the case of $Re_\Gamma^r = 10000$ and $Re_\Gamma^t = 5000$ is longer than those with $Re_\Gamma^r = 10000$ and $Re_\Gamma^t = 10000$. This is explained as the fact that with $Re_\Gamma^r = 10000$ and $Re_\Gamma^t = 10000$, the flow becomes more stable when the ring and tube are reconnected. The reconnection reduces the mixing performance. The total kinetic energy significantly reduces in the case of $Re_\Gamma^r = 10000$ and $Re_\Gamma^t = 5000$, followed by the cases with $Re_\Gamma^t = 10000$ and $Re_\Gamma^t = 1000$, respectively. The higher the mixing performance is, the more significant the kinetic energy is transferred to thermal energy.

A Change rate of enstrophy

The flow enstrophy is formulated as

$$En(t) = \frac{1}{2L_xL_yL_z}\iiint_{\mathbf{\Omega}} \overline{\boldsymbol{\omega}}^2 dxdydz \tag{43}$$

The change rate of enstrophy is expressed as [24]

$$\frac{D(En(t))}{Dt} = \frac{1}{L_xL_yL_z}\iiint_{\mathbf{\Omega}} \frac{D(0.5\overline{\boldsymbol{\omega}}^2)}{Dt} dxdydz = \frac{1}{L_xL_yL_z}\iiint_{\mathbf{\Omega}} \frac{\overline{\boldsymbol{\omega}}D\overline{\boldsymbol{\omega}}}{Dt} dxdydz \tag{44}$$

Substituting the following equation, Eq. 24,

$$\frac{D\overline{\boldsymbol{\omega}}}{Dt} = \frac{\partial\overline{\boldsymbol{\omega}}}{\partial t} + (\overline{\boldsymbol{u}}\cdot\nabla)\overline{\boldsymbol{\omega}} = \nu\nabla^2\overline{\boldsymbol{\omega}} + (\overline{\boldsymbol{\omega}}\cdot\nabla)\overline{\boldsymbol{u}} + \nabla\cdot(\Phi_{ij} - \Phi_{ji}) \tag{45}$$

into Eq. (44), an equation showing the effects on the change rate of enstrophy is written as

$$\begin{aligned}\frac{D(En(t))}{Dt} = &\underbrace{\frac{1}{L_xL_yL_z}\iiint_{\mathbf{\Omega}} \overline{\boldsymbol{\omega}}\cdot(\nu\nabla^2\overline{\boldsymbol{\omega}})dxdydz}_{\text{diffusion effects}} + \underbrace{\frac{1}{L_xL_yL_z}\iiint_{\mathbf{\Omega}} \overline{\boldsymbol{\omega}}\cdot\left[(\overline{\boldsymbol{\omega}}\cdot\nabla)\overline{\boldsymbol{u}}\right]dxdydz}_{\text{stretching effects}} + \\ &\underbrace{\frac{1}{L_xL_yL_z}\iiint_{\mathbf{\Omega}} \overline{\boldsymbol{\omega}}\cdot\left[\nabla\cdot(\Phi_{ij} - \Phi_{ji})\right]dxdydz}_{\text{sub-grid scale effects}}\end{aligned} \tag{46}$$

The first, second, and third terms on the right of Eq. (46) expresses the effects of vortex diffusion, stretching, and sub-grid scale term on the rate of change of enstrophy.

Declaration of interest

The authors declare no competing financial interest.

DATA AVAILABILITY

The data that support the findings of this study are available from the corresponding author upon reasonable request.

References

[1] T. T. Lim and T. B. Nickels, "Instability and reconnection in the head-on collision of two vortex rings," *Nature*, vol. 357, pp. 225–227, 1992.

[2] M. W. Scheeler, W. M. van Rees, H. Kedia, D. Kleckner, and W. T. M. Irvine, "Complete measurement of helicity and its dynamics in vortex tubes," *Science*, vol. 357, pp. 487–491, 2017.

[3] G. Winckelmens, R. Cocle, L. Dufresne, and R. Capart, "Vortex methods and their application to trailing vortex simulations," *Comptes Rendus Physique*, vol. 6, no. 4–5, pp. 467–486, 2005.

[4] H. Ishikawa, S. Izawa, O. Mochizuki, and M. Kiya, "Vortex ring-vortex tube interactions," *Transactions of the Japan Society of Mechanical Engineers, Part B*, vol. 68, no. 674, pp. 2688–2694, 2002.

[5] S. Sazhin, F. Kaplanski, S. Begg, and M. Heikal, "Vortex rings in internal combustion engines: modelling versus experiment," *Proceedings of the 19th International Symposium on Transport Phenomena*, p. 7 pages, 2008.

[6] P. Walmsley, P. Tompsett, D. Zmeev, and A. Golov, "Reconnections of quantized vortex rings in superfluid ^{4}He at very low temperatures," *Phys. Rev. Lett.*, vol. 113, p. 125302, 2014.

[7] R. S. Jaque and O. V. Fuentes, "Reconnection of orthogonal cylindrical vortices," *European Journal of Mechanics - B/Fluids*, vol. 62, pp. 51–56, 2017.

[8] W. V. Rees, M. Wim, F. Hussain, and P. Koumoutsakos, "Vortex tube reconnection at $re = 10^4$," *Physics of fluids*, vol. 24, no. 7, p. 075105, 2012.

[9] F. Hussain and K. Duraisamy, "Mechanics of viscous vortex reconnection," *Physics of Fluids*, vol. 23, no. 2, p. 021701, 2011.

[10] G. Beardsell, L. Dufresne, and G. Dumas, "Investigation of the viscous reconnection phenomenon of two vortex tubes through spectral simulations," *Physics of Fluids*, vol. 28, no. 9, p. 095103, 2016.

[11] P. McGavin and D. I. Pontin, "Reconnection of vortex tubes with axial flow," *Physical Review Fluids*, vol. 4, no. 2, p. 024701, 2019.

[12] M. Cheng, J. Lou, and T. T. Lim, "Leapfrogging of multiple coaxial viscous vortex rings," *Physics of Fluids*, vol. 27, p. 031702, 2015.

[13] M. Cheng, J. Lou, and T. T. Lim, "Evolution of an elliptic vortex ring in a viscous fluid," *Physics of Fluids*, vol. 28, no. 3, p. 037104, 2016.

[14] J. Yao and F. Hussain, "A physical model of turbulence cascade via vortex reconnection sequence and avalanche," *Journal of Fluid Mechanics*, vol. 883, 2020.

[15] C.-C. Chu, C.-T. Wang, C.-C. Chang, R.-Y. Chang, and W.-T. Chang, "Head-on collision of two coaxial vortex rings: experiment and computation," *J. Fluid Mech.*, vol. 296, pp. 39–71, 1995.

[16] M. Cheng, J. Lou, and T. T. Lim, "Numerical simulation of head-on collision of two coaxial vortex rings," *Fluid Dynamics Research*, vol. 50, no. 6, p. 065513, 2018.

[17] M. Cheng, , J. Lou, and T. T. Lim, "Collision and reconnection of viscous elliptic vortex rings," *Physics of Fluids*, vol. 31, no. 6, p. 067107, 2019.

[18] P. Chatelain, D. Kivotides, and A. Leonard, "Reconnection of colliding vortex rings," *Physical review letters*, vol. 90, no. 5, p. 054501, 2003.

[19] R. McKeown, P. R. Ostilla-Mónico, A. Pumir, M. P. Brenner, and S. M. Rubinstein, "Turbulence generation through an iterative cascade of the elliptical instability," *Science Advances*, vol. 6, no. 9, p. eaaz2717, 2020.

[20] Y. Kato, Y. Tada, H. Harada, Y. Nagatsu, and T. Nakatani, "Effects of vortex ring on liquid mixing," *KAGAKU KOGAKU RONBUNSHU*, vol. 34, no. 6, pp. 562–565, 2008.

[21] I. Zawadzki and H. Aref, "Mixing during vortex ring collision," *Phys. Fluids A*, vol. 3, no. 5, pp. 1405–1410, 1991.

[22] R. H. Hernandez and T. Reyes, "Symmetrical collision of multiple vortex rings," *Physics of Fluids*, vol. 29, no. 10, p. 103604, 2017.

[23] G.-H. Cottet and P. Poncet, "Advances in direct numerical simulations of 3D wall-bounded flows by vortex-in-cell methods," *J. Comput. Phys.*, vol. 193, no. 1, pp. 136–158, 2003.

[24] V. L. Nguyen, K. Takamure, and T. Uchiyama, "Deformation of a vortex ring caused by its impingement on a sphere," *Physics of Fluids*, vol. 31, no. 10, p. 107108, 2019.

[25] V. L. Nguyen, T. Degawa, T. Uchiyama, and K. Takamure, "Numerical simulation of bubbly flow around a cylinder by semi-Lagrangian–Lagrangian method," *Int. J. Numerical Methods for Heat and Fluid Flow*, vol. 29, no. 12, pp. 4660–4683, 2019.

[26] L. A. Barba, A. Leonard, and C. B. Allen, "Numerical investigations of the accuracy of the vortex method with and without remeshing," *16th AIAA Computational Fluid Dynamics Conference, Floria*, p. 11 pages, 2003.

[27] V. L. Nguyen, T. Degawa, and T. Uchiyama, "Numerical simulation of annular bubble plume by vortex in cell method," *Int. J. Numerical Methods for Heat and Fluid Flow*, vol. 29, no. 3, pp. 1103–1131, 2019.

[28] C. K. Birdsall and D. Fuss, "Clouds-in-clouds, clouds-in-cells physics for many-body plasma simulation," *J. Comput. Phys.*, vol. 3, no. 4, pp. 494–511, 1969.

[29] J. P. Christiansen, "Numerical simulation of hydrodynamics by the method of point vortices," *J. Comput. Phys.*, vol. 13, no. 3, pp. 363–379, 1973.

[30] G.-H. Cottet and P. D. Koumoutsakos, *Vortex Methods: Theory and Practice.* Cambridge University Press, 2000.

[31] M. Coquerelle and G.-H.Cottet, "A vortex level set method for the two-way coupling of an incompressible fluid with colliding rigid bodies," *J. Comput. Phys.*, vol. 227, no. 21, pp. 9121–9137, 2008.

[32] J. H. Walther and P. Koumoutsakos, "Three-dimensional vortex methods for particle-laden flows with two-way coupling," *J. Comput. Phys.*, vol. 167, no. 1, pp. 39–71, 2001.

[33] V. L. Nguyen, T. Degawa, and T. Uchiyama, "Numerical simulation of the interaction between a vortex ring and a bubble plume," *Int. J. Numerical Methods for Heat and Fluid Flow*, vol. 29, no. 9, pp. 3192–3224, 2019.

[34] A. J. Chorin, "Numerical study of slightly viscous flow," *J. Fluid Mech.*, vol. 57, no. 4, pp. 785–796, 1973.

[35] A. Leonard, "Vortex methods for flow simulation," *J. Comp. Phys.*, vol. 37, pp. 289–335, 1980.

[36] L. F. Rossi, "Resurrecting core spreading vortex methods: A new scheme that is both deterministic and convergent," *SIAM J. Sci. Comp..*, vol. 17, pp. 370–397, 1996.

[37] D. Fishelov, "A new vortex scheme for viscous flows," *J. Comput. Physics*, vol. 86, pp. 211–224, 1990.

[38] Y. Ogami and T. Akamatsu, "Viscous flow simulation using the discrete vortex model – The diffusion velocity method," *Computers and Fluids*, vol. 19, pp. 433–441, 1991.

[39] S. Shankar and L. van Dommelen, "A new diffusion procedure for vortex methods," *J. Comp. Phys.*, vol. 127, pp. 88–109, 1996.

[40] P. Degond and S. Mas-Gallic, "The weighted particle method for convection–diffusion equations. I. The case of an isotropic viscosity; II. The anisotropic case," *Math. Comput.*, vol. 53, no. 188, pp. 529–525, 1989.

[41] G.-H. Cottet, "Large-time behavior of deterministic particle approximations to the navier-stokes equations," *Mathematics of Computation*, vol. 56, no. 193, pp. 45–59, 1991.

[42] J. R. Mansfield, O. M. Knio, and C. Meneveau, "A dynamic LES scheme for the vorticity transport equation: Formulation and a priori tests," *J. Comput. Phys.*, vol. 145, no. 2, pp. 693–730, 1998.

[43] P. Chatelain, S. Backaert, G. Winckelmans, and S. Kern, "Large eddy simulation of wind turbine wakes. Flow, turbulence and combustion," *Flow, turbulence and combustion*, vol. 91, no. 3, pp. 587–605, 2013.

[44] R. Cocle, L. Bricteuxa, and G. Winckelmans, "Scale dependence and asymptotic very high Reynolds number spectral behavior of multiscale subgrid models," *Physics of Fluids*, vol. 21, no. 8, p. 085101, 2009.

[45] J. R. Mansfield, O. M. Knio, and C. Meneveau, "Dynamic LES of colliding vortex rings using a 3D vortex method," *J. Comput. Phys.*, vol. 197, no. 2, pp. 779–780, 2004.

[46] J. J. Monaghan, "Extrapolating B splines for interpolation," *J. Comput. Phys.*, vol. 60, no. 2, pp. 253–262, 1985.

[47] G. Winckelmens and A. Leonard, "Contributions to vortex particle methods for the computation of three-dimensional incompressible unsteady flows," *J. of Comput. Physics*, vol. 109, no. 2, pp. 247–273, 1993.

[48] M. Frigo and S. G. Johnson, "http://www.fftw.org/," 1997.

[49] N. Sharma and T. K. Sengupta, "Vorticity dynamics of the three-dimensional taylor-green vortex problem," *Phys. Fluids*, vol. 31, no. 3, p. 035106, 2019.

[50] S. A. Orszag, "Numerical simulation of the Taylor-Green vortex," *Computing Methods in Applied Sciences and Engineering Part 2: International Symposium, Versailles*, pp. 50–64, 1974.

[51] R. Z. Lavi, V. D. Duong, J. S. Alex, and M. Day, "Core spreading vortex method for simulating 3d flows around bluff bodies," *Journal of Engineering and Technological Sciences*, vol. 46, no. 4, pp. 436–454, 2014.

[52] R. J. Leveque, "High-resolution conservative algorithms for advection in incompressible flow," *SIAM Journal on Numerical Analysis*, vol. 33, no. 2, pp. 627–665, 1996.

[53] I. S. Sullivan, J. J. Niemela, R. E. Hershberger, D. Bolster, and R. J. Donnelly, "Dynamics of thin vortex rings," *Journal of Fluid Mechanics*, vol. 609, pp. 319–347, 2008.

[54] J. C. R. Hunt, A. A. Wray, and P. Moin, "Eddies, stream, and convergence zones in turbulent flows," *Center for Turbulence Research Report CTR-S88*, pp. 193–208, 1988.

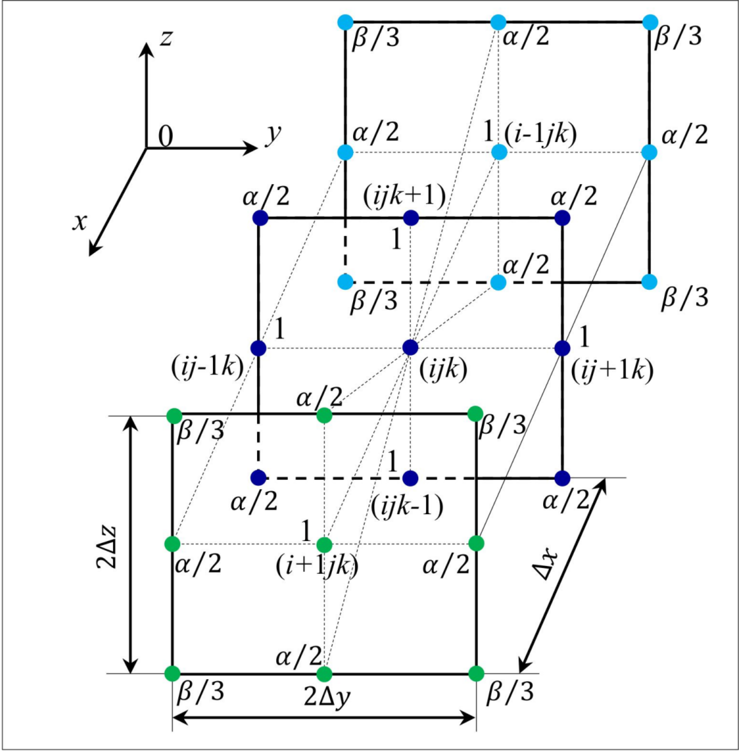

z
0
y
x
β/3
α/2
β/3
α/2
1 (i-1jk)
α/2
α/2
(ijk+1)
α/2
1
α/2
β/3
β/3
1
1
(ij-1k)
(ijk)
(ij+1k)
α/2
β/3
β/3
1
α/2
(ijk-1)
α/2
2Δz
1
α/2
(i+1jk)
α/2
Δx
α/2
β/3
2Δy
β/3

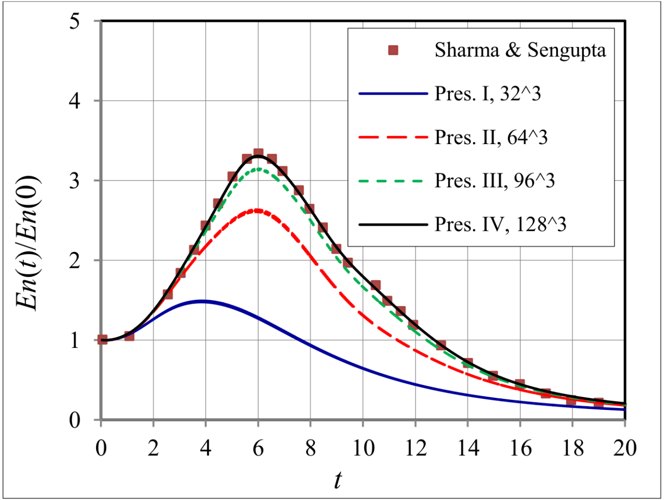

Sharma & Sengupta
Pres. I, 32^3
Pres. II, 64^3
Pres. III, 96^3
Pres. IV, 128^3
$En(t)/En(0)$
t

(a)

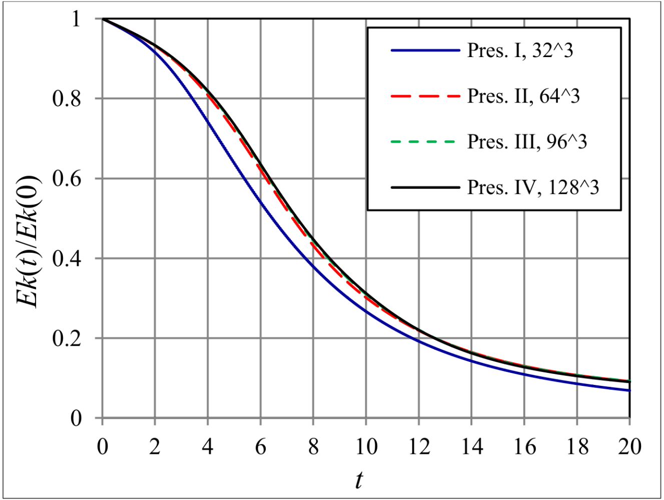

Pres. I, 32^3
Pres. II, 64^3
Pres. III, 96^3
Pres. IV, 128^3
$Ek(t)/Ek(0)$
t

(b)

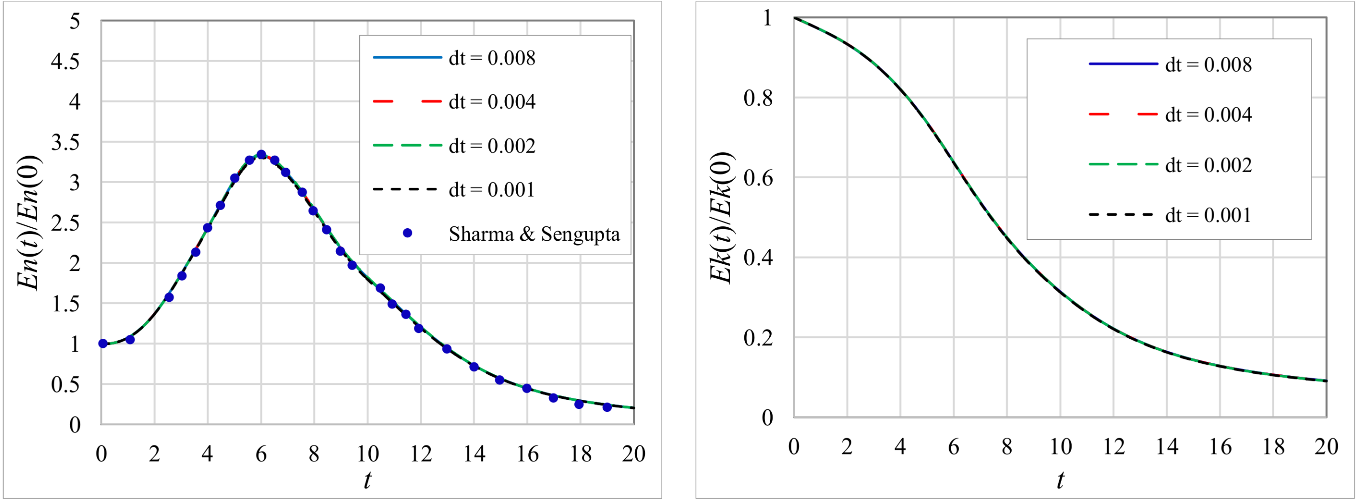
En(t)/En(0)
t
dt = 0.008
dt = 0.004
dt = 0.002
dt = 0.001
Sharma & Sengupta
Ek(t)/Ek(0)
t
dt = 0.008
dt = 0.004
dt = 0.002
dt = 0.001

(a) (b)

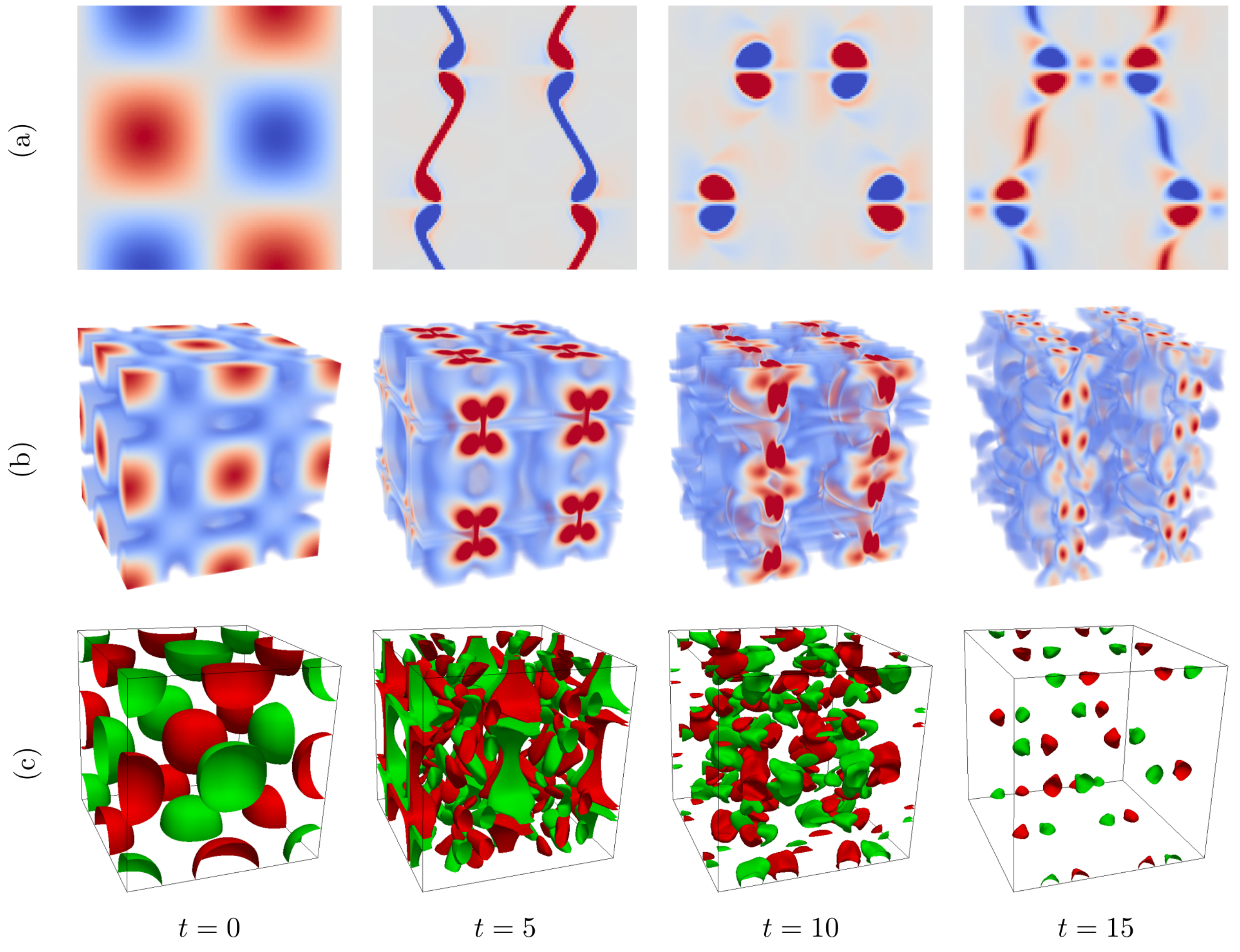

(a)
(b)
(c)
$t = 0$
$t = 5$
$t = 10$
$t = 15$

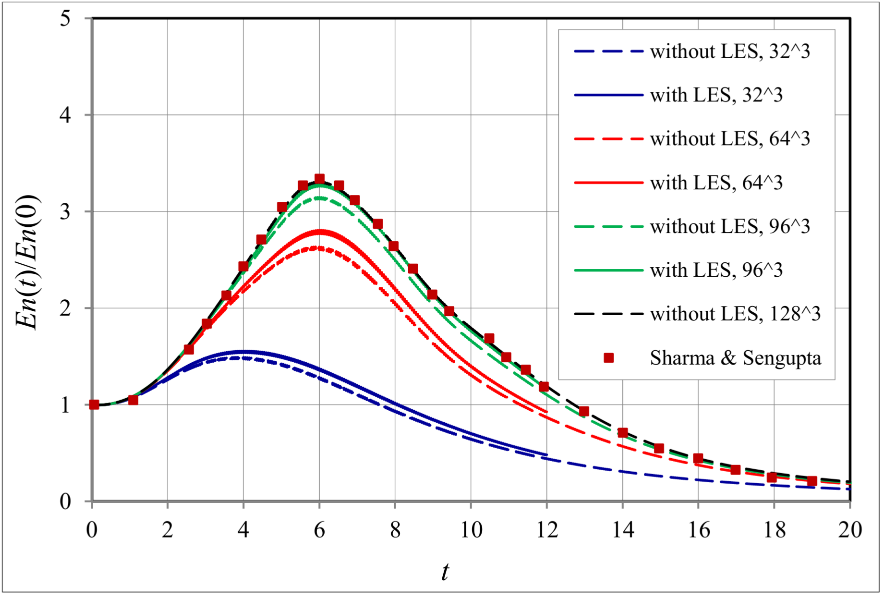

without LES, 32^3
with LES, 32^3
without LES, 64^3
with LES, 64^3
without LES, 96^3
with LES, 96^3
without LES, 128^3
Sharma & Sengupta
$En(t)/En(0)$
t
0
1
2
3
4
5
0
2
4
6
8
10
12
14
16
18
20

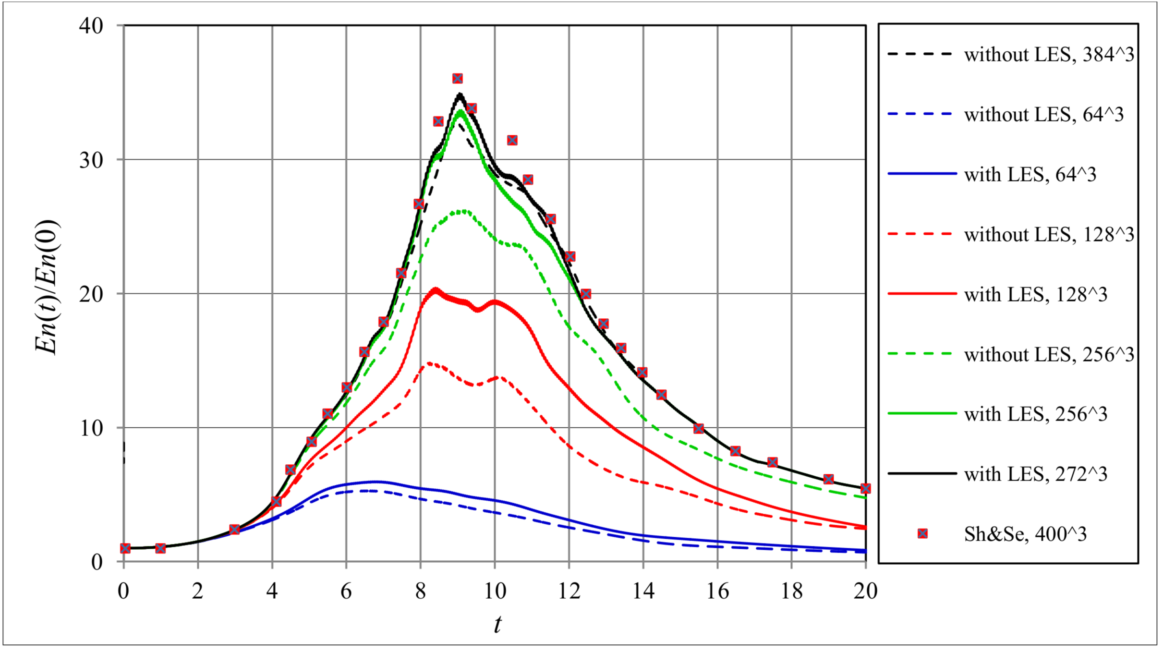

En(t)/En(0)
t
0
10
20
30
40
0
2
4
6
8
10
12
14
16
18
20
without LES, 384^3
without LES, 64^3
with LES, 64^3
without LES, 128^3
with LES, 128^3
without LES, 256^3
with LES, 256^3
with LES, 272^3
Sh&Se, 400^3

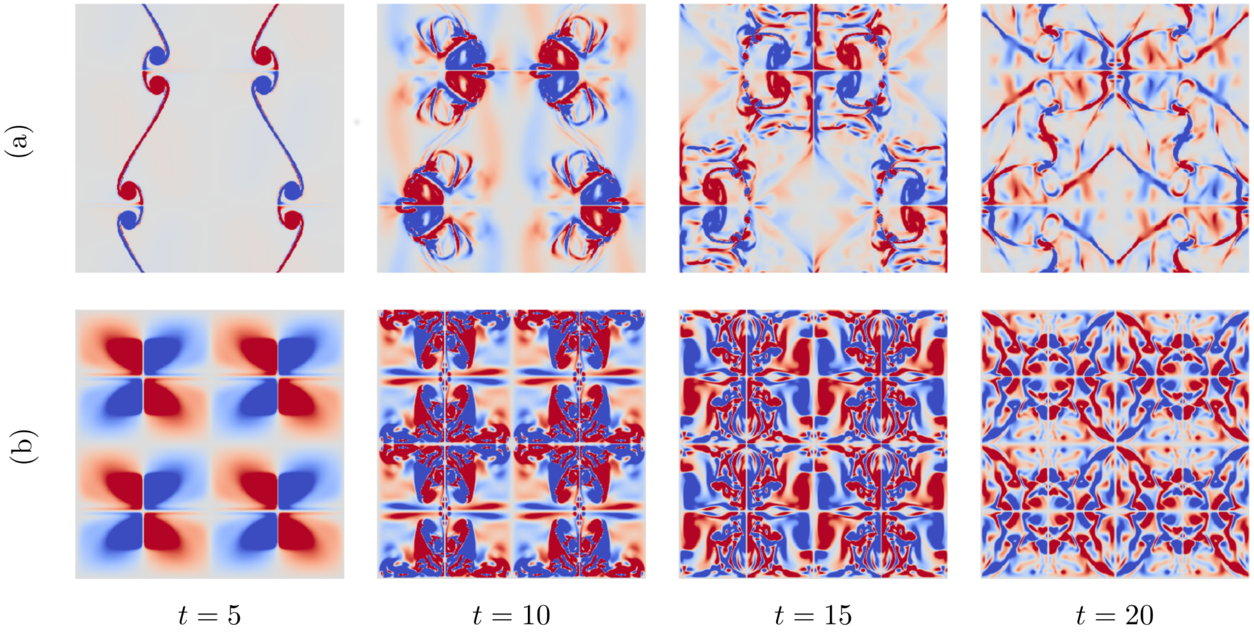
(a)
(b)
$t = 5$
$t = 10$
$t = 15$
$t = 20$

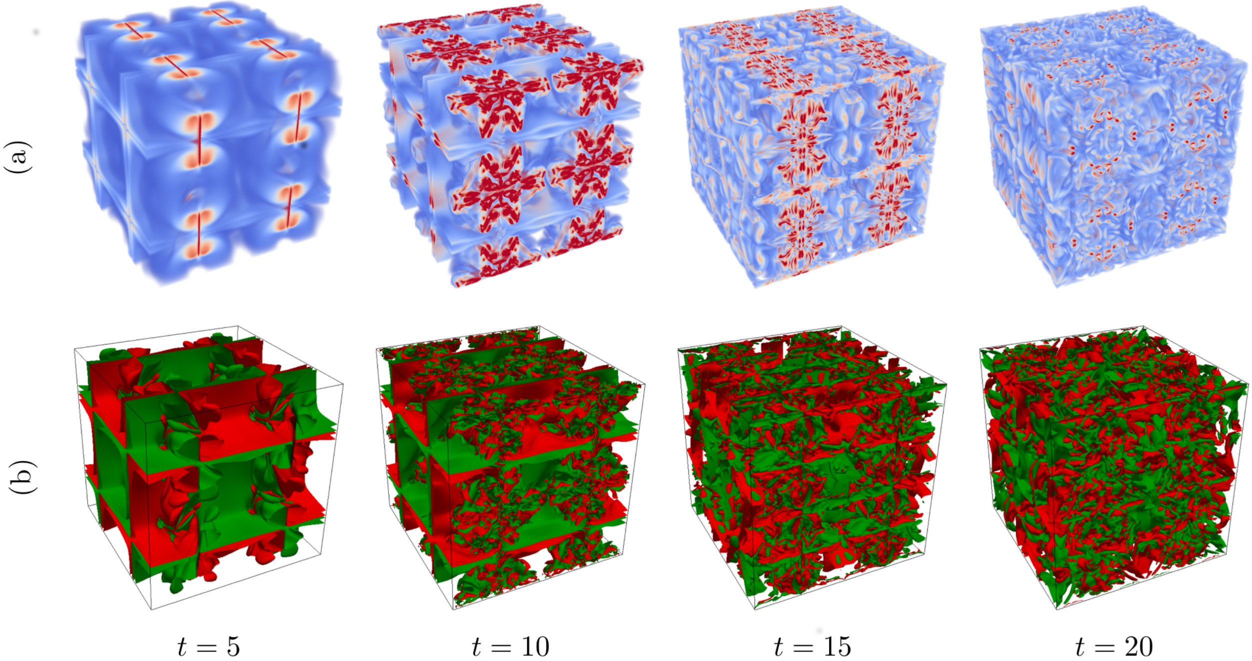
(a)
(b)
$t = 5$
$t = 10$
$t = 15$
$t = 20$

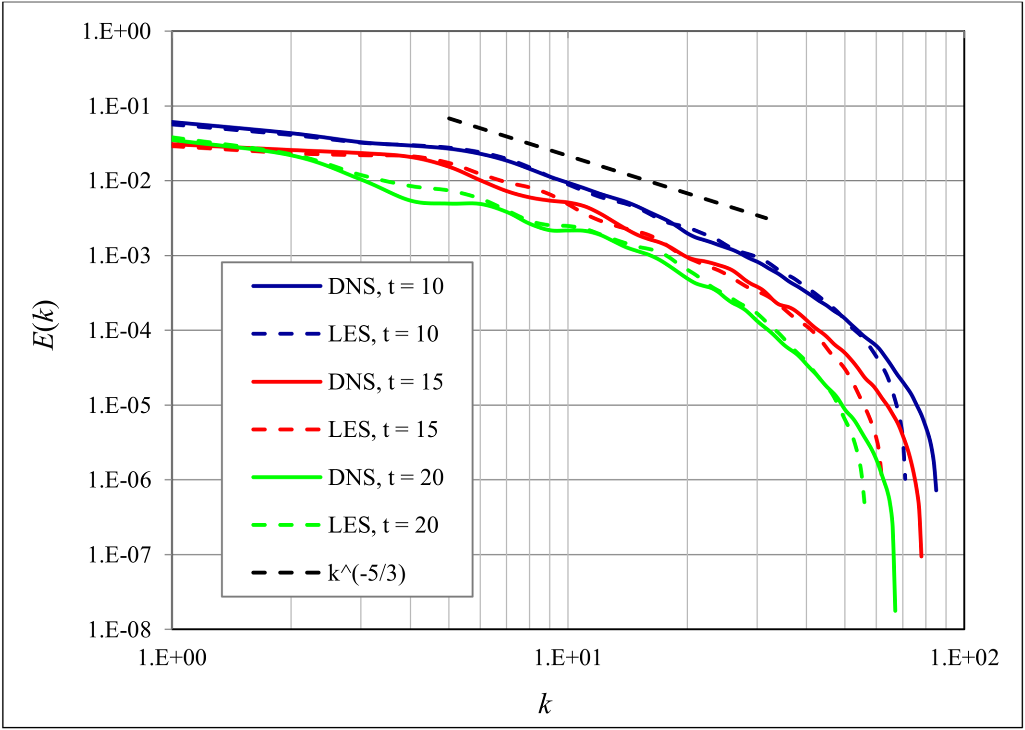

1.E+00
1.E-01
1.E-02
1.E-03
1.E-04
1.E-05
1.E-06
1.E-07
1.E-08
E(k)
1.E+00
1.E+01
1.E+02
k
DNS, t = 10
LES, t = 10
DNS, t = 15
LES, t = 15
DNS, t = 20
LES, t = 20
k^(-5/3)

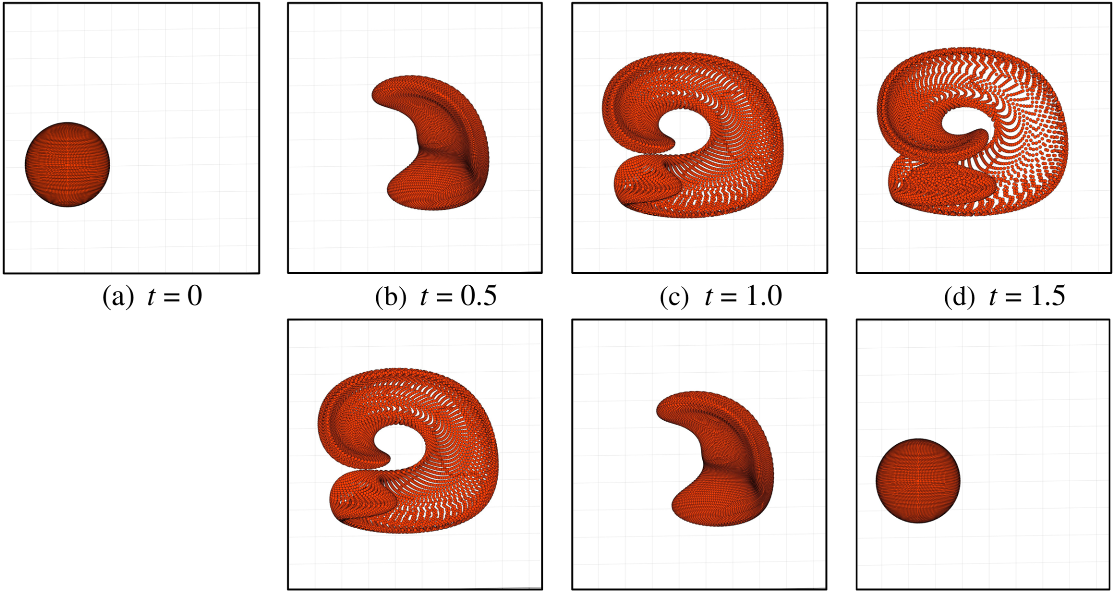

(a) $t = 0$ (b) $t = 0.5$ (c) $t = 1.0$ (d) $t = 1.5$

(e) $t = 2.0$ (f) $t = 2.5$ (g) $t = 3.0$

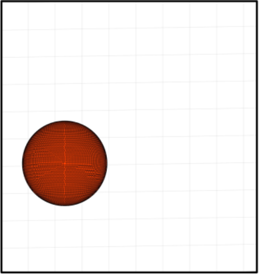

(a) $t = 0$

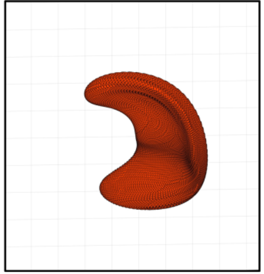

(b) $t = 0.5$

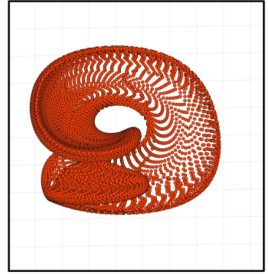

(c) $t = 1.0$

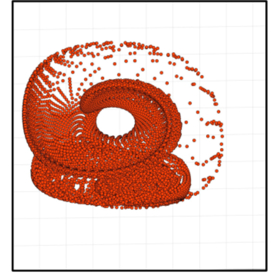

(d) $t = 1.5$

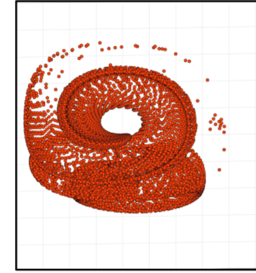

(e) $t = 2.0$

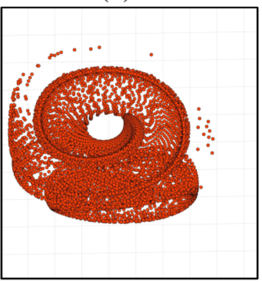

(f) $t = 2.5$

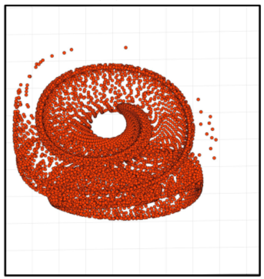

(g) $t = 3.0$

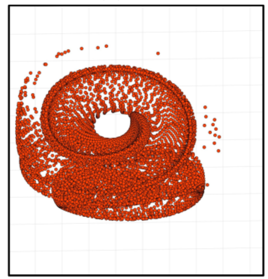

(h) $t = 3.5$

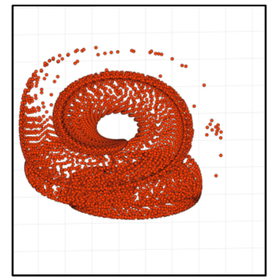

(i) $t = 4.0$

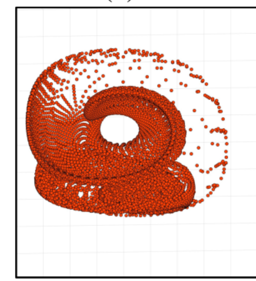

(j) $t = 4.5$

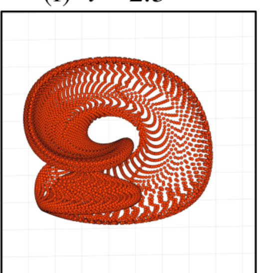

(k) $t = 5.0$

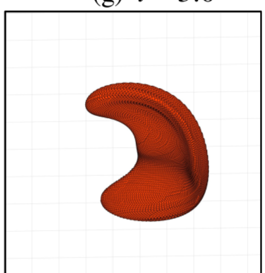

(l) $t = 5.5$

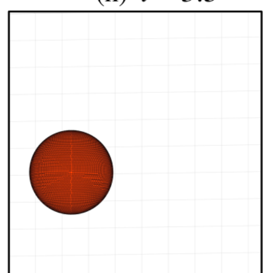

(m) $t = 6.0$

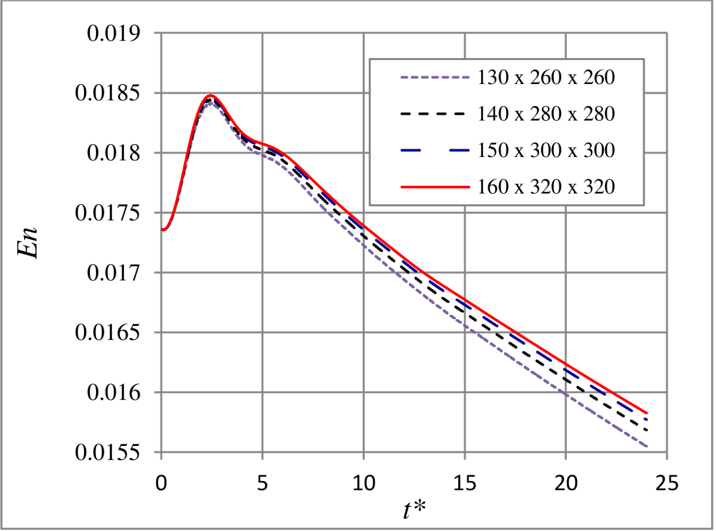
0.019
0.0185
0.018
0.0175
0.017
0.0165
0.016
0.0155
En
0
5
10
15
20
25
t*
130 x 260 x 260
140 x 280 x 280
150 x 300 x 300
160 x 320 x 320

(a)

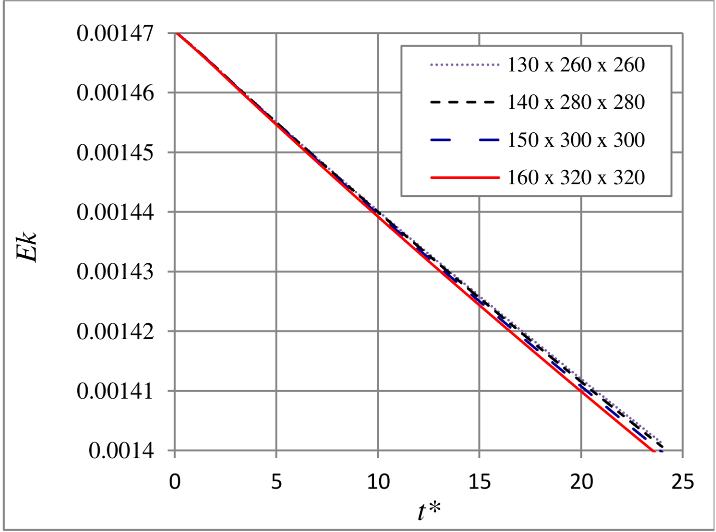
0.00147
0.00146
0.00145
0.00144
0.00143
0.00142
0.00141
0.0014
Ek
0
5
10
15
20
25
t*
130 x 260 x 260
140 x 280 x 280
150 x 300 x 300
160 x 320 x 320

(b)

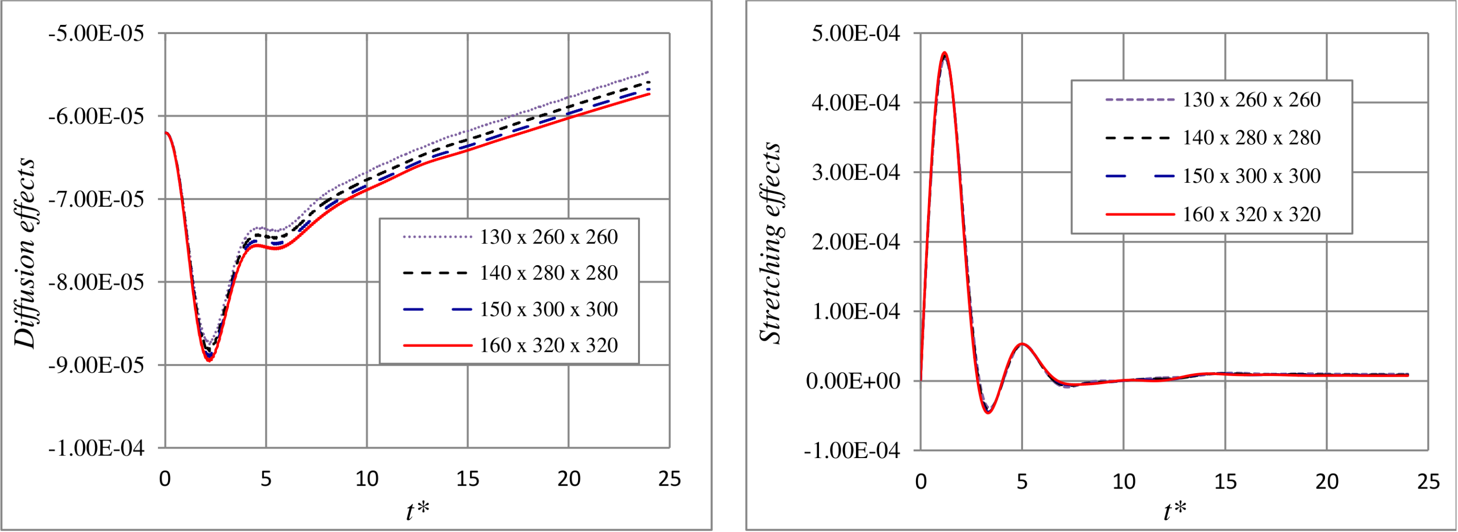

-5.00E-05
-6.00E-05
-7.00E-05
-8.00E-05
-9.00E-05
-1.00E-04
Diffusion effects
0
5
10
15
20
25
t*
130 x 260 x 260
140 x 280 x 280
150 x 300 x 300
160 x 320 x 320
5.00E-04
4.00E-04
3.00E-04
2.00E-04
1.00E-04
0.00E+00
-1.00E-04
Stretching effects

(a) (b)

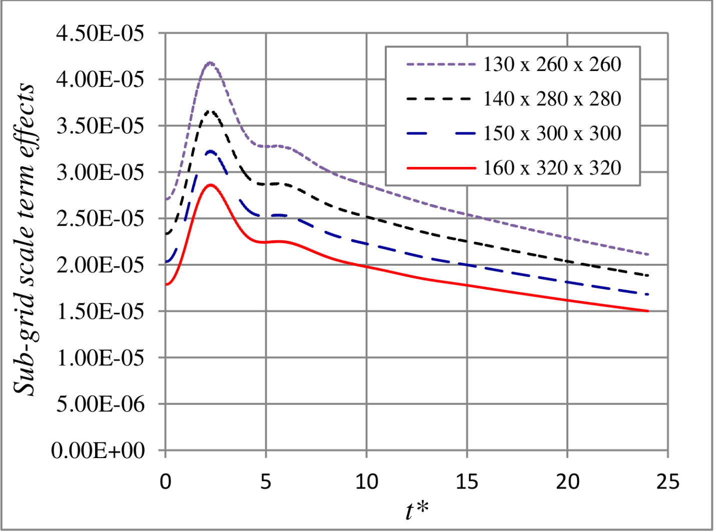

Sub-grid scale term effects
t*
130 x 260 x 260
140 x 280 x 280
150 x 300 x 300
160 x 320 x 320

(a)

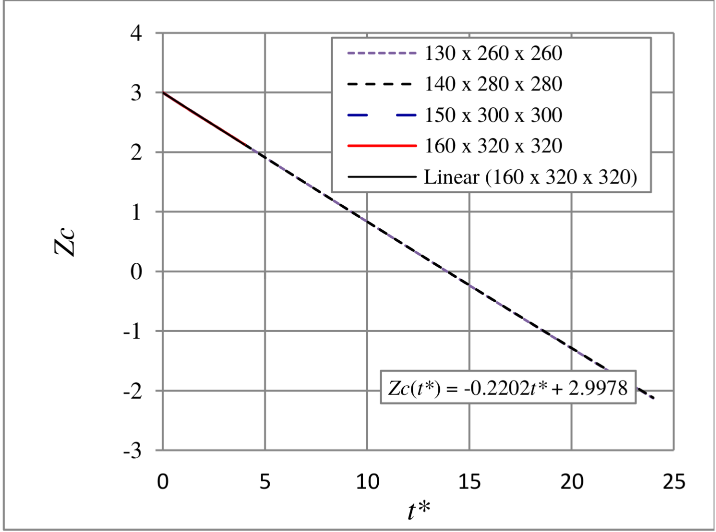

Zc
t*
130 x 260 x 260
140 x 280 x 280
150 x 300 x 300
160 x 320 x 320
Linear (160 x 320 x 320)
Zc(t*) = -0.2202t* + 2.9978

(b)

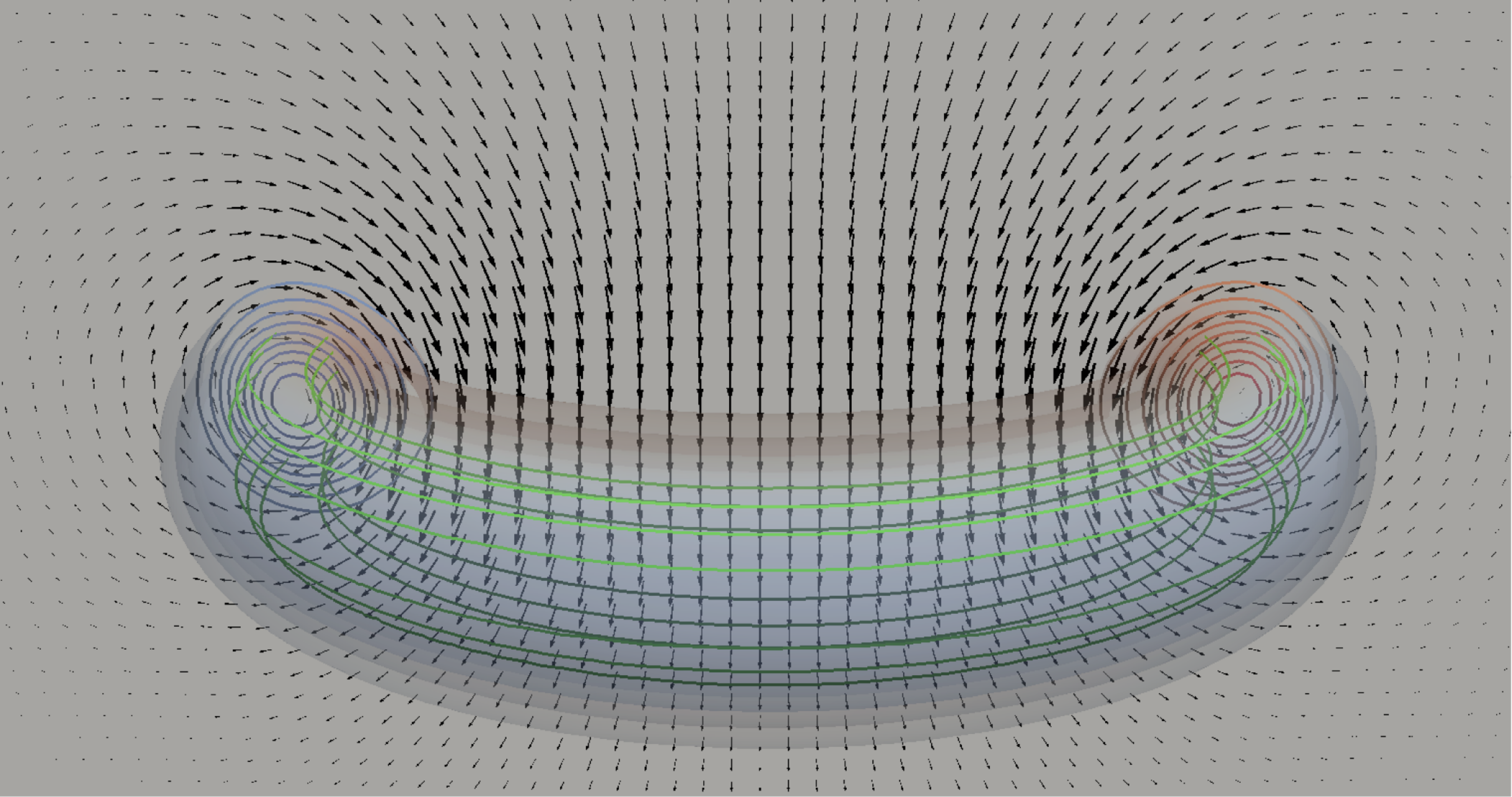

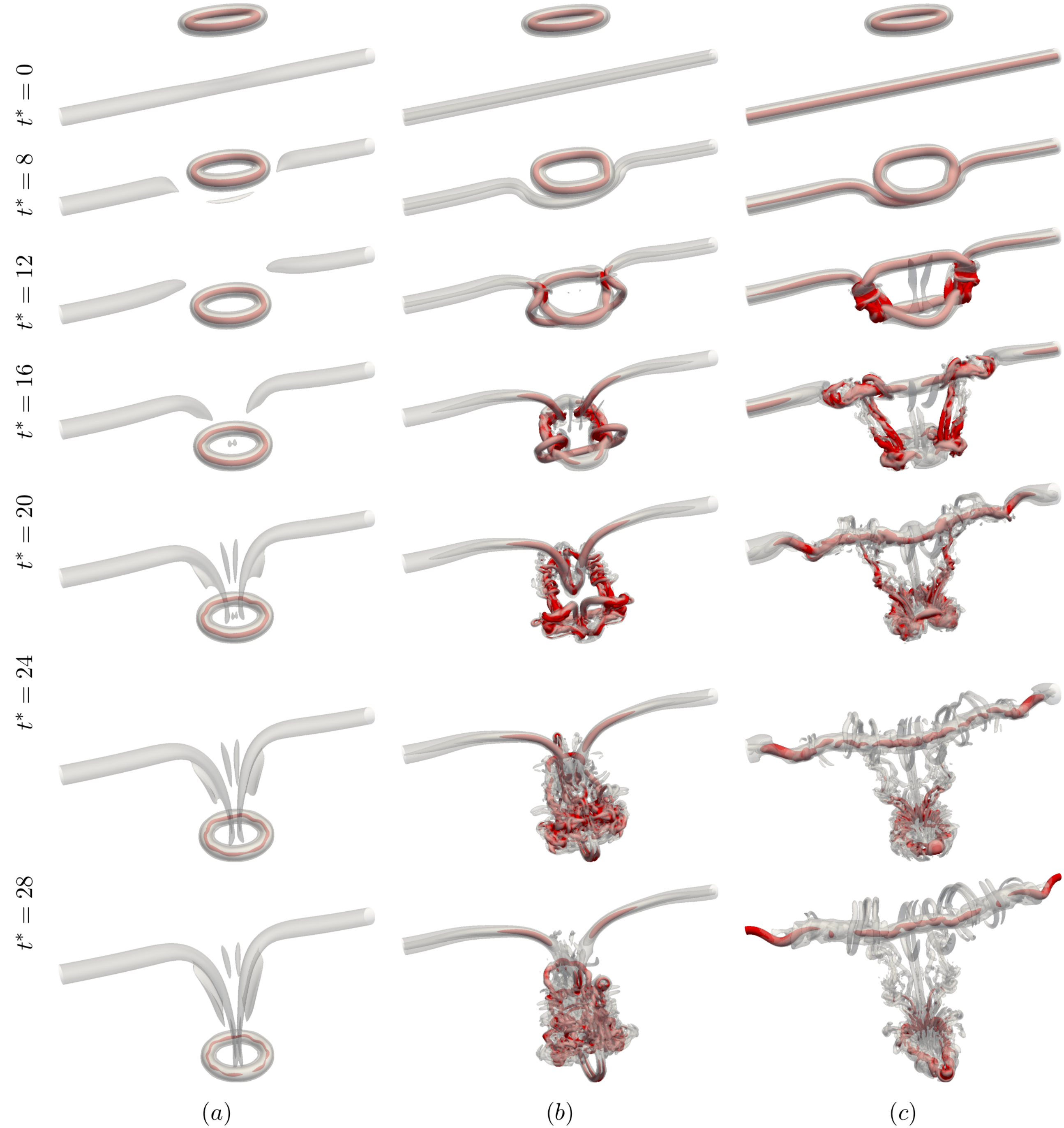

$t^* = 0$
$t^* = 8$
$t^* = 12$
$t^* = 16$
$t^* = 20$
$t^* = 24$
$t^* = 28$
(a)
(b)
(c)

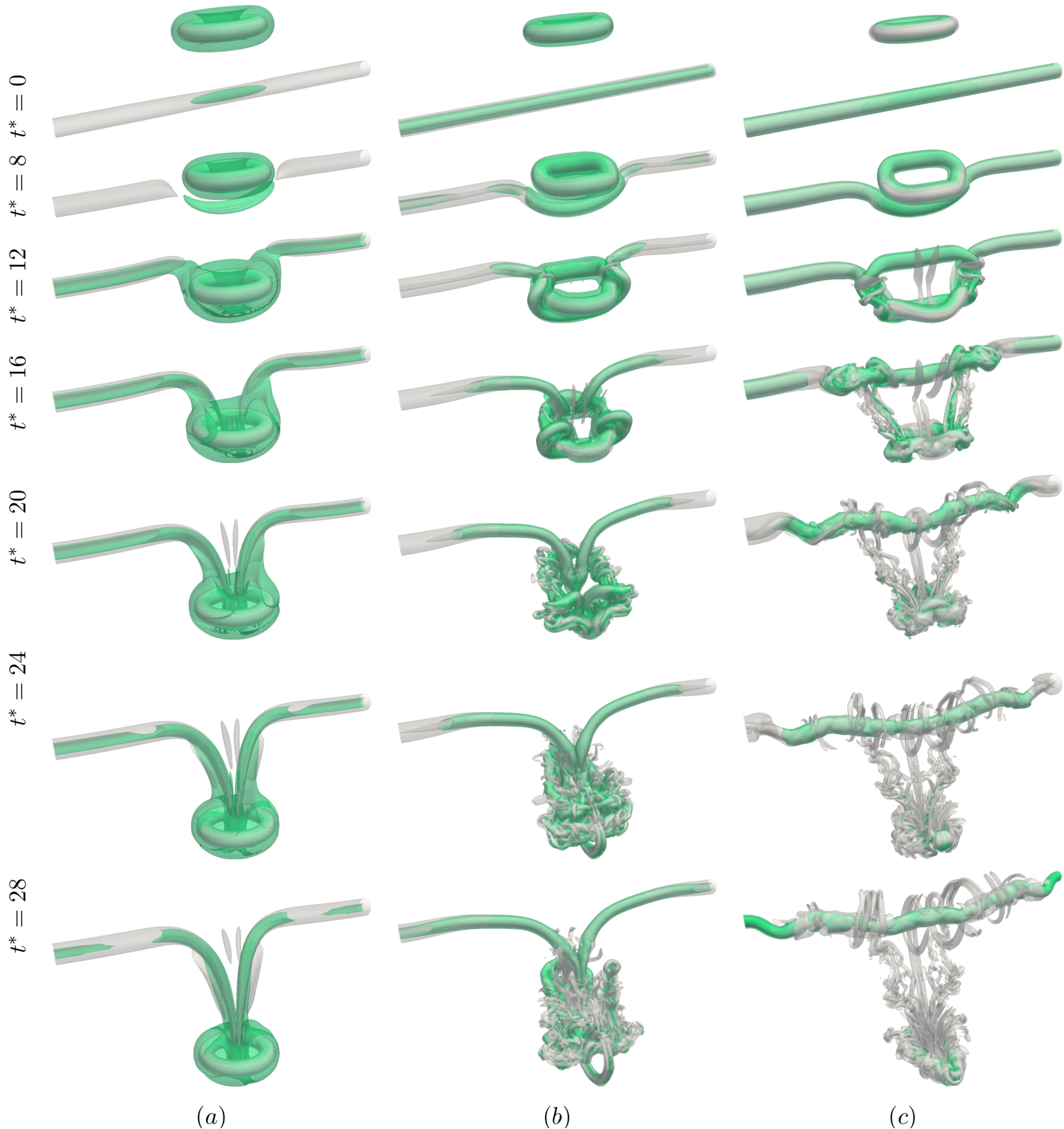
$t^* = 0$
$t^* = 8$
$t^* = 12$
$t^* = 16$
$t^* = 20$
$t^* = 24$
$t^* = 28$
(a)
(b)
(c)

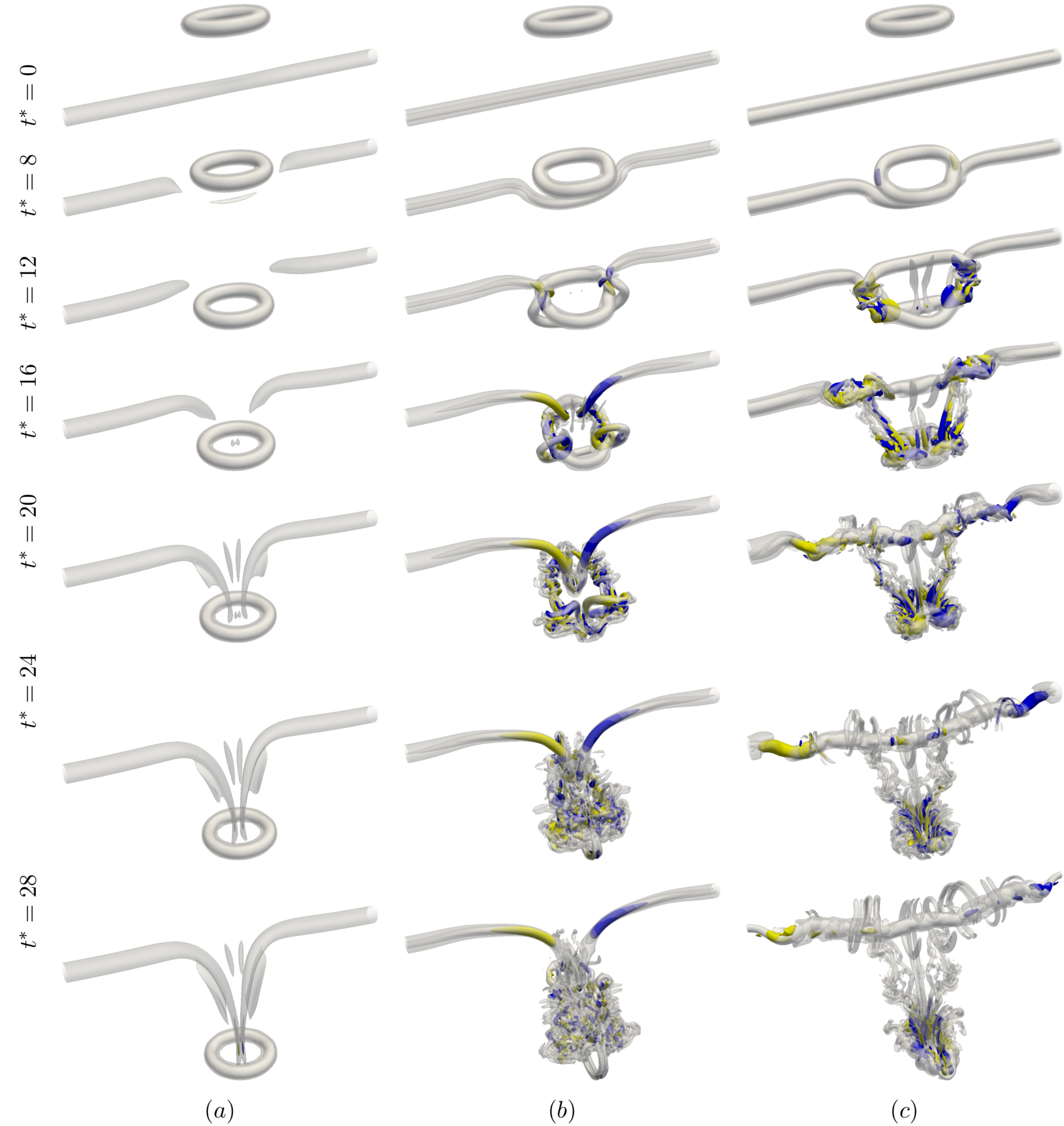

$t^* = 0$
$t^* = 8$
$t^* = 12$
$t^* = 16$
$t^* = 20$
$t^* = 24$
$t^* = 28$
(a)
(b)
(c)

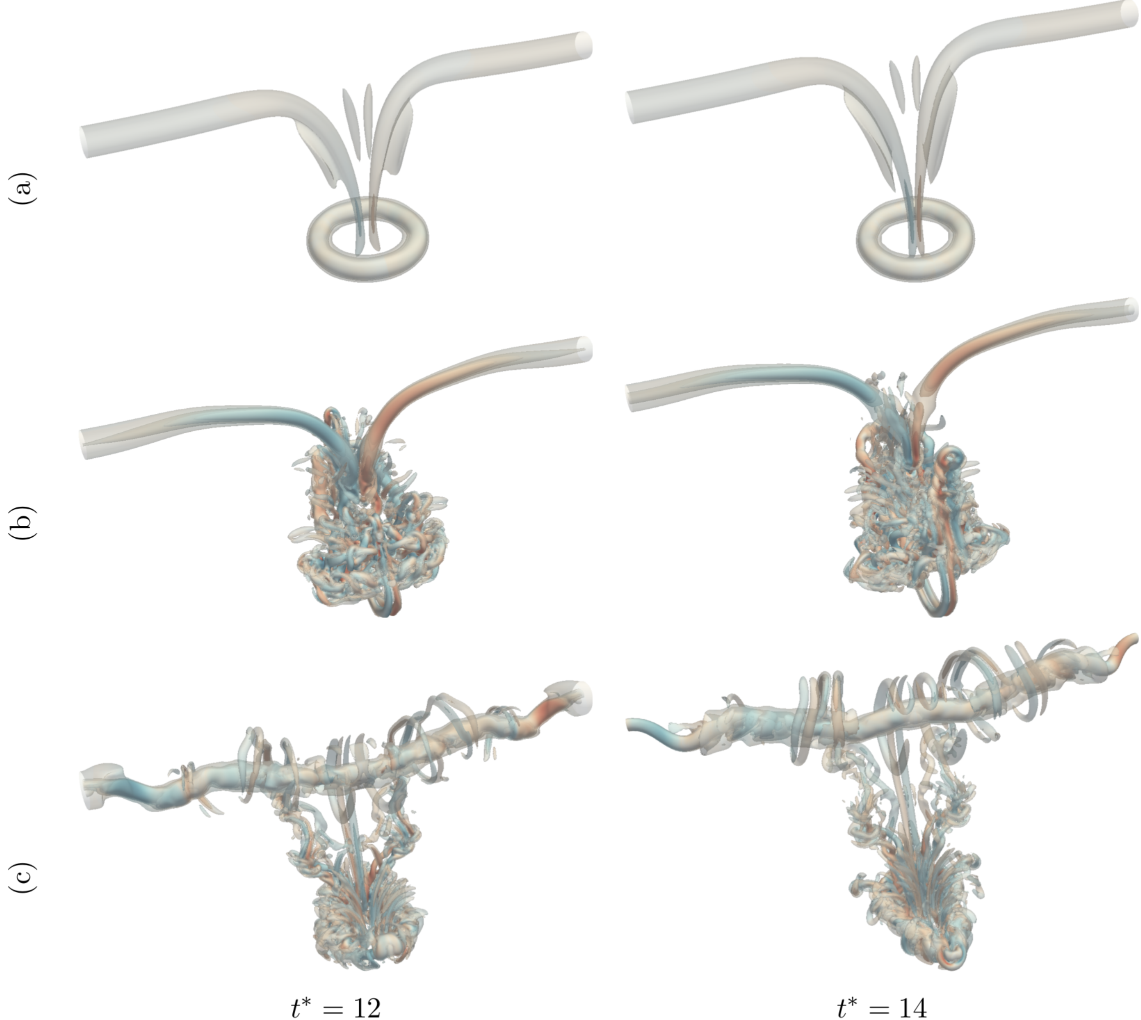
(a)
(b)
(c)
$t^* = 12$
$t^* = 14$

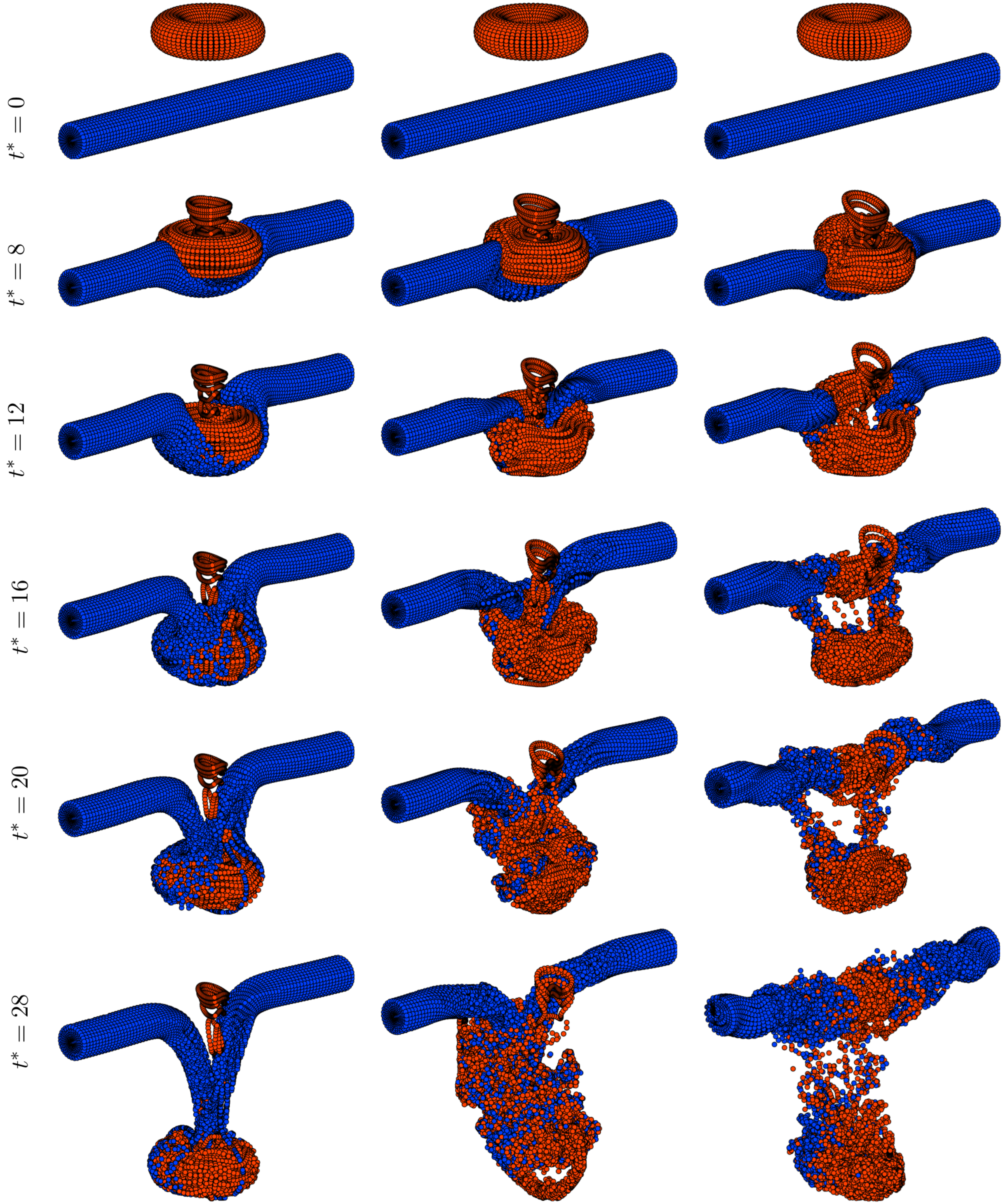

(a) (b) (c)

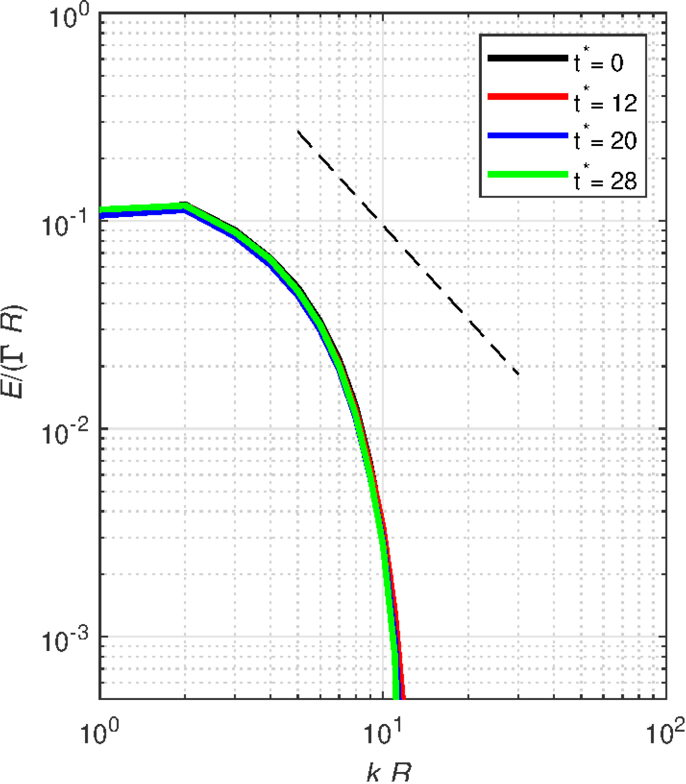

t* = 0
t* = 12
t* = 20
t* = 28
E/(Γ R)
k R

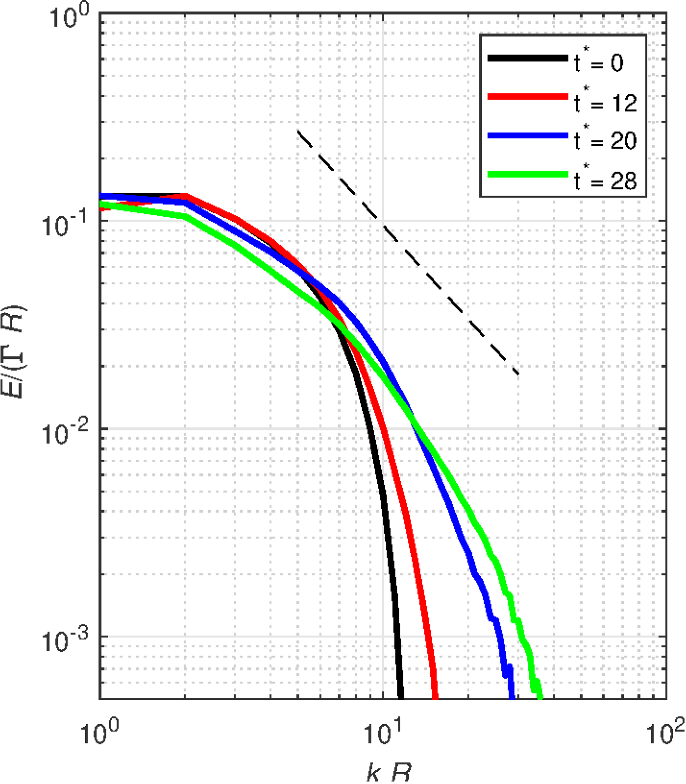

t* = 0
t* = 12
t* = 20
t* = 28
E/(Γ R)
k R
10^0
10^-1
10^-2
10^-3
10^1
10^2

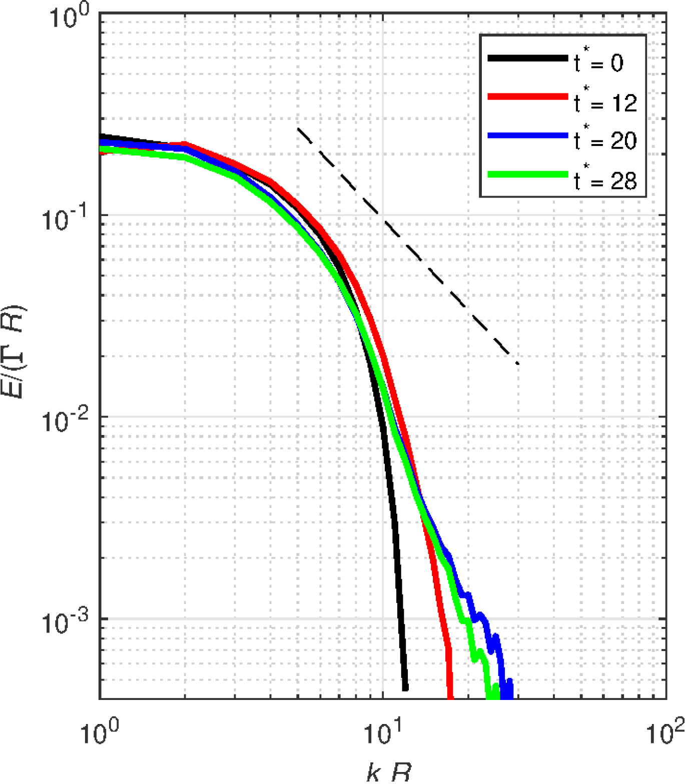

$t^* = 0$
$t^* = 12$
$t^* = 20$
$t^* = 28$
10^0
10^{-1}
10^{-2}
10^{-3}
10^0
10^1
10^2
$E/(\Gamma R)$
$k\ R$

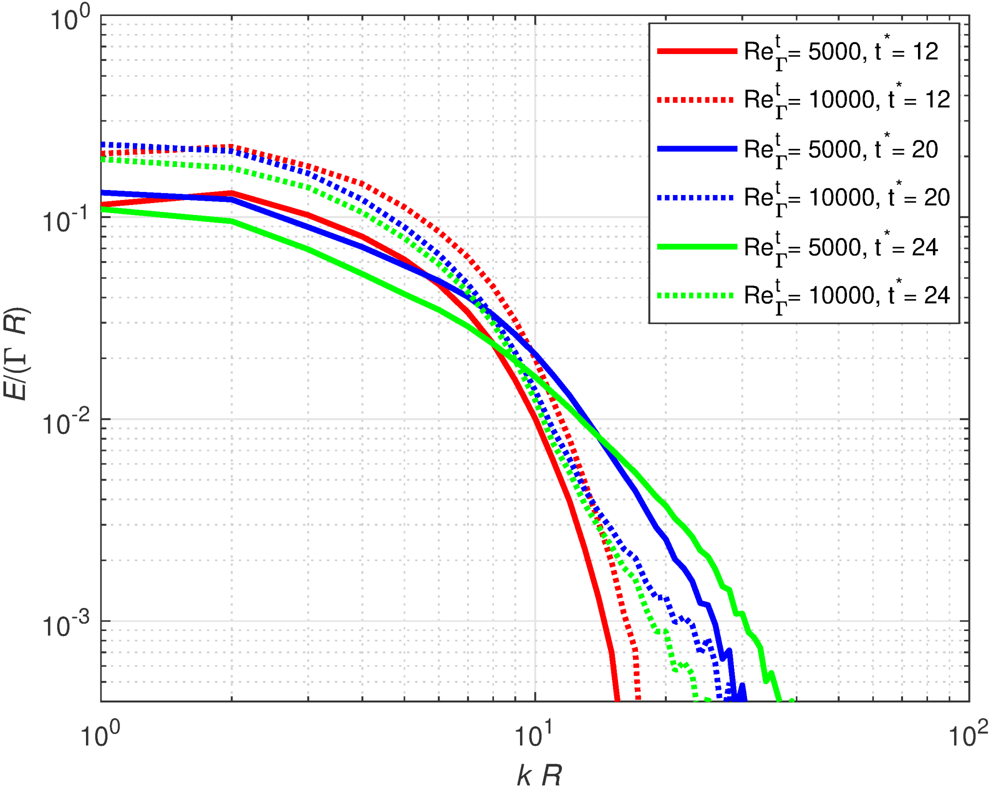

10^0
10^{-1}
10^{-2}
10^{-3}
$E/(\Gamma\ R)$
10^0
10^1
10^2
$k\ R$
Re^t_Γ= 5000, t^* = 12
Re^t_Γ= 10000, t^* = 12
Re^t_Γ= 5000, t^* = 20
Re^t_Γ= 10000, t^* = 20
Re^t_Γ= 5000, t^* = 24
Re^t_Γ= 10000, t^* = 24

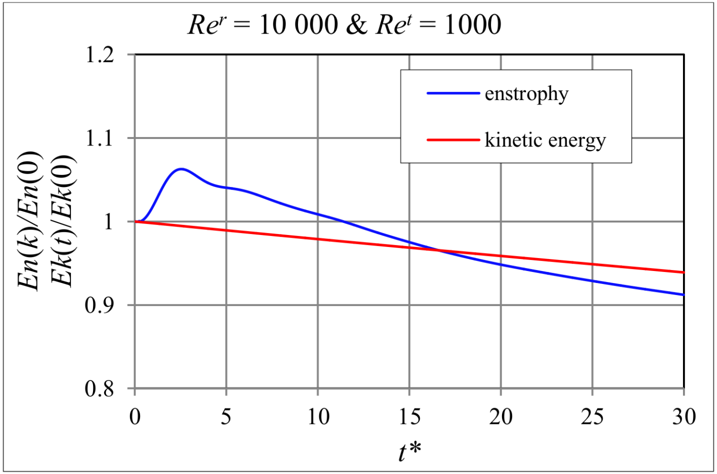

Re^r = 10 000 & Re^t = 1000
enstrophy
kinetic energy
$En(k)/En(0)$
$Ek(t)/Ek(0)$
1.2
1.1
1
0.9
0.8
0
5
10
15
20
25
30
t^*

(a)

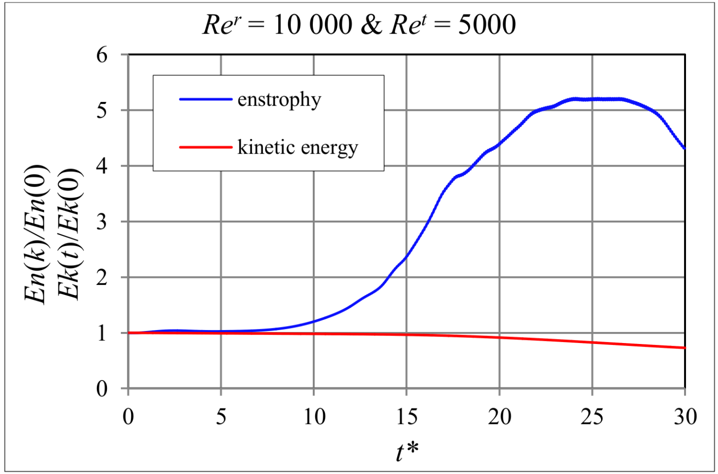

Re^r = 10 000 & Re^t = 5000
enstrophy
kinetic energy
$En(k)/En(0)$
$Ek(t)/Ek(0)$
6
5
4
3
2
1
0
0
5
10
15
20
25
30
t^*

(b)

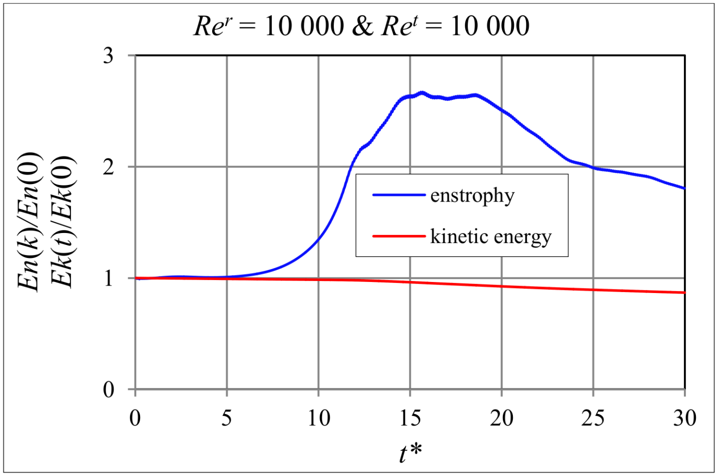

Re^r = 10 000 & Re^t = 10 000
enstrophy
kinetic energy
$En(k)/En(0)$
$Ek(t)/Ek(0)$
3
2
1
0
0
5
10
15
20
25
30
t^*

(c)

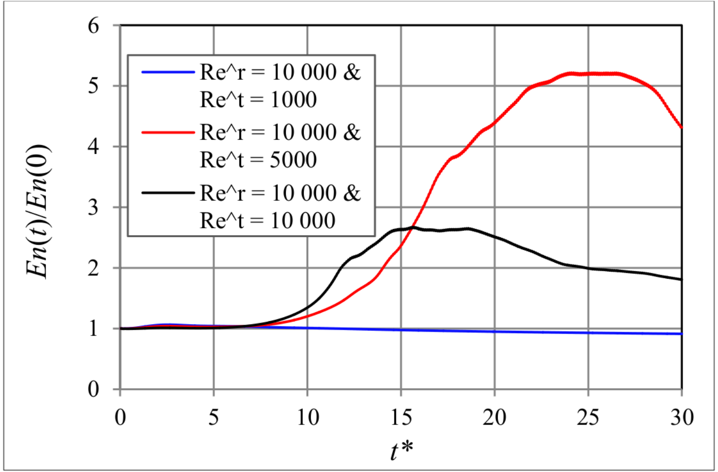

6
5
4
3
2
1
0
En(t)/En(0)
Re^r = 10 000 &
Re^t = 1000
Re^r = 10 000 &
Re^t = 5000
Re^r = 10 000 &
Re^t = 10 000
0
5
10
15
20
25
30
t*

(a)

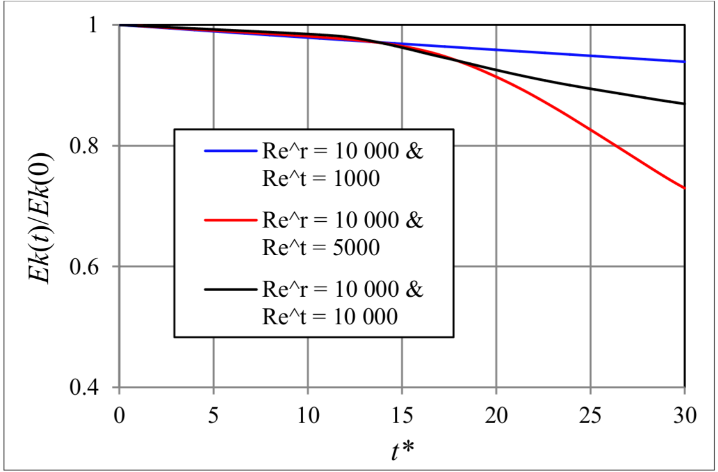

1
0.8
0.6
0.4
Ek(t)/Ek(0)
Re^r = 10 000 &
Re^t = 1000
Re^r = 10 000 &
Re^t = 5000
Re^r = 10 000 &
Re^t = 10 000
0
5
10
15
20
25
30
t*

(b)

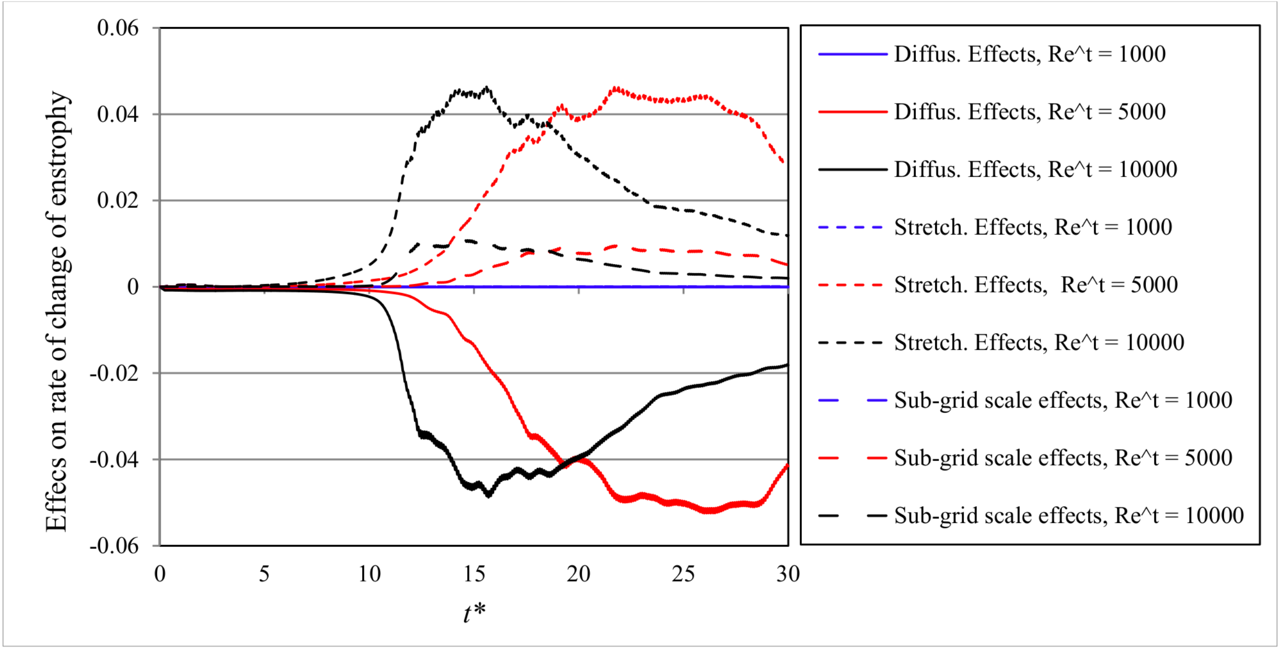

0.06
0.04
0.02
0
-0.02
-0.04
-0.06
Effecs on rate of change of enstrophy
0
5
10
15
20
25
30
t*
Diffus. Effects, Re^t = 1000
Diffus. Effects, Re^t = 5000
Diffus. Effects, Re^t = 10000
Stretch. Effects, Re^t = 1000
Stretch. Effects, Re^t = 5000
Stretch. Effects, Re^t = 10000
Sub-grid scale effects, Re^t = 1000
Sub-grid scale effects, Re^t = 5000
Sub-grid scale effects, Re^t = 10000